HOKKAIDO UNIVERSITY

Title	Effect evaluation of grass on shallow slope stability of unsaturated volcanic soil in seasonal cold region
Author(s)	NGUYEN BINH, THANH
Citation	北海道大学. 博士(工学) 甲第14304号
Issue Date	2020-12-25
DOI	10.14943/doctoral.k14304
Doc URL	http://hdl.handle.net/2115/80249
Type	theses (doctoral)
File Information	NGUYEN_BINH_THANH.pdf

Instructions for use

Hokkaido University Collection of Scholarly and Academic Papers : HUSCAP

Effect evaluation of grass on shallow slope stability of unsaturated volcanic soil in seasonal cold region

積雪寒冷地の不飽和火山灰質土斜面表層の安定性に及ぼす植生の影響評価

By

Binh Thanh NGUYEN

A thesis submitted in partial fulfillment of the requirements for the degree of Doctor of Philosophy in Engineering
under the guidance and supervision of
Professor Tatsuya ISHIKAWA

Examined by the Doctoral Committee
Professor Tatsuya ISHIKAWA
Professor Yoichi WATABE
Professor Satoru KAWASAKI

December 2020

English Engineering Education Program (e^3)
Laboratory of Analytical Geomechanics
Division of Field Engineering for the Environment
Graduate School of Engineering
Hokkaido University
Sapporo, Hokkaido, Japan

ABSTRACT

Vegetation has been recognized as an environmentally friendly method for stabilizing soil slope through hydro-mechanical effects. In terms of hydrological effects, transpiration could induce soil matric suction hence result in an increase in soil shear strength and a decrease in coefficient of permeability. In addition, the presence of vegetation roots could cause the change in soil hydraulic properties. Vegetation roots enhance water retention capacity and reduce coefficient of permeability of soil. These effects minimize infiltration into soil slope. Furthermore, soil shear strength at the potential slip surface of slope is increased due to the tensile shear strength provided by roots. As a result, the landslide-prone areas might be stabilized due to the hydro-mechanical effects of vegetation.

Quantifying the hydrological properties of soil with different vegetated ages is vital to predict the long-term performance of vegetated soil slope. However, measuring the hydraulic properties (i.e. SWCC and unsaturated coefficient of permeability) of soils is time-consuming and costly. Currently, the simple model to estimate the hydraulic properties of vegetated soil is not available. Moreover, there is a lack of understanding about relationship of soil shear strength and root content at different grass ages. Comprehensive field measurements and numerical studies were rarely carried out to properly consider hydro-mechanical effects of grass on instability of soil slope. In addition, researches often studied the vegetation species in tropical or subtropical regions (i.e. Vetiver grass, Bermuda grass, Ivy tree), whereas seldom have studies paid attention to vegetation species which are commonly used in the seasonal cold region.

To overcome the above-mentioned limitations, this study investigates the effects of grass age on hydraulic properties of coarse-grained volcanic soil, namely: Komaoka soil. The soil-water characteristic curves (SWCC), unsaturated coefficient of permeability, outflow, runoff, and the variations in volumetric water content/matric suction under different rainfall intensities are measured by carrying out column tests. In addition, permeability tests are performed to determine the saturated coefficients of permeability of bare soil and grassed soils. The experimental results reveal that the grass age has an influence on the hydraulic properties of Komaoka soil. At the same volumetric water content, grassed soil with higher grass age has higher matric suction. Both saturated and unsaturated coefficient of permeability are significantly reduced with the increase in the grass age. Moreover, there is a decrease in the outflow and an increase in the runoff for grassed soil with higher grass age. Matric suction decreases later in grassed soil than that of bare soil under rainfall events. The new model is proposed to estimate the unsaturated coefficient of permeability of coarse-grained soil due to the effects of grass roots. The good agreement between estimations and experimental results shows that the proposed model is useful to capture the decrease in unsaturated coefficient of permeability of grassed soil.

In order to investigate the reinforced strength of the grassed soil, a series of consolidated drainage (CD) compression tests were performed on root-reinforced soils with different grass ages. Experimental results reveal that there is significant increase in peak shear strength, effective cohesion of grassed soil as the grass root volume ratio is increased, whereas a slightly higher effective angle of internal friction is observed. Furthermore, the volumetric strain is decreased with the rise in root volume ratio.

In this research, a field study was carried out on unsaturated soil slopes. The field measurement consisted of two neighboring cut slopes, namely bare slope and grassed slope. Field measurement results reveal that grass has influences on reducing and stabilizing the soil water content, increasing matric suction, and lowering soil temperature in warm seasons. In winter, the gap of matric suction between bare slope and grassed slope is greater than that in other seasons. In addition, the soil temperature of grassed slope is higher than bare slope. The approach of coupled nonisothermal-seepage numerical analysis for unsaturated soil slope considering impacts of grass is suggested. The good agreement regarding to soil temperature and volumetric water content between simulation and field measurement indicates that the proposed approach is useful to consider the influences of grass on the hydro-thermal behaviors of unsaturated soil lope against climate variations. Furthermore, the slope stability analysis has been performed considering enhanced shear strength of soil due to grass roots. The higher values of FOS and maximum depth of slip surface of grassed slope presents that the grass is effective to resists the shallow landslide-prone area. The application of the recommended numerical approach is expected to contribute to pre-design study of grassed unsaturated soil slopes.

The thesis includes 9 chapters. Chapter 1 introduces the background, objectives, and organization of this study. Chapter 2 reviews past studies related to effects of vegetation on unsaturated soils. Chapter 3 illustrates the soil slope measurements. Chapters 4 and 5 show the effects of grass age on hydraulic properties of saturated and unsaturated soil, respectively. A new model for estimating hydraulic properties of grassed soils is presented in chapter 6. Chapter 7 shows the mechanical properties of saturated soil at different grass ages. The numerical approach of coupled nonisothermal-seepage numerical analysis for unsaturated soil slope considering impacts of grass is suggested in chapter 8. Finally, chapter 9 summarizes the conclusions obtained in this study and gives the recommendation for further studies.

< This dissertation is a part of the following original journals and proceedings >

1. Nguyen B.T., Ishikawa T., Murakami T.: Effect evaluation of grass age on hydraulic properties of coarse-grained soil. *Transportation Geotechnics*, Vol.25, 100401 (2020).

2. Nguyen, B.T., Ishikawa, T, Murakami T.: Numerical analysis of in-situ water content and temperature variations due to effects of grass cover. *Japanese Geotechnical Society Special Publication*, Vol.7(2), pp: 660-668 (2019).

3. Jin P., Nguyen B.T., Ishikawa, T.: Effect of grass root on deformation strength characteristics of a volcanic coarse-grained soil. *53rd Japan National conference*. 2018 July 24-27, Takamatsu, Japan.

4. Nguyen, B.T., Ishikawa, T., Siva Subramanian, S.: Rainfall infiltration and runoff characteristics of an unsaturated volcanic soil under grass cover, *Second Pan American Conference on Unsaturated soils*, 2017 November 12-15, Texas, USA.

5. Nguyen, B.T., Ishikawa, T., Mori. K.: Influence of grass cover on the infiltration of unsaturated volcanic soil. *Geotechnics for Sustainable Infrastructure Development*, 2016 November 24-25, Hanoi, Vietnam.

ACKNOWLEDGEMENT

Firstly, I would like to express my sincere and deepest gratitude to my supervisor Prof. Tatsuya Ishikawa for his patient guidance, valuable advice, and continuous support during my doctoral study and related research. Prof. Tatsuya Ishikawa had a profound impact on my academic attitude throughout my doctoral program with his immense specialized knowledge, excellent academic level, and stringent academic spirit. It is Prof. Tatsuya Ishikawa who introduces me to the field of unsaturated soil and encourages me to explore the unknown. His guidance helped me in all the time of my research and writing of this dissertation. Without Prof. Tatsuya Ishikawa's persistent guidance, this dissertation would not have been possible.

Sincere appreciation is due to all members of the doctoral committee, Prof. Yoichi Watabe and Prof. Satoru Kawasaki for their valuable comments, constructive suggestions, and tremendous support not only on this dissertation but also on annual evaluations.

I am sincerely grateful to Dr. Srikrishnan Siva Subramanian, Dr. Bin Luo, Dr. Zhu Yulong, and Mr. Takumi Murakami for giving me important inspiration, valuable guidance and continuous help to my research. I also grateful acknowledge to the students of Laboratory of Analytical Geomechanics for their help during these three years.

The MEXT scholarship provided by Japanese Government through English Engineering Education (E3) Program, Graduate School of Engineering, Hokkaido University, is also gratefully acknowledged.

Finally, my special thanks are extended to my beloved wife Truong Thi Thuong, my son Nguyen Viet Hoang, my parents, family and friends. Without their encouragement, support and confidence in me all through these years, it would not be possible for me to arrive Japan and complete my doctoral study.

TABLE OF CONTENTS

LIST OF FIGURES

LIST OF TABLES

1 INTRODUTION

1.1 Background

Vegetation has been applied in engineering design methods because of its numerous benefits such as preventing the soil from erosion, improving the aesthetics of the environment, and reinforcing the structure of the soil. In addition, vegetation has been widely employed as an environmentally friendly restoration technique for stabilizing soil slopes through both hydrological and mechanical reinforcement. The effects of basic plant traits on their slope stability functions in compacted and planned green slopes have been summarized in the study of Bordoloi and Ng 2020. Furthermore, the heat insulation due to grass leaves and reinforcement of vegetation cover effectively restrain the displacement of the shallow soil slope soil in the cold region (Rui et al. 2018). The hydrological benefits of vegetation have been widely experimentally investigated. Recent experimental studies reveal that the presence of roots affects the soil hydraulic properties such as soil-water characteristic curve (SWCC), saturated/unsaturated coefficient of permeability, infiltration, and surface runoff (Rahardjo et al 2014, Leung et al. 2015a, Johantisankasa and Sirirattanachat 2017, Nguyen et al. 2020). The past studies clearly showed that the effects on soil hydraulic properties are inconsistent and depend on types of soil and vegetation species. The vegetation also has effects on transpiration (Ng et al. 2013a,b, Leung 2014, Leung et al. 2015a,b, Ni et al. 2017, 2018). The higher matric suction induced by evapotranspiration results in a lower coefficient of permeability hence the soil slope is further stabilized. In contrast, the long-term field measurements of vegetated soil are rarely carried out. Ng et al (2019) conducted a field study to investigate the effect of vegetation growth and spacing on hydraulic properties of soil. The vegetation species were *Schefflera arboricola* and *Cynodon dactylon* which are drought tolerant. Seldom have studies paid attention to vegetation species which are commonly used in the seasonal cold region.

Cui et al. (2005, 2010) and An et al. (2018 a,b) examined the hydro-thermal behavior of embankment under climate effects. The numerical approach proposed in these studies reproduced well as compared to the field monitoring data for bare soil. On the contrary, numerical simulation approach which considers the influence of vegetation on hydro-thermal properties of unsaturated soil is not well understood. Pagano et al. (2019) reported that the hypothesis of bare soil cannot be used to analyses vegetated conditions. Nguyen et al (2017), Shao et al (2017), and Ni et al (2018) reported that the seepage behavior under rainfall infiltration in vegetated soil could be reasonably predicted if the hydraulic properties of vegetated soil including SWCC and saturated/ unsaturated coefficient of permeability are properly considered. Several numerical studies were performed to evaluate the effect of evapotranspiration on only hydraulic behaviors of soil. However, vapor transport was not taken into account in the numerical simulation (Ni et al 2018, Ni et al. 2019a, Ng. et al 2019). It is noted that considering the coupled transport of heat and water in soil is important when investigating the hydro-mechanical behavior of soil during evaporation (An et al. 2018a).

Therefore, vapor transport plays an important role to properly study the soil water content near the soil surface. Ni et al. (2019a) presented that soil temperature has influences on transpiration. The root water uptake was inhibited due to low soil temperature. Without considering soil temperature effects on transpiration, the soil water content was underestimated by around 50% in the autumn period. Since only the seepage analysis had been performed in Ni et al. (2019a) study, soil temperature near the surface was estimated based on empirical model. The coupled nonisothermal-seepage analysis, which takes both the vapor transport and the effect of vegetation cover on the reduction of soil temperature into account, is useful to the numerical assessment of vegetated soil slope performance.

Soil shear strength at the potential slip surface of slope is increased due to the enhanced shear strength provided by roots. As a result, the shallow landslide-prone areas might be resisted due to the mechanical effects of vegetation. Shear strength behaviors of root-reinforced soil were studied by direct shear test in both experimental laboratory and in-situ condition (Fan and Su 2008, Wood et al. 2016, Mahannopkul and Jotisankasa 2019, Yildiz et al 2018, 2020). The drawback of the direct test is that the failure plane is commonly assumed. However, stress and strain in a sample are uneven and complicated and the weakest surface may not be the assumed shear plane in reality. In addition, the whole process of a test, from loading to breaking, can be monitored closely, in which shear strength, stress-strain relationship, and changes of the sample volume can be measured simultaneously (Zhang et al, 2010). Few past researches employed the root-induced changes in shear strength properties of vegetated soils to numerically access the stability of unsaturated soil slope (Ni et al. 2018). The cohesion of rooted soils in these researches was empirically estimated by Wu and Watson (1998), and Liang et al (2020) models. There is limited research that determines the effect of natural roots on an increase in shear strength properties of soils by triaxial test. The effects of roots on the factor of safety of vegetated soil slope are more properly determined by employing shear strength parameters of rooted soil which are studied from the triaxial test.

This study investigates the effects of grass age on hydraulic properties of coarse-grained soil by performing a series of permeability tests and column tests. In addition, this study aims to investigate the influences of grass on variations in soil water content, matric suction and soil temperature in unsaturated soil slopes from a field measurement. A series of triaxial tests were performed to investigate the influences of grass roots on shear strength behaviors of saturated soil. Furthermore, a numerical simulation approach considering the effects of grass on thermal-hydro properties, and to access the shallow stability of grassed unsaturated soil slope is proposed.

1.2 Objectives and Organization

This thesis consists of nine chapters. The introduction and objectives of this study have been provided in the current chapter.

Chapter 2 introduces unsaturated soil, slope failure due to infiltration, and the effects of vegetation on hydraulic properties and seepage behavior of soil (i.e. matric suction, water content, coefficient of permeability). The mechanical effects of vegetation on soils are also mentioned.

Chapter 3 presents the field measurement of two neighboring soil slopes including bare slope and grassed slope, which were constructed in Hokkaido, Japan. The field instrumentation and field measurement results (i.e. volumetric water content, matric suction, soil temperature) of two unsaturated soil slopes are described.

Chapter 4 discusses the effects of grass age on saturated coefficient of permeability of soil. The permeability test apparatus is employed to study the saturated coefficient of permeability of grassed soil. The overview of test apparatus and experiment procedures are explained. It is followed by the results of the permeability test and discussions.

Chapter 5 discusses the effect of grass age on unsaturated coefficient of permeability and seepage behavior of grassed soil. The column test apparatus is employed to investigate the hydraulic properties (i.e. soil-water characteristic curve and unsaturated coefficient of permeability) and seepage behaviours (i.e. infiltration, runoff) of grassed soil. The overview of column test apparatus, and experimental procedures are explained. After that, the results of column test and are discussed.

Chapter 6 proposes new model to estimate the unsaturated coefficient of permeability of grassed soils. In this chapter, the new model for estimating unsaturated coefficient of permeability of grassed soils with different grass ages is proposed. After that, the new model is validated by comparing with the experimental results of column test.

Chapter 7 presents the effect of grass age on mechanical properties of soil. Triaxial test apparatus is used to study the shear behavior of grassed saturated soils. After that, the unsaturated shear strengths of grassed soils are estimated. The shear behaviours of grassed saturated soils and estimated shear strength of grassed unsaturated soils with different grass ages are discussed.

Chapter 8 investigates the numerical analysis approach considering effects of grass on variations in volumetric water content/matric suction and soil temperature in unsaturated soil slope. Analytical analysis procedure considering evapotranspiration is validated based on the past experimental results. After that, the approach of coupled nonisothermal-seepage numerical analysis for unsaturated soil slope considering the impacts of grass on hydraulic properties of soil is suggested. Next, the shear strength of grassed unsaturated soil derived from triaxial test is employed in slope stability analysis to access the shallow stability of grassed unsaturated soil slope.

In chapter 9, the conclusions and some recommendations for the future works are given.

2 LITERATURE REVIEW

2.1 Unsaturated soil

The soil zone which is between the ground surface and the water table is referred to as the unsaturated soil zone by Fredlund et al. (2012) as shown in Figure 2.1. Generally, in geotechnical engineering, the zone which is subjected to negative pore-water pressures has been widely referred as the unsaturated soil zone. In the unsaturated field, the ground surface climate is an important factor which determines the thickness of the unsaturated zone by controlling the depth from the ground surface to the groundwater table. Any soil near the ground surface will be subjected to negative pore-water pressures and possible reduction in degree of saturation once it is in an environment where the water table is below the ground surface. With consideration of the wide existence of unsaturated soil, it is necessary to investigate the difference of mechanical properties between the saturated soil and the unsaturated soil.

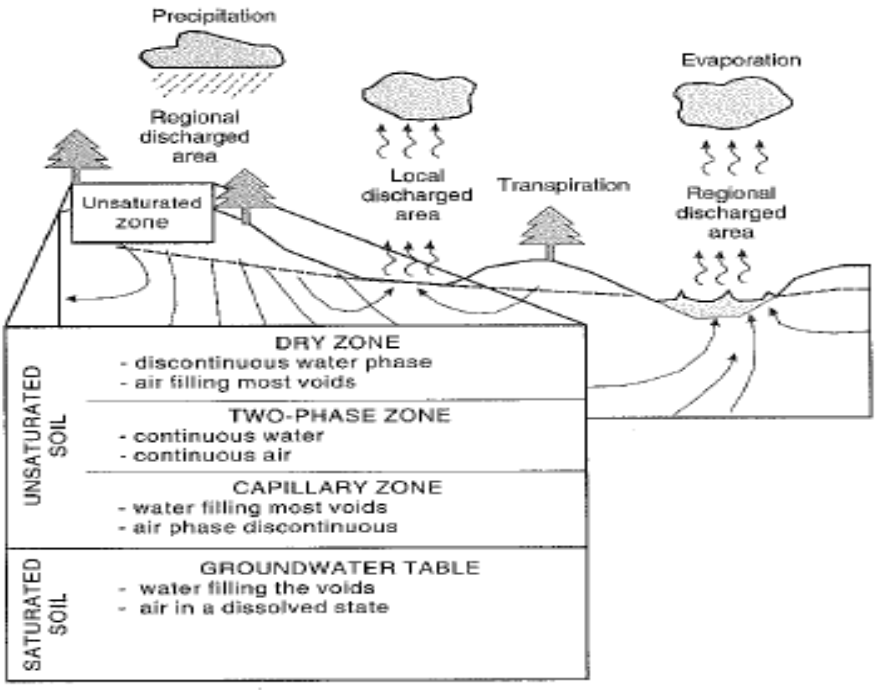

Figure 2.1 Subdivisions of unsaturated soil zone on the local and regional basis (Fredlund et al. 2012).

Within the saturated soil and the air-dried soil, there are only two phases existed, i.e., soil structure and other fluid in the voids. Such soils could be well explained by principles and concepts of classical soil mechanics. In unsaturated soil's situation, however, it has commonly been considered to have more than two phases, i.e., soil structure, water, and air. In addition, the air-water interface (i.e., the contractile skin) has been realized to play an important role as an additional phase in unsaturated soils. Fredlund et al. (2012) suggested that when the air phase is continuous, the contractile skin will interact with the soil particles to

provide an influence on the mechanical behaviour of the soil. Figure 2.2 shows an element of unsaturated soil with a continuous air phase.

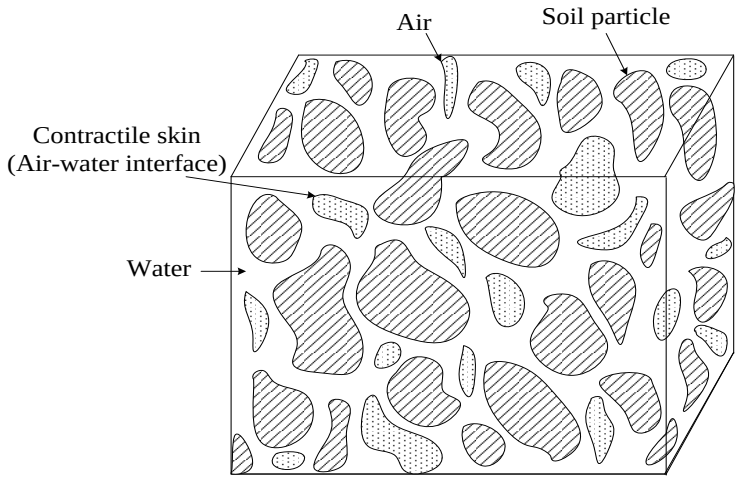

Figure 2.2 Element of unsaturated soil with a continuous air phase (Fredlund et al. 2012).

2.2 Slope failures due to rainfall and snowmelt infiltration

Rainfall-induced landslides are common in many regions under tropical or subtropical climates. Fig. 2.3 shows the global landslide susceptibility map of rainfall-induced landslides produced by National Aeronautics and Space Administration (NASA) with a combination of surface landslide susceptibility and a real-time space-based rainfall analysis system (Hong and Adler 2008). The red and orange indicate regions with high-potential landslide risk include the Pacific Rim, the Alps, and South Asia, Rocky Mountains, Appalachian Mountains, and parts of the Middle East and Africa. Based on the historical records, most catastrophic landslides and debris flows have occurred in Japan, China, India, Singapore, the United States, Italy, Brazil, and Venezuela.

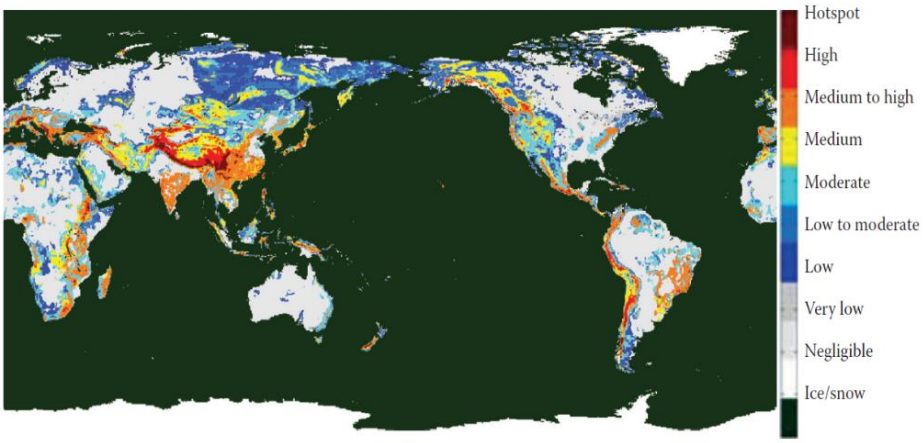

Figure 2.3 Global susceptibility map of rainfall-induced landslides. (Hong, Y. et al, 2008).

Figure 2.4a shows a notable landslide triggered by the rainstorms in the March 4, 1995, La Conchita landslide. It occurred in the small residential community of La Conchita at the northwest of Los Angeles. This landslide was a reactivation of an ancient complex earth flow in marine sediments and badly damaged nine houses (Jibson, 2005). Because the slide moved at only a moderate rate (tens of meters in a few minutes), there were no casualties. On January 10, 2005, the left side of the 1995 La Conchita landslide remobilized due to a heavy rainfall. A high-velocity debris flow at an estimated velocity of 10 m/s destroyed 13 houses (Figure 2.4b).

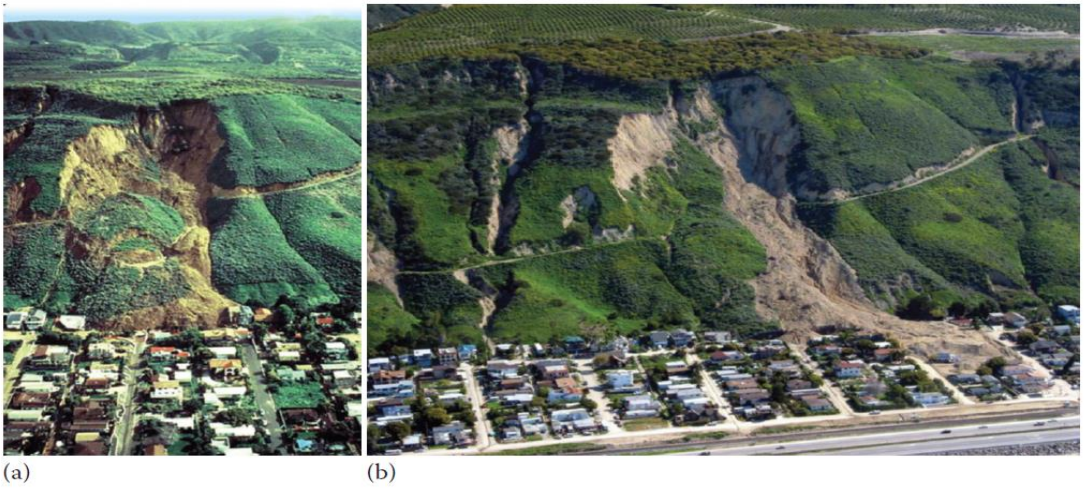

Figure 2.4 The landslides occurred in La Conchita, California. (a) The March 4, 1995, rainfall-triggered La Conchita, California, landslide. (Courtesy of Robert L. Schuster, US Geological Survey.) (b) The January 10, 2005, remobilization of part of the 1995 landslide.

Ishikawa et al (2015) reported that according to the data for the last 14 years, the slope failure made up 62% of a total number of the causes for the urgent inspections at the national roads in Hokkaido. Fig. 2.5 presents an example failure occurred at Hikachi Pass, Hokkaido, Japan due to the heavy rain on 31 August, 2016.

Figure 2.5 Slope failure at Route No. 38, Hikachi Pass, Hokkaido, Japan on 31 August, 2016.

In seasonally cold regions, rainfall and snowmelt water infiltration are major factors that influence the soil slope stability. The increase in pore-water pressure caused by the rainwater and snowmelt water infiltration results in the decrease in matric suction of unsaturated soil is considered the main cause of the slope failure. Ishikawa et al. (2010, 2015) indicated that there is a difference in the failure mechanism of slopes between cold regions and warm-temperate regions due to additional factors, i.e., freeze-thaw action causes residual displacement to parallel to the slope surface and shear strain at the subsurface layer. Fig. 2.6 presents slope failure happened at National Highway No.230 (near Nakayama Pass and Jouzai stream) at 11:20 A.M., April 7, 2013 (Nguyen et al. 2016). This location was approximately 6.5 km southwest of Jouzai hot spring and the highway plays an important role in connecting Sapporo and Kunon district, Setana town (Fig. 2.6a). The size of slope failure was 44 m in length (from KP34,360.0 to KP34,404.0) and 19 m in height. Approximately 11,000 m^3 of sediment flowed out downward to slope foot with snow as shown in Fig. 2.6 (b).

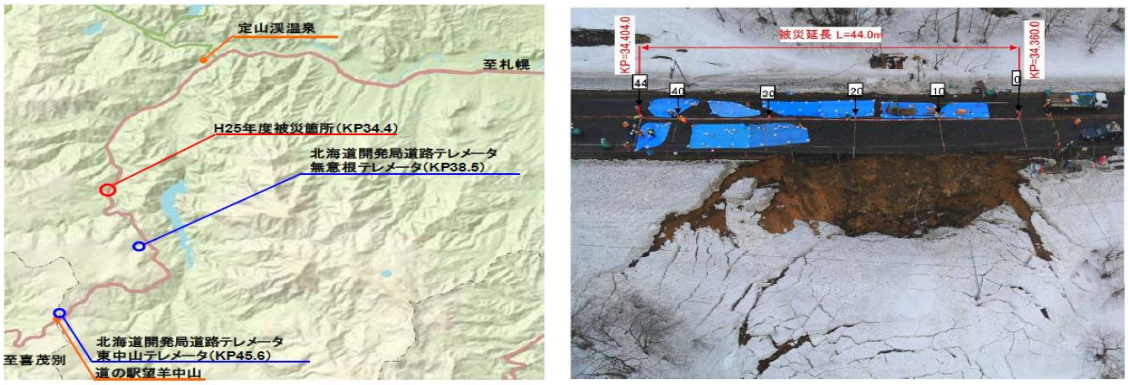

Figure 2.6 (a) Location of slope failure (b) slope failure covered with snow.

2.3 Effects of vegetation on hydraulic properties of soil

Leung. et al 2015b compared the measured cumulative water infiltration with time between bare, grass-covered and tree-covered soil during the 2 h of ponding. The constant head of ponding water was 0.1m. In bare soil, water volume infiltrated is found to increase at a decreasing rate. After ponding for 1 h, the amount of water volume infiltrated appears to increase linearly with time, indicating that steady-state condition was reached. A similar trend of variation is observed for both grass-covered and tree-covered soil, and it is found that the volume of water infiltrated in these two types of vegetated soil was similar. The volume of water infiltrated in both vegetated soil was less than that in the bare soil by up to 50% at a steady state although the initial suction between bare, grass-covered and tree-covered soil was comparable. This shown that the water infiltration is reduced because of roots.

Rahardjo et al (2014) reported that both Orange Jasmine and Vetiver grass can be used as environmentally friendly method to minimize the infiltration of rainwater into slopes. The field measurement results presented that Orange Jasmine and Vetiver grass were able to maintain the matric

suction within the slopes during rainfall. In other words, vegetation is an effective slope cover for maintaining the stability of unsaturated soil slopes during rainfall.

It has been recognized that an increase in suction not only increases soil shear strength (Ng and Zhan 2007) but it also reduces coefficient of permeability of soils (Ng and Leung 2016b). Some field studies on residual silty clay slopes, loess-derived alluvial slope, silty loam flat ground showed that vegetated soil could retain suction from 5–20 kPa at 1–1.5m depths (within root zone) after rainfall with return period less than 10 years. Based on laboratory studies (Ng et al. 2013 a,b), more than 9 kPa of matric suctions were retained in the root zone of vegetated silty sand after ponding. More studies are needed to investigate the hydrological effect of vegetation on induced matric suction and hence enhance slope stability during prolonged heavy rainfall.

Evapotranspiration (ET) is defined as the sum of evaporation from the soil surface and transpiration (T) through root-water uptake. The associated changes in soil moisture and matric suction have important implications for the performance of geotechnical infrastructure. Some studies have been conducted to quantify the partitioning of plant transpiration and soil evaporation (Ritchie 1972; Tratch et al. 1995). Based on the measurements of transpiration, evaporation, and ET, several semi-empirical equations were proposed (Ritchie 1972; Tratch et al. 1995) to partition ET into these two components through the addition rule depending on some plant properties such as leaf area index (LAI; a dimensionless index defining the ratio of total one-sided leaf area to the soil surface area). However, the addition rule may not apply to partition ET induced suction into those induced by each individual process of evaporation and transpiration. This is because both the processes are nonlinear and are a direct function of matric suction (Feddes et al. 1976; Wilson et al. 1990).

Ni et al. (2019b) summarized the influences of vegetation on the soil-water characteristic curve (SWCC) and the coefficient of permeability of existing studies. It can be seen that inconsistent results were reported. The differences in vegetation species (Song et al., 2017), soil density (Ng et al., 2014), root content (Jotisankasa and Sirirattanachat, 2017), and vegetation spacing (Ng et al., 2016b; Ni et al., 2016) might result in distinct effects. Higher water retention capacity and a lower coefficient of permeability might be observed in vegetated soil as compared to bare soil because roots block the soil pores (Leung et al., 2015a, b,c; Ng et al., 2016a). However, the formation of macro-pores due to the decayed roots (Ghestem et al., 2011; Ng et al., 2016b) and the preferential flow due to vegetation roots (Li et al., 2016) leads to the contrasting result.

Jotisankasa and Sirirattanachat (2017) presented that grass roots can affect hydraulic properties in different ways. Previous research showed that the coefficient of permeability might be reduced due to actively growing roots. However, a decayed root would cause a preferential flow path hence the coefficient of permeability is increased. The effects of Vetiver grass (Chrysopogon zizanioides) on the soil-water characteristic curve (SWCC), the saturated/unsaturated coefficient of permeability have been investigated on two soil types: low plasticity silt (ML) and clayey sand (SC), compacted at 80% standard Proctor density.

Grass roots affect the hydraulic behavior of soils more significantly in the range of macropore size greater than about 1.5 mm, corresponding to matric suction less than 1 kPa. The saturated coefficient of permeability increased, the air-entry suction decreased, and the SWCC became steeper with increasing root contents (i.e. root volume ratio). Reason is attributed to the formation of cracks caused by wetting and drying cycles during the plant growing period when the root biomasses per soil volume were less than 6 kg/m^3 for ML soil. There is a decrease in the saturated coefficient of permeability and an increase in the air-entry value of ML soil due to roots, after reaching this threshold with root content of about 6.5 kg/m^3 as roots occupied the macropores and tended to suppress cracks and swelling. Regarding SC soil, there is a slight variation of the saturated coefficient of permeability with root content for the upper bound on the saturated coefficient of permeability. In contrast, the lower bound on saturated permeability decreases as root biomass increases. When matric suction exceeds around 30 kPa, the influence of roots on the coefficient of permeability is less significant.

The vegetation age and vegetation species play a key role in the effects on hydraulic properties of soil. Leung et al. (2018) quantified the effects of vegetation ages for two distinct vegetation types (willow and grass) on the infiltration rate. It is reported that the increase in vegetation age results in a faster infiltration rate for willowed soil than that for grassed soil. Song et al. (2017) presented the opposite effects of two distinct grass species even though the same soil was used. The coefficient of permeability of Vetiver grassed soil is significantly higher than that of bare soil. In contrast, there is a decrease in the coefficient of permeability of Bermuda grassed soil compared to bare soil. Researchers often studied the vegetation species in tropical or subtropical regions (i.e. Vetiver grass, Bermuda grass, Ivy tree), whereas seldom have studies paid attention to vegetation species which are commonly used in the seasonal cold region.

Plant evapotranspiration have effects on soil suction of slopes. Ng et al (2016b) quantified changes in tree growth and tree-induced matric suction during evapotranspiration and rainfall under different planting densities for non-mixed-species plantations. It is noted that tree species (*Schefflera heptaphylla*) was planted in silty sand at spacings of 60, 120 and 180 mm, representing three different planting densities. The test results show that reducing the tree spacing from 180 to 60 mm induced greater tree–tree competition for water. There was a higher infiltration rate for vegetated soil with trees planted at a spacing of 60 mm (by 247% higher than) as compared to those for soil with a wider tree spacing, in which mainly fresh roots appeared.

2.4 Effects of vegetation on soil temperature

Vegetation has influences on soil temperature. Some past studies in literature have focused on development of relationship between the vegetation and soil temperature for agricultural fields and forest regions. These relationships could be different due to the differences in soil conditions such as soil density and soil type, vegetation species and temperature between agricultural and urban landscape. Ni et al (2019a)

investigated the effects of vegetation on soil temperature. A simple hydrological model is developed to capture variations in surface soil temperature and its effect on root water uptake. Hypothesis of effects of soil temperature on root water uptake was investigated using field measurements of soil water content. Field site including bare, grass and tree species were studied. There were contrasting trends in variations of water content between summer and autumn for both bare and vegetated soils. As evapotranspiration in summer was higher, water content in vegetated soils were lower by 50%. In contrast, water content in vegetated soil was higher by around 70% than that in a bare soil during autumn. The reason is attributed to the lower soil temperature that inhibits root water uptake ability. This was verified using a series of numerical simulations that consider effects of soil temperature on root water uptake. There was an overestimation of reduction of soil water content by around 50% in autumn period when soil temperature effects on root water uptake is ignored.

2.5 Effects of vegetation on mechanical properties of soil

Stability of soil slopes that were mechanically reinforced by plant roots has been investigated by Sonnenberg et al. (2012) at 15-g using a centrifuge. Contributions of mechanical root reinforcement were back-analyzed based on observed slip surface at failure by continuously raising groundwater table. Plant shoots including all green leaves were harvested before testing. This aimed to minimize plant transpiration and the associated induced soil suction during sample preparation and centrifuge testing. A vegetated root models to study influences of model materials and root architecture on slope stability in the centrifuge are also developed. It is noted that effects of plant induced matric suction due to transpiration are not considered.

Mahannopkul and Jotisankasa (2019) reported that the influences of root concentration and suction were investigated on Chrysopogon zizanioides (vetiver grass) root-reinforcement of clayey sand, using suction-monitored direct shear tests at four different suctions varying from zero to 50 kPa. The vetiver grass specimens were grown in containers for a year until they showed various root concentrations. Of all matric suctions, there were higher peak strength in soil samples with greater root concentrations. Unsaturated root-reinforced soils contracted while the non-reinforced soils dilated during shearing. The rate of increase in root cohesion with root concentrations was highest at the suctions around 20 kPa. The rates of increase in shear strength with suction were similar for non-reinforced soils and reinforced soils up to a threshold in root concentration beyond which the rate became slightly smaller. The infinite slope stability analysis of an instrumented slope based on field pore water pressure and mini-rhizotron measurements has been conducted employing the obtained relationships between root area ratio and strength. The analysis results showed that in unsaturated condition, the stabilizing effect of suction was greater than that of roots. However, the stabilizing effect of root reinforcement was more important especially for shallower depth in a saturated condition.

Day (1993) conducted direct shear tests to evaluate the effect of roots to soil shear strength. The results showed that the shear strength of soil with roots was greater than that of soil without roots. Wu and Watson (1998) carried out in-situ direct shear tests on plain soil and soil–root systems. It was reported that the shear strength of bare plain soil was distinctly lower than that of root-reinforced soil. A direct shear tests in laboratory to show soil penetrated by root of paper birch and lodgepole pine can significantly increase soil shear strength were conducted by Campbell and Hawkins (2003), while the degree of increase is different due to the type of soil. Similar results have also been reported by Ali and Osman (2007), Fan and Su (2008). It is noted that plant roots contribute an important increase in soil shear strength.

The effects of roots on shear strength of root-reinforced soil were investigated by employing modified direct shear tests which have been widely applied in-situ and in laboratory conditions. However, researches on employing triaxial tests for studying root-reinforced soil are relatively rare. Most of the triaxial compression tests for grass-reinforced soil focus on the reinforcement of soil with artificial materials and relatively simply accessed structures (Schlosser and Long 1974, Gray and Al-Refeai 1986). Zhang et al. (2010) conducted triaxial compression tests on re-compacted loess with artificially accessed root structures. However, as for investigations of soil-root structures utilizing triaxial compression tests, there is a limited research on coarse-grained soil, especially on coarse-grained soil with undisturbed root structures.

3 SOIL SLOPE MEASUREMENT

3.1 Introduction

The hydrological effects of vegetation have been widely experimentally investigated. However, the long-term field measurements of vegetated soil are rarely carried out. It is noted that the variations of soil parameters in unsaturated soil slopes depends on the climates (i.e solar radiation, air temperature, rainfall and snowmelt). Ng et al 2019, and Jotisankasa and Sirirattanachat (2017) presented that the soil-water characteristic curves and saturated/unsaturated coefficient of permeability of vegetated soil vary against vegetation ages. Most of past research only focused on effects of vegetation on soil hydraulic properties at particular vegetation age. Therefore, to access the long-term performance of vegetated unsaturated soil slope, long-term field measurement is needed to be carried out. In addition, past studies focused on vegetation species which are drought tolerant (*Schefflera arboricola* and *Cynodon dactylon*). Seldom have studies paid attention to vegetation species which are commonly used in the seasonal cold region.

This chapter investigated the influences of grass on long-term performance of soil slope. A field study was carried out on unsaturated soil slopes. The field measurement consisted of two neighboring cut slopes, namely bare slope and grassed slope. Soil moisture sensors, tensiometers, and thermometers are installed to studies the variations of volumetric water content, matric suction, and soil temperature at different depths and locations in unsaturated soil slopes. The meteorological station was built on the top of soil slopes to record the climate variables every 10 minutes. The meteorological data included solar radiation, air temperature, rainfall intensity, snow depth, wind speed, and relative humidity. Therefore, the changes in soil water content, matric suction, and soil temperature within two soil slopes against climate variations over the long-term period are studied.

3.2 Overview of soil slope measurement

In order to understand the grass influence on soil slopes, an instrumented field study was conducted on unsaturated soil slopes. Two neighboring cut slopes consisting of Komaoka volcanic soil were constructed in Makomanai district, Hokkaido prefecture, Japan as presented in Fig. 3.1a. Each cut slope has 6.8 m long, 4 m wide, and 4 m high. The grain size distribution and physical properties of Komaoka volcanic soil are presented in Fig. 3.2 and Table 3.1. Komaoka soil is classified as gravelly sand of fine fraction nature (SFG) according to the method of classification of geomaterials for engineering purposes (JGS 2009a). A mixture of three grass species is selected in this study, namely: Kentucky Bluegrass, Creeping Red Fescue, and Tall Fescue. These species are cold tolerant and hence widely used in a seasonal cold region like Hokkaido. The mixed-grass seeds with a density of 18 g/m^2 (Table 3.2) are chosen based on hydroseeding specification for general bio-engineering purposes in Hokkaido and uniformly germinated over the surface of one cut slope

on early of June 2016. The slopes covered with and without grass are named as “grassed slope” and “bare slope”, respectively.

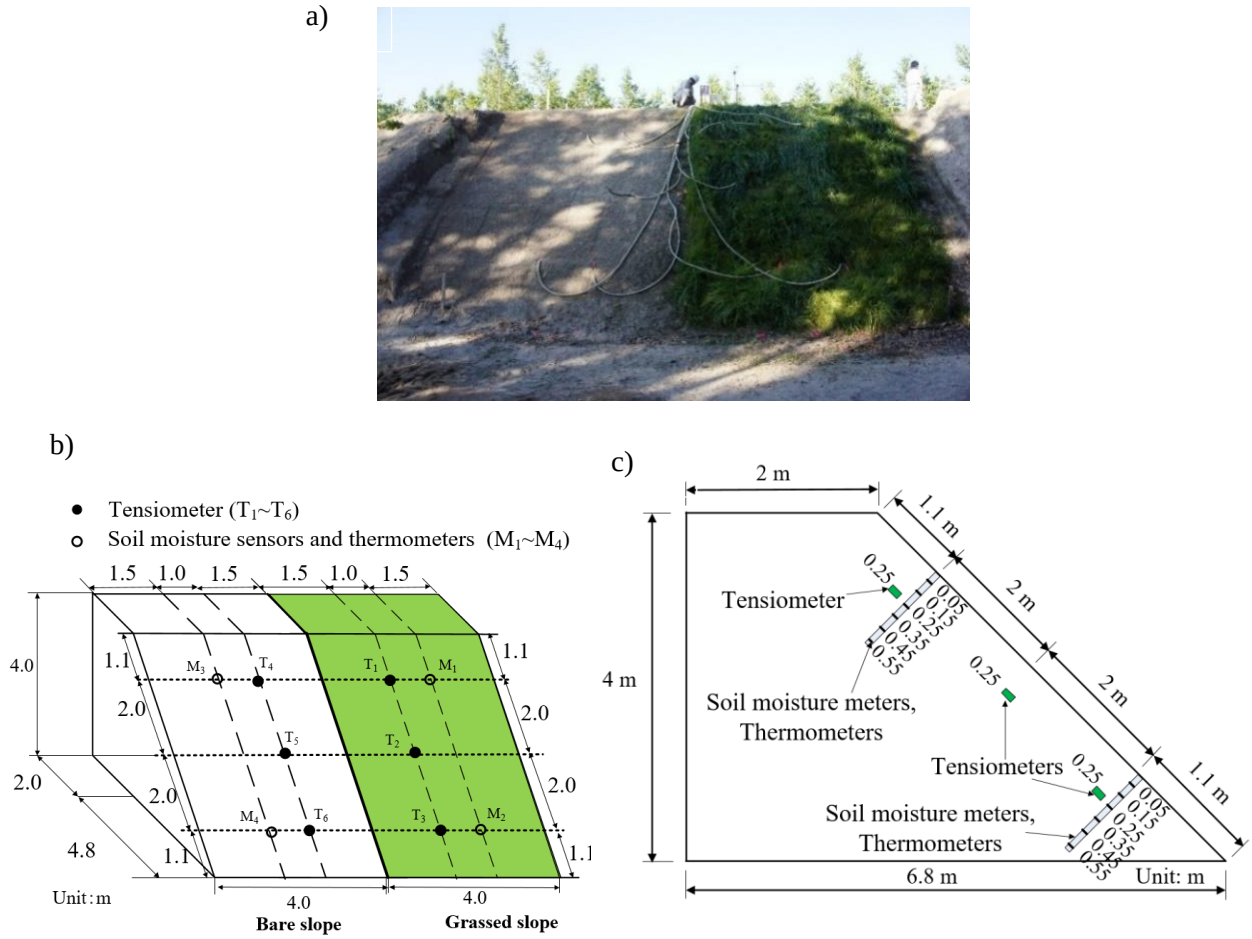

Figure 3.1 (a) Photograph of soil slopes, (b) schematic diagram of soil slopes, and (c) depths and locations of installed sensors.

The above-mentioned soil slopes were instrumented with tensiometers and soil moisture meters at different depths in order to measure the change in pore-water pressure and soil-water contents against time. The location of installing these sensors are shown in Fig. 3.1 b,c. Measurement sensors including tensiometers, soil moisture meters, thermometers were installed in two soil slopes to monitor the changes in matric suction, soil water content, and soil temperature against the variations of climate. In each soil slope, two arrays including twelve soil moisture sensors and twelve thermometers in total were installed perpendicularly to the slope surface. One array consisting of six soil moisture sensors and six thermometers (CST-SEN-DD6, Climatec Inc., Japan) were installed at the crest, while the remaining array was inserted near the toe of soil slope. These sensors were inserted at different depths varying from 0.05 m to 0.55 m. The distance between each sensor was 0.1 m. It is noted that the depths of these two types of sensors were same. Besides, three tensiometers (CHG - 2100 AET, Climatec Inc., Japan) were installed at 0.25 m depth

in the crest, center, and toe of soil slope. The locations and depths of the above-mentioned sensors are clearly illustrated in Fig. 3.2.

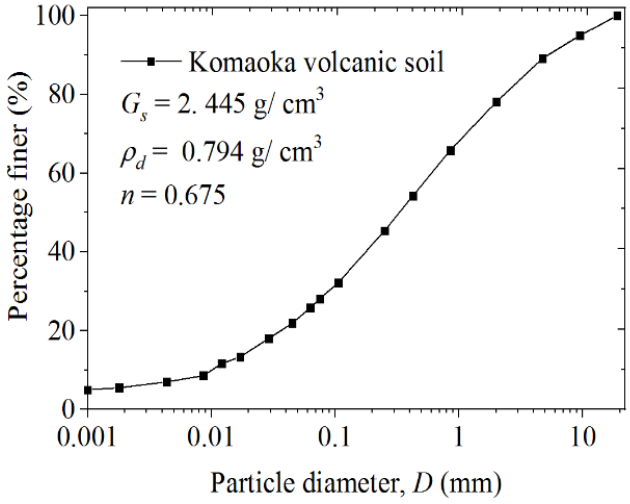

Figure 3.2 Grain size distribution of Komaoka volcanic soil.

Table 3.1 Basic properties of Komaoka soil.

Properties	Komaoka soil
Specific gravity, *Gs*	2.445
In-situ dry density, ρ_d (g/cm^3)	0.794
Maximum dry density, $\rho_{d\,max}$ (g/cm^3)	1.12
Minimum dry density, $\rho_{d\,min}$ (g/cm^3)	0.76
In-situ porosity, *n*	0.675
Mean grain size, D_{50} (mm)	0.27
Coefficient of uniformity, U_c	3.6
Fines content, F_c (%)	26.0

Table 3.2 Basic properties of a mixture of grass seeds (kg/100 m^2).

Grass seeds	Kentucky Bluegrass	Creeping Red Fescue	Tall Fescue
Weight of grass seeds (kg)	0.2	0.4	1.2

The meteorological station was built on the top of two soil slopes to record the climate variables every 10 minutes. The meteorological data included solar radiation, air temperature, rainfall intensity, snowfall, wind speed, and relative humidity are measured. In addition, two high-resolution cameras were installed to capture the change in snow depth against variations over the long-term period are studied. Therefore, the changes in soil water content, matric suction, and soil temperature within two soil slopes against climate. The time interval of collecting data was set to be 10 min. Measured results of sensors near the top of slopes and recording data from the meteorological station during 1 year from May 11th, 2017 to May 11th, 2018

are presented and discussed in this study.

3.3 Field measurements

3.3.1 Soil moisture meter and thermometers

Four sets of soil moisture meters and thermometers (CST-SEN-DD6, Climatec Inc., Japan) were installed in the same arrangement on two soil slopes as shown in Fig. 3.3. They were buried perpendicularly to the slopes at 1.1 m from the top and the foot, respectively. The lateral distance between soil moisture meter and the edge of the slope was 1.5 m. Each set was composed of 6 soil moisture meters, which measured the volumetric moisture contents at 0.05, 0.15, 0.25, 0.35, 0.45, 0.55 m depth from the ground surface. Therefore, the total monitoring points for soil moisture at each soil slope were 12. Each soil moisture meter had the size of 600 mm in length and 27.50 mm in diameter, and it was applicable for measurement under any conditions of oven dry to saturation. The area of measuring the soil moisture with a single soil moisture meter was within the radius of 100 mm around. After installing the set of soil moisture meters into a borehole at the desired location, the hollow between the soil and the instrument was filled with natural soil.

Figure 3.3 Soil moisture meter and thermometer.

3.3.2 Tensiometer

The tensiometers (CHG - 2100 AET, Climatec Inc., Japan) were installed at 0.25 m depth in the crest, center, and toe of soil slope shown in Figure 3.4 to measure the pore water pressure of the soil. In each slope, six tensiometers were buried at 0.25 m depth from the ground surface as shown in Fig. 3.4. The reading range of the tensiometer was around from 10 ~ 70 kPa. After ensuring the porous cup touched the bottom of the borehole, the Komaoka volcanic soil was filled up into the hole.

Figure 3.4 Tensiometer.

3.3.3 Temperature and humidity sensor

A small temperature/humidity sensor (CVS - HMP60HT-03C) was installed at the crest of the slopes in order to measure the temperature and humidity in the field (Fig. 3.5). The temperature and humidity are directly recording by connecting to the data logger.

Figure 3.5 Temperature and humidity sensor.

3.3.4 Solar radiation meter

The solar radiation meter (Fig. 3.6) is used in order to measure the solar radiation. It was also installed at the crest of two slopes, the reading of the solar radiation meter was integrated every 10 minutes.

Figure 3.6 Solar radiation meter.

3.3.5 Wind speed and wind direction sensors

The wind direction and wind speed sensors (CYG-3002) shown in Fig. 3.7 are used to measure wind direction and wind speed. CYG-3002 was a low-cost wind anemometer that combines a three-cup anemometer and an arrow-type wind direction gauge. This was also installed at the crest of the soil slopes.

Figure 3.7 Wind speed and wind direction sensors.

3.3.6 Rain gauge

The rain gauge (CYG-52203) shown in Fig. 3.8 is used for this study. It is the most common rain gauge that is widely used by the meteorological agency.

Figure 3.8 Rain gauge.

3.4 Results and discussions

3.4.1 Meteorological data

Fig. 3.9 presents meteorological data during 1 year. Solar radiation was relatively similar from 2017 May to 2017 July (25 $MJ.m^{-2}.day^{-1}$), then significantly decreased to somewhere in the vicinity of 2 $MJ.m^{-2}.day^{-1}$ in 2018 January. After that, the solar radiation rose dramatically until 2018 May. Relatively low rainfall events were observed. Rainfall events mainly occurred from 2017 September to 2018 March. The wind speed varied from 1.2 to 8.2 m/s. After increasing from 2017 May (13 °C) to2017 July (26 °C), air temperature dropped to minimum value of about -11 °C in 2018 January. Next, it was increased until the end of presented period. The general trend of relative humidity was similar to that of air temperature. However, the daily changing pattern of air temperature was in general opposite to the pattern for minimum relative humidity. When the air temperature was high, the low value of humidity was observed. Snowfall happened from November 17th, 2017 when the temperature was below 0 °C. After reaching the maximum depth of 89 cm on March 2nd, 2017, snow began to melt due to the rise in both air temperature and solar radiation hence the snow depth was dramatically decreased from March 2nd, 2017 to March 31st, 2017.

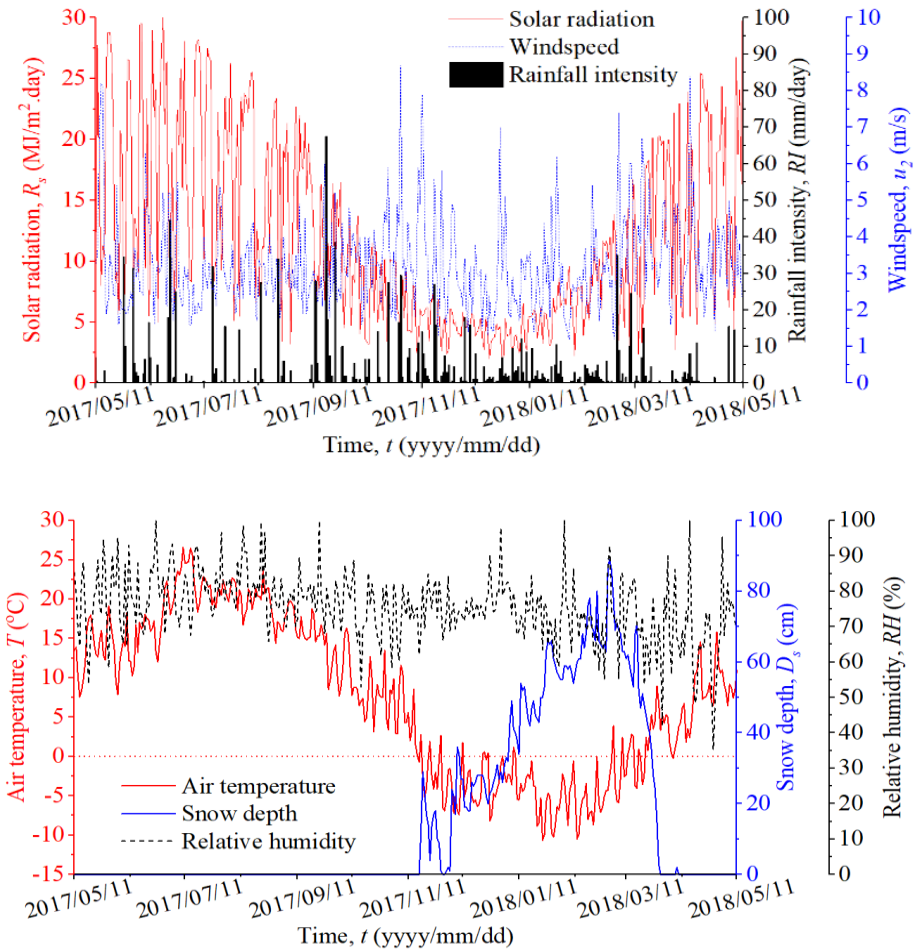

Figure 3.9 Meteorological data from 11 May 2017 to 11 May 2018.

3.4.2 Volumetric water content

The measured volumetric water contents (VWCs) of bare slope and grassed slope are demonstrated in Fig. 3.10. The volumetric water content in bare slope increased linearly from the surface to 0.35 m before remaining unchanged at about 26% at the greater depths. The volumetric water content in grassed slope was lower than in bare slope within the depth lower than around 0.55 m because the grassed not only minimized the rainfall infiltration (Nguyen at al. 2020) but also extracted water from the soil through transpiration process. There was an equal volumetric water content at the 0.55m depth between bare slope and grassed slope.

Fig. 3.11 compared the variations of volumetric water content at 0.05 m depth between bare slope and grassed slope. The VWC in bare slope doubled as compared to that from grassed slope. Furthermore, there was highly fluctuated in VWC under rain and snowmelt infiltration in the former, while the VWC in the latter was much stable. The VWC of the bare slope dramatically rise by nearly 30% (from 7.4 % to 20.2 %) due to snowmelt infiltration on March 3rd, 2018. However, there was an increase by 15% (3.7% to 5.6%) on the same date in VWC of grassed slope.

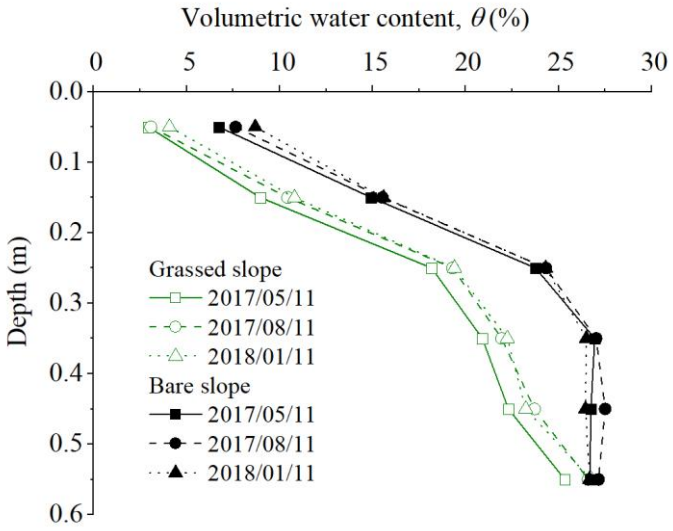

Figure 3.10 Volumetric water content along depth of bare slope and grassed slope.

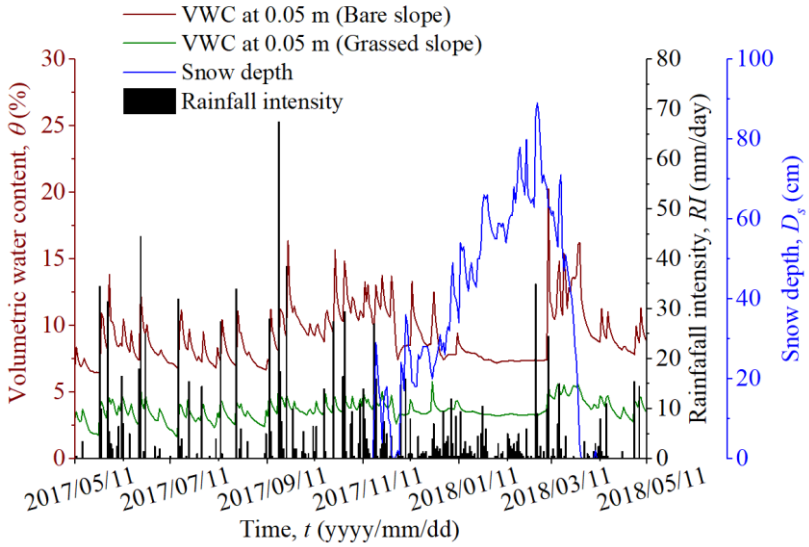

Figure 3.11 Variations of VWC at 0.05 m depth of bare slope and grassed slope with time.

3.4.3 Matric suction

The comparison in matric suction at 0.25 m depth between bare slope and grassed slope is indicated in Fig. 3.12. Matric suctions in both bare soil and grassed soil decreased in the middle of 2017 June because many rainfall events happened. After that, the matric suctions in two soil slopes increased rapidly until 2017 August because there were few rainfall events. The relatively high solar radiation and air temperature also led to a high amount of moisture flowing from the ground to the atmosphere. The dramatic increase in matric suction of grassed slope was attributed to the transpiration process. The low solar radiation and low air temperature, as well as the occurrent of several light rainfall events in 2017 September to the end of 2017 October caused a drop in matric suction.

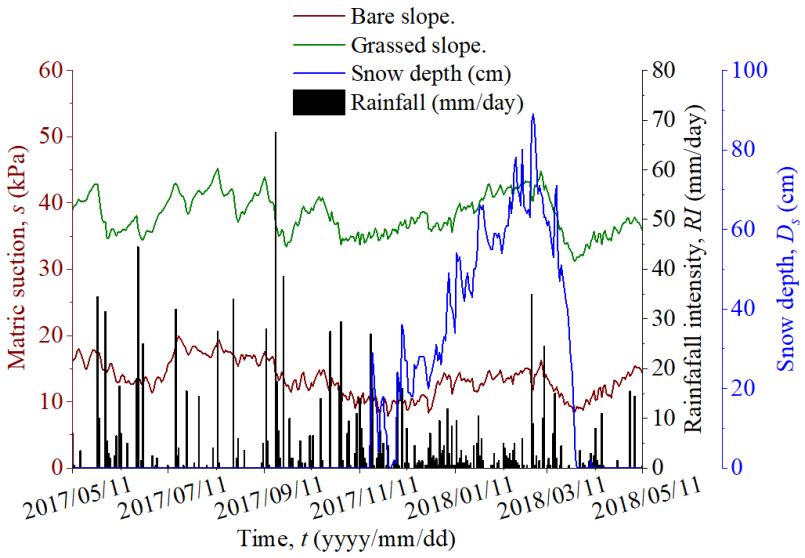

Figure 3.12 Soil suction at 25 cm depth of bare slope and grassed slope.

The grassed slope always remained higher matric suction as compared to the bare slope. This is corresponding to the lower volumetric water content in a shallow depth of grassed slope compared to that in bare slope as have mentioned previously. In addition, the vegetated soil has higher matric suction than bare soil due to the differences in soil water characteristic curves (Ng. et al 2016, Nguyen et al. 2020). It is noted that the gap in matric suction between grassed slope and bare slope was greater in winter season with the occurrence of snow. There are two reasons for the differences in matric suction due to the grass root existence. The first reason is that the soil pores are occupied by grass roots hence the diameters of soil pores are reduced hence matric suction is increased due to the capillary law (Scanlan and Hinz, 2010). Another reason might be attributed to the exudates released by grass roots (Carminati et al, 2016). Since the effect of grass roots on reducing soil pore was similar in both warm and winter seasons, the enhanced matric suction under the snow cover might be mainly attributed to the second reason. The exudates might be released more by grass roots in winter. This explanation is not yet conclusive. However, it should be noted that this phenomenon has been occurring and repeated for continuously 3 winters (from winter of 2017 to winter of 2019).

3.4.4 Ground temperature

Daily soil temperatures of the bare slope and the grassed slope at different depths are shown in Fig. 3.13. In warm season when the air temperature and solar radiation were relatively high, the daily soil temperature in bare slope was higher than grassed slope. The reason was because of the grass leaves partially prevented the net radiation from reaching to heat the soil. There was an increase in daily soil temperature from 2017 May to 2017 August before reducing to about lower than 2 ºC in 2018 January. This observation was consistent with the trend of solar radiation and air temperature as shown in Figure 3.9.

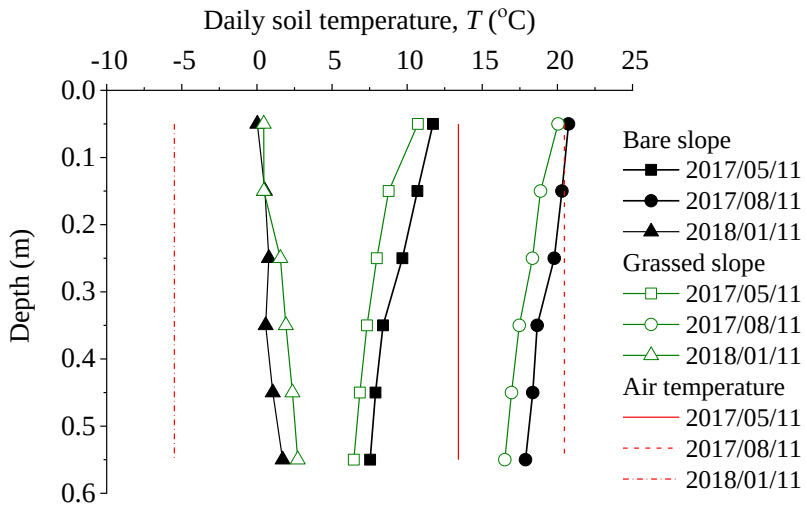

Figure 3.13 Change in the ground temperature at different depths at the lower side of bare and grassed soil slopes.

The variations in daily soil temperature at 0.05 m in both bare slope and grassed slope during period of one year is indicated in Fig. 3.14. There was a higher daily soil temperature in bare slope from 2017 May to 2017 July. The daily soil temperatures in two slopes were contracted from December 10th, 2017 to April 3rd, 2018. This phenomenon happened as the air temperature and solar radiation are lower than 16 °C and 16 MJ.m^{-2}.day^{-1}, and 5 °C and 2.7 MJ.m^{-2}.day^{-1}, respectively. When the air temperature dropped below 0 °C, the daily soil temperature in bare slope remained constant at nearly 0 °C. Whereas there was a slightly higher in daily soil temperature of grassed slope. The reason was also due to grass leaves which provided heat insulation effect. Rui et al. 2018 also presented that the grass leaves has heat insulation property to a certain extent in winter hence the frost depth in grassed slope was lower than bare slope.

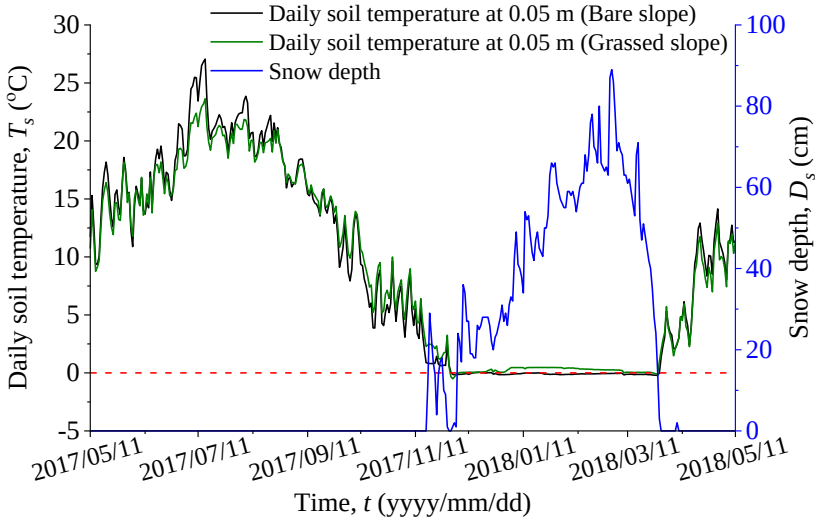

Figure 3.14 Variations of soil temperature at 0.05 m depth of bare slope and grassed slope with time.

In a seasonal cold region like Hokkaido**,** freeze-thaw action resulted in a decrease in shear strength and stiffness of volcanic soil (Ishikawa and Miura, 2011). Since grassed slope was not frozen in snowy season, the shear strength of grassed soil might not be affected by freeze-thaw action. In contrast, shear strength of bare soil might decrease. As a result, the shallow stability of grassed slope might be higher as compared to bare slope.

3.5 Summary

From the above measurement results, it was clear that the grass cover had significant influences on retaining higher matric suction into unsaturated soil slope. The volumetric water content into grassed soil slope was also lower than in bare soil slope. Furthermore, the volumetric water content in the grassed slope is less fluctuated against rainfall infiltration than in bare slope, especially when the snowmelt occurs.

The field measurement also showed that matric suction in grassed slope was higher than bare slope. The higher matric suction was corresponding to the lower volumetric water contents in the former. The reason was the differences in soil hydraulic properties (SWCC and saturated/unsaturated coefficient of permeability). Another attributable reason was the transpiration due to grass-soil-atmosphere interaction. The gap of matric suction between grassed slope and bare slope was greater in snowy season. It might be because more exudates were released by grass roots. The capacity to retain higher matric suction in grassed slope increased the stability of unsaturated soil slope by enhancing the shear strength of soil.

In warm seasons, lower daily soil temperature was observed in grassed slope as compared to bare slope. The reason was that the grass leaves intercepted net radiation by shading the ground surface. In contrast, there was a higher daily soil temperature in the grassed slope in winter due to the insulation of grass leaves. Since the soil temperature in grassed slope was higher than 0° C in snowy season, the shear strength of grassed soil was not be affected by freeze-thaw action. However, as the soil temperature near the slope surface of bare slope was around 0° C, shear strength of bare soil might be reduced because of freeze-thaw effects. Therefore, the shallow stability of grassed slope might be higher than that of bare slope.

4 SATURATED HYDRAYLIC PROPERTIES OF GRASSED SOIL

4.1 Introduction

The vegetation age and vegetation species play a key role in the effects on hydraulic properties of soil. Leung et al. (2018) quantified the effects of vegetation ages for two distinct vegetation types (willow and grass) on the infiltration rate. It was reported that the increase in vegetation age resulted in a faster infiltration rate for willowed soil than that for grassed soil. Song et al. (2017) presented the opposite effects of two distinct grass species even though the same soil was used. The saturated coefficient of permeability of Vetiver grassed soil was significantly higher than that of bare soil. However, the formation of macro-pores due to the decayed roots (Ghestem et al., 2011; Ng et al., 2016b) and the preferential flow due to vegetation roots (Li et al., 2016) leads to the contrasting result. Furthermore, the saturated coefficient of permeability of vegetated soil varied with grass age (Ng et al. 2019). The saturated coefficient of permeability of grassed soil was similar to bare soil during the first six months of transplantation. After that, it was slightly decreased for the next three months. In contrast, it was increased after transplantation for around 12 months due to evidently root decays. Therefore, this chapter investigated the saturated coefficient of permeability of grassed soil with different grass ages. The permeability test apparatus was employed to investigate the relationship between root content (i.e. root volume ratio) and saturated coefficient of permeability of grassed soil with different grass age.

4.2 Soil types and grass species

4.2.1 Soil types

Komaoka soil and Toyoura sand are used as test materials in this study. Komaoka soil is a coarse-grained volcanic soil, which is widely distributed in Hokkaido, Japan. Besides, Toyoura sand is commonly used as the Japanese standard sand. The grain-size distribution of Komaoka soil and Toyoura sand is indicated in Fig. 4.1.

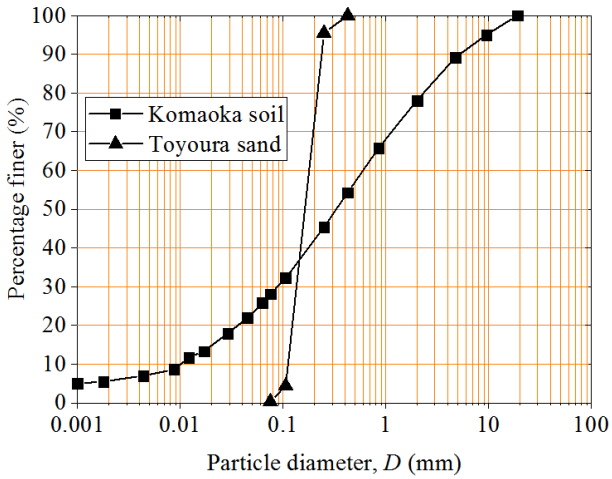

Figure 4.1 Grain size distribution curves of Komaoka soil and Toyoura sand.

Komaoka soil and Toyoura sand are classified as gravelly sand of fine fraction nature (SFG) and sand (S) according to the method of classification of geomaterials for engineering purposes (JGS 2009a). Table 4.1 presents the physical properties of Komaoka soil, Toyoura sand, and a mixture of grass seeds.

4.2.2 Grass species

A mixture of three grass species is selected in this study, namely: Kentucky Bluegrass, Creeping Red Fescue, and Tall Fescue as similar to that from field measurement. The mixed-grass seeds with a density of 18 g/m^2 as shown in Table 3.2 are chosen. The purpose of using the same soil and same grass species is to investigate the hydraulic properties (i.e. saturated coefficient of permeability) of bare soil and grassed soil which will be expected to clearly explain the differences in volumetric water content and matric suction observed in filed measurement. Besides, the parameters related to seepage analysis (i.e. saturated coefficient of permeability) will be employed as input data in numerical simulation which will be discussed later.

Table 4.1 Basic properties of Toyoura sand, Komaoka soil, and a mixture of grass seeds.

Properties	Komaoka soil	Toyoura sand
Specific gravity, *Gs*	2.445	2.65
In-situ dry density, ρ_d (g/cm^3)	0.794	1.56
Maximum dry density, $\rho_{d\,max}$ (g/cm^3)	1.12	1.63
Minimum dry density, $\rho_{d\,min}$ (g/cm^3)	0.76	1.37
In-situ porosity, *n*	0.675	0.412
In-situ volumetric water content, θ_n (%)	24.5	--
Mean grain size, D_{50} (mm)	0.27	0.18
Coefficient of uniformity, U_c	3.6	1.5
Fines content, F_c (%)	26.0	0

4.3 Overview of permeability test apparatus

A schematic diagram of the permeability test apparatus is shown in Fig. 4.2a. The constant head method is adapted to determine the saturated coefficient of permeability of soil. Whereas instantaneous profile method is employed to calculate the unsaturated coefficient of permeability of soil. Pore-water pressure and water content at two ends of soil specimen are measured and hence hydraulic head gradient and flow rate are obtained, which are in turns used to compute the hydraulic permeability at the central point of specimen (Mori, 2016).

The size of the specimen in this permeability test is 100 mm in diameter and 120 mm in height. The size of the soil specimen is adequate for the requirement of a permeability test apparatus (JGS 2009b). Tensiometer (ML2100-AM6, Mol Ltd., Japan) and soil moisture sensor (ML3 ThetaProbe, Delta-T Devices

Ltd., UK) are used to measure the pore water pressure at the center of soil specimen (Fig.4.2). Tensiometer can measure the pore-water pressure in the range from -90 kPa to 0 kPa. The measured negative pore-water pressure is numerically equal to matric suction since the pore-air pressure is assumed atmospheric. The ceramic tip and its tube are fully saturated with distilled water before installing a tensiometer. In addition, the pore water pressure at the top and bottom of soil specimen are recorded by two pressure transducers, which connect with two ends of soil specimen through ceramic disks with a diameter of 20 mm.

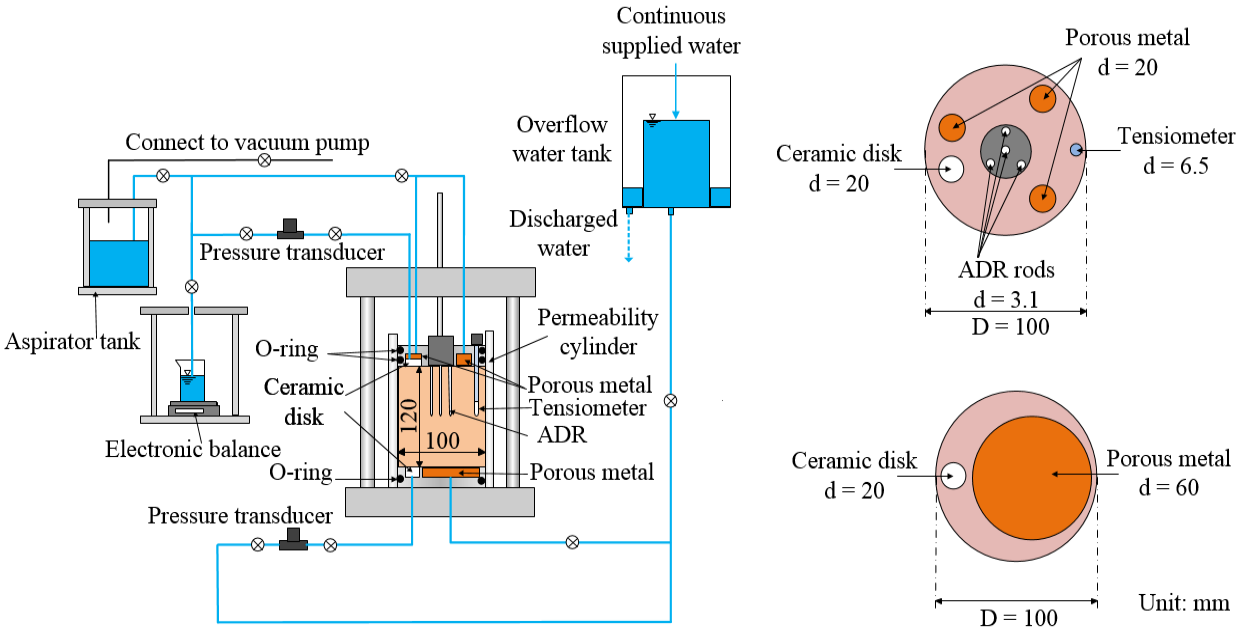

Figure 4.2 (a) Schematic diagram, (b) cross-section of the cap, and (c) cross-section of pedestal of permeability test apparatus.

The overflow water tank contains two concentric cylinders. Water is continuously supplied to the inner cylinder. Any rise in water over the top of the inner cylinder is collected and discharged by the outer cylinder. Therefore, the water head in the inner cylinder of overflow water tank remains constant. Water is continuously supplied to soil specimens from the overflow water tank. The drainage water is collected and automatically recorded by electronic balance. It is placed in a chamber to avoid any influence from the surrounding environment, which might cause errors in the measurement of drainage water. Three porous metals with a diameter of 20 mm are uniformly distributed in the cap (Fig. 4.2b). Moreover, a pedestal of the permeability test apparatus is equipped with a porous metal with a diameter of 60 mm (Fig. 4.2c).

4.4 Soil specimen preparation

The PVC mold with an internal diameter of 100 mm and height of 150 mm were used to prepare the soil specimens. The PVC mold was pre-cut along the axial axis and held with tapes and clamps which were later released when the soil specimens were removed for testing (Sauceda et al., 2014). Komaoka soil with volumetric water content of 24.5% was mixed by quartering method (JGS 2009b) to establish the identical

soil water content and uniformity in grain-size distribution. Next, the air pluviation method and slight compaction were employed to make Komaoka soil specimen into four layers (i.e. 30 mm in height each). Good contact between each layer is provided by scarifying its soil surface after preparing. As a result, the soil specimens have the same in-situ porosity and in-situ dry density as presented in Table 4.1. These soil properties are similar to those of the cut slopes constructed at Makomanai district, Hokkaido, Japan for long-term field measurement (Nguyen et al., 2019). After that, the mixture of grass seeds was uniformly germinated on the surface of Komaoka soil specimens.

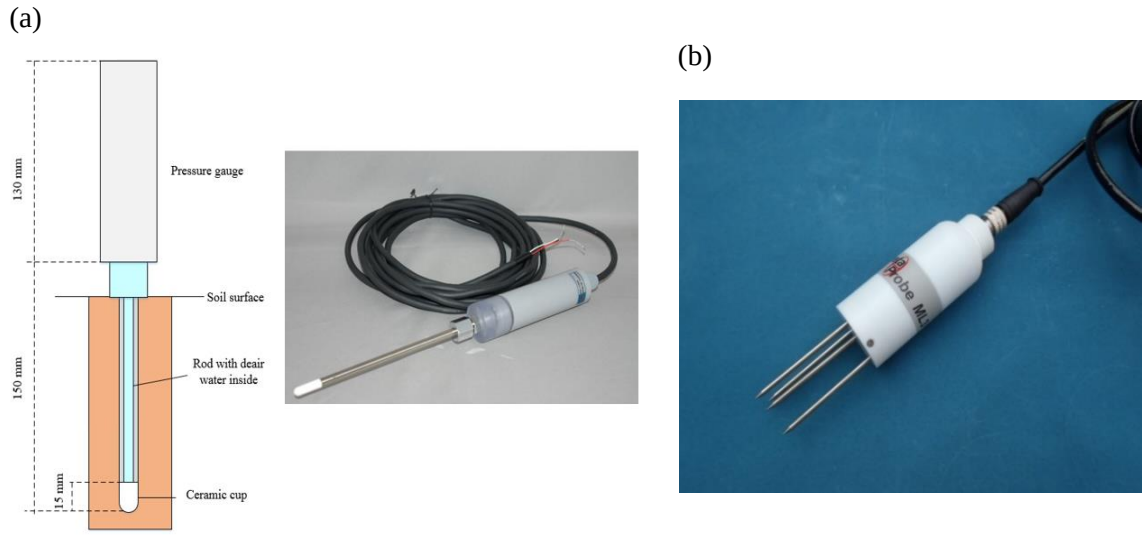

Figure 4.3 (a) Schematic diagram of the tensiometer and (b) soil moisture sensor.

All soil specimens were placed inside growth room with regulated temperature (around 25 ºC), and daily irrigation for three weeks. In addition, the fluorescent bulbs were used to simulate daylight. This growth condition was to shorten the time demanded for growth (Sauceda et al., 2014). The soil specimens then were placed outdoor in which climatic elements (e.g. solar radiation, heat, rainfall, humidity) were provided. The irrigations were applied frequently every 2 days to provide sufficient water content for root growth. No fertilizer was added to the soil to prevent any induced osmotic suction due to the different solute concentrations in pore water (Krahn and Fredlund, 1972). When the grasses have grown to a certain age varying from 1 month to 6 months, the soil specimens were brought to laboratory and placed on the porous stone for two days for internal drainage. This procedure is to minimize any influence of freeze-thaw effect on saturated coefficient of permeability. It was followed by cutting grass shoots carefully before putting soil specimens into refrigerator for 12 hours. The mold was then released after moving out soil specimen from refrigerator. Next, soil specimen was accommodated into cylinder of permeability test apparatus. The examples of grassed soil specimens and grass roots are presented in Fig. 4.4.

(a) (b)

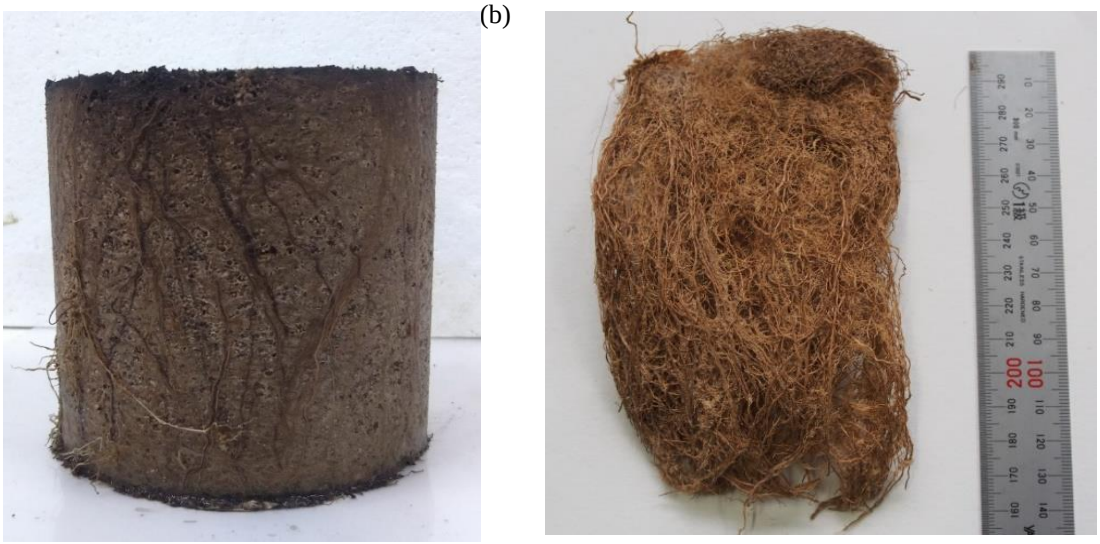

Figure 4.4 Examples of (a) grassed soil specimen, and (b) grassroots of permeability test.

Any gap between the soil specimen and permeability cylinder was sealed by pasting a thin layer of vacuum grease along the internal surface of the permeability cylinder so that any water leakage was prevented. A process of soil specimen preparation is illustrated in Fig. 4.5. By preparing the soil specimens following this method, the disturbances of obtaining vegetated soil samples might be significantly minimized.

4.5 Experiment procedures

A series of saturated permeability tests were performed for grassed soils with the growing age of 1, 2, 3, 4, 5, 6 months and bare soil. Three replicates were conducted for each test. Firstly, the water-saturated filters with a diameter of 100 mm were placed on the bottom and top of soil specimens. The cap equipped with a soil moisture sensor and tensiometer was inserted to measure the volumetric water content and matric suction at the center of soil specimen. The procedures suggested by Ng and Pang (2000) were carried out to increase the degree of saturation of soil specimens. After installing the cap, the soil specimen was submerged in deaired water which was supplied through the pedestal from the overflow water tank. In addition, a negative pore water pressure of -2 kPa was applied on the cap for 24 hours. This saturation process was completed when no bubbles were observed in aspirator tank. The soil moistures sensor, tensiometer, and two pressure transducers recorded the outputs (in voltages) when the soil specimens are inserted in permeability cylinder. The degree of saturation for soil specimens was as high as 92 % by adopting this saturation procedure. After that, water was supplied from the overwater tank to the soil specimen through porous metal and ceramic disk at the pedestal. The hydraulic head difference (h) between surface water in the overflow tank and top of soil specimens was 300 mm. The water was freely drained through three porous metals and a ceramic disk on the cap of test apparatus before collecting and weighting by a cup placing on electronic balance. The coefficient of permeability of saturated soil was calculated as

follows (JGS 2009c).

$$k_s = \frac{L}{h}\frac{Q}{A(t_2 - t_1)} \tag{4.1}$$

where, k_s (m/s) is saturated coefficient of permeability of soil, L (0.12 m) is specimen length; Q (m^3) is the volume of water flowing through the soil specimen and measured by electronic balance during a particular elapsed time; A (7.85E-5 m^2) is the cross-sectional area of the soil specimen; and t_1, t_2 (s) are measurement time.

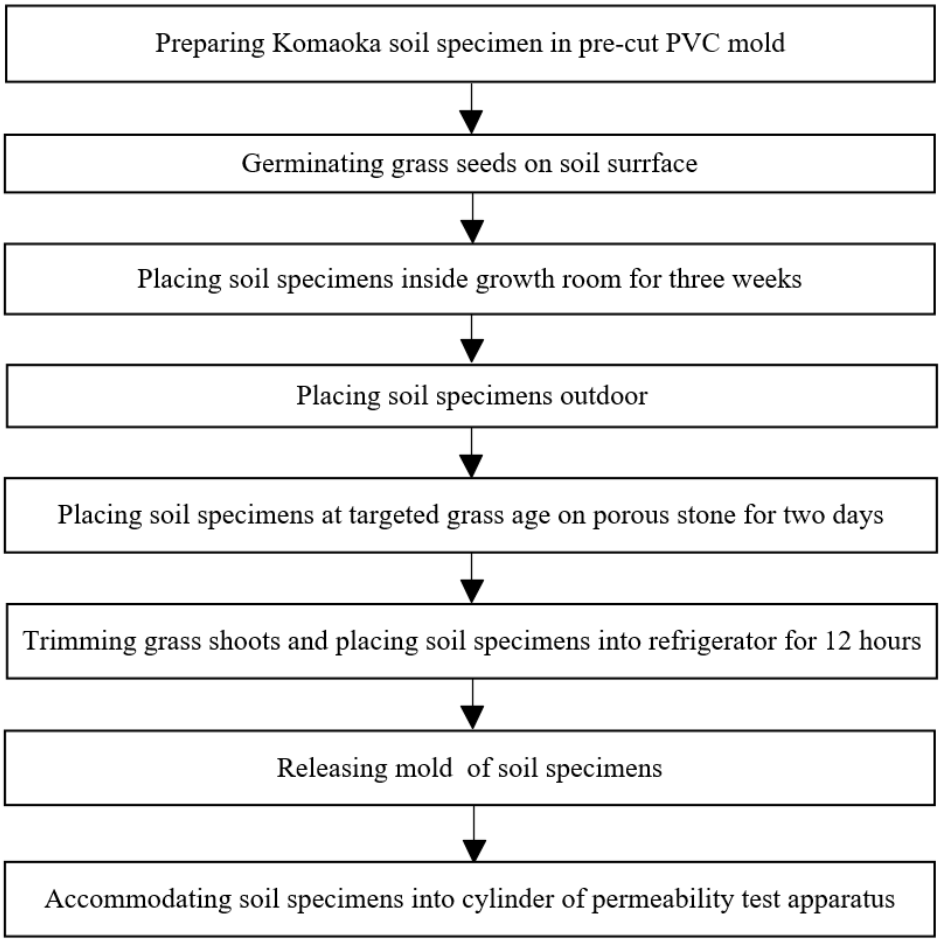

Figure 4.5 Process of preparing soil specimens for permeability test.

After conducting the permeability test, grassed soil specimens were carefully removed from test apparatus and the soil attached with roots was washed away with care according to the standardized root washing procedures adopted by Smucker et al. (1982). These roots were then air-dried at room temperature (around 25 ºC) until the root biomass remains constant. After that, the volume of grassroots was quantified by the actual volume displacement approach. The volume of grassroots was measured by the volume of water displaced when it was submerged in water in a graduated cylinder (Novoselov, 1960). The air-dried method was adopted to measure root biomass instead of the oven-dried method. The reason was to prevent the roots

from breaking into small pieces, which in turn might reduce the accuracy in the measurement of root volume. The root contents were measured in terms of 'root biomass per soil volume ρ_R (kg/m^3)' and 'root volume ratio, R_v (m^3/ m^3)' in this study.

4.6 Results and discussions

The saturated coefficients of permeability of grassed soils with different ages and bare soil obtained by the permeability tests are illustrated in Fig. 4.6a. It can be seen that the saturated coefficient of permeability of grassed soil with higher grass age is lower than that with lower grass age. The reason for this phenomenon is that the root volume ratio increases with the rise of grass age as can be seen in Fig. 4.6b, hence more soil pores are clogged by grass roots. In another word, the flow channels are significantly blocked due to the increase in the root void ratio. An additional reason is that the exudates lead to the higher viscosity of the liquid phase. Moreover, the adhesive properties of exudates result in the links between exudates and soil particles (Kroener et al., 2014).

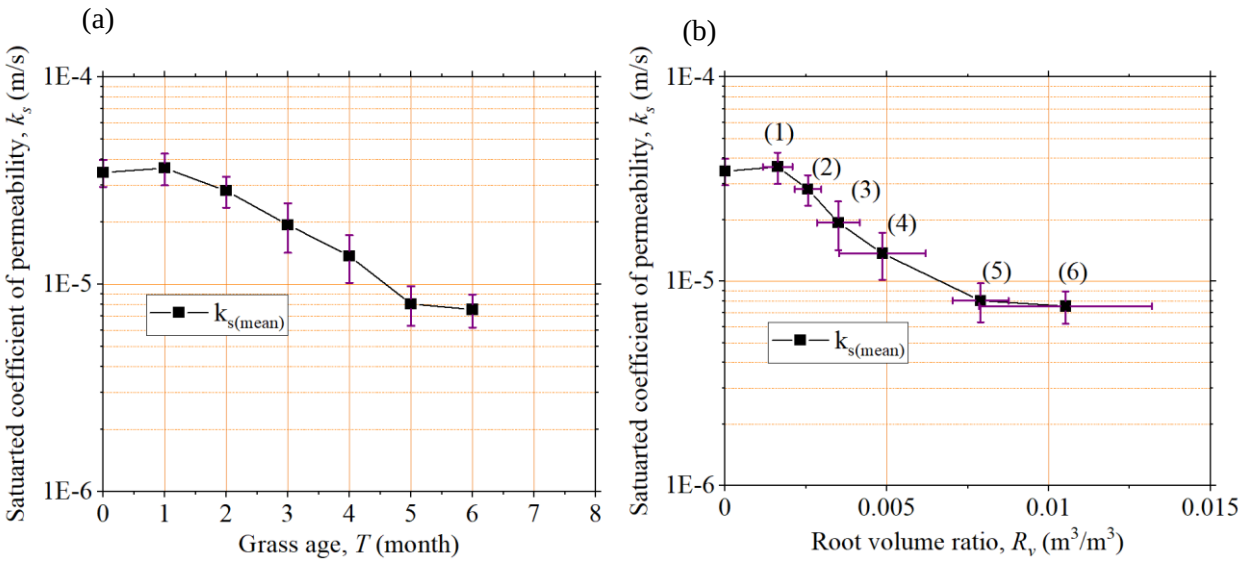

Figure 4.6 Relationship between the saturated coefficient of permeability of grassed soils (a) versus grass age, and (b) versus root volume ratio. (Number in brackets represents grass age).

The increase in the root volume ratio might be associated with the rise in water viscosity and adhesive properties. These phenomena also contribute to the decrease in the saturated coefficient of permeability. The saturated coefficient of permeability of grassed soil decreases from 3.46 E-5 m/s in the second month to 8.04 E-6 m/s in the fifth month. There is a relatively similar in the saturated coefficient of permeability of grassed soil in six months to that of the fifth months even though the root biomass per soil volume and root volume ratio are higher in the latter. When the grass-root volume ratio reaches 7.89E-3 m^3/m^3, any increase in root contents might have less influence on reducing the saturated coefficient of permeability.

The results of the saturated coefficient of permeability and root contents are summarized in Table 4.2. Mean ($\overline{X}$) and standard deviation (*S.D*) are computed by Eqs. 4.2 and 4.3.

$$\overline{X} = \frac{\sum_{i=1}^{n} X_i}{n-1} \tag{4.2}$$

where X_i is one sample value; $\overline{X}$ is the mean of all values; and n is the sample size.

$$S.D = \sqrt{\frac{\sum_{i=1}^{n} (X_i - \overline{X})^2}{n-1}} \tag{4.3}$$

Table 4.2 Descriptions and the results of permeability tests.

Test No.	Age of grass (months)	Root biomass per soil volume, ρ_R (kg/m^3)	Root volume ratio, R_v (m^3/m^3)	Saturated coefficient of permeability (m/s)
BK	0	0	0	2.92E-5, 3.52E-5, 3.94E-5
		Mean: 0	Mean: 0	Mean: 3.46E-5
		S.D.: ±0	S.D.: ±0	S.D.: ± 5.13E-6
GK-1	1	0.44, 0.62, 0.71	1.3E-3, 1.6E-3, 2.1E-3	3.07E-5, 3.50E-5, 4.32E-5
		Mean: 0.59	Mean: 1.62E-3	Mean: 3.63E-5
		S.D.: ±0.13	S.D.: ±4.5E-4	S.D.: ±6.35E-6
GK-2	2	0.81, 0.85, 1.09	2.2E-3, 2.6E-3, 3.0E-3	2.32E-5, 2.86E-5, 3.28E-5
		Mean: 0.92	Mean: 2.56E-3	Mean: 2.82E-5
		S.D.: ±0.15	S.D.: ±4.1E-4	S.D.: ±4.79E-6
GK-3	3	0.99, 1.29,1.67	2.9E-3, 3.4E-3, 4.2E-3	1.52E-5, 1.77E-5, 2.52E-5
		Mean: 1.32	Mean: 3.5E-3	Mean: 1.94E-5
		S.D.: ±0.33	S.D.: ±6.6E-4	S.D.: ±5.20E-6
GK-4	4	1.19, 1.81, 2.65	3.9E-3, 4.6E-3, 6.9E-3	9.86E-6,1.44E-5,1.68E-5
		Mean: 1.88	Mean: 4.86E-3	Mean: 1.37E-5
		S.D.: ±0.73	S.D.: ±1.34E-3	S.D.: ±3.53E-6
GK-5	5	2.66, 2.67, 3.20	7.2E-3, 7.6E-3, 8.9E-3	6.42E-6, 7.82E-6, 9.88E-6
		Mean: 2.84	Mean: 7.89E-3	Mean: 8.04E-6
		S.D.: ±0.30	S.D: ±8.6E-4	S.D.: ±1.74E-6
GK-6	6	3.56, 3.62, 5.71	8.8E-3, 9.1E-3, 1.4E-2	6.13E-6 ,7.67E-6, 8.86E-6
		Mean: 4.30	Mean: 1.05E-2	Mean: 7.55E-6
		S.D.: ±1.22	S.D.: ±2.7E-3	S.D.: ±1.37E-6

S.D. stands for standard deviation

4.7 Summary

This chapter studies the effect of grass age on the saturated coefficient of permeability of soil by employed the permeability test apparatus. The constant head method was used to compute the saturated coefficient of permeability. It was worth noting that the method proposed by Ng and. Pan (2000) was effective to increase the degree of saturation of soil specimens (as high as 92%). The experimental results presented that the saturated coefficient of permeability of grassed soil was lower than bare soil and it was decreased with the increase in grass age. The reason for this phenomenon was attributed to the higher root volume ratio (R_v). Since more soil pores are clogged by grass roots, the flow channels were blocked due to the increase in the root void ratio. An additional reason was that the exudates, which were released by grass roots, lead to the higher viscosity of the liquid phase.

5 UNSATURATED HYDRAULIC PROPERTIES OF GRASSED SOIL

5.1 Introduction

The improper SWCC and saturated/unsaturated coefficient of permeability of vegetated soil caused less agreement between numerical simulation and field measurement for the soil near the slope surface (Cui et al., 2005). Quantifying the hydraulic properties of soil with different vegetated ages is vital to predict the long-term performance of vegetated soil slope. However, measuring the SWCC and unsaturated coefficient of permeability of soils is time-consuming and costly. Ng et al. (2016a) proposed a new and simple model for estimating the soil-water characteristic curves of root-permeated soils. Currently, the simple model to estimate the unsaturated coefficient of vegetated soil is not available. Therefore, this chapter investigated the effects of grass age on unsaturated hydraulic properties (i.e. SWCC and unsaturated coefficient of permeability) and seepage behaviors (i.e. outflow, runoff, and the variations in volumetric water content/matric suction) of unsaturated Komaoka volcanic soil by performing column tests. Based on the results of SWCCs and unsaturated coefficient of permeability of grassed soil, the estimation model for the later will be proposed and validated in the next chapter.

5.2 Overview of column test apparatus

The schematic diagram of the column test apparatus is presented in Fig. 5.1. It contains transparent acrylic cylinders with a total height of 1000 mm and an internal diameter of 200 mm. These cylinders are connected by O-rings and bolts. The height of Toyoura sand layer is 500 mm, which is placed from an elevation of 0 mm to 500 mm. It is overlain by bare soil or grassed soil, which has a thickness of 150 mm. There is a porous metal with 30 mm in height and 200 mm in diameter at the bottom of the cylinder to allow water flow out freely.

Two tensiometers (ML2100-AM6, Mol Ltd., Japan) are installed through two pre-drilled holes in the column test apparatus at an elevation of 525 mm and 625 mm to measure the pore-water pressure of soil specimen. There are rubber O-rings in two drilled holes to prevent water from leakage through the connection. Besides, EC-5 (Decagon Devices Inc, USA) is employed as soil moisture sensors to measure the soil water content (Fig. 5.2). Seven soil moisture sensors are installed at depths of 75, 175, 275, 375, 475, 525, and 625 mm to investigate the variations in volumetric water content against time. Five soil moisture sensors are buried at desired depths in the Toyoura sand while the remaining two soil moisture sensors are inserted at the same depths as the above-mentioned two tensiometers. Soil moisture sensors were calibrated for both bare soil and grassed soils. Fig. 5.3 indicated that the grass roots slightly affect the relationship between sensor output (in voltage) and volumetric water content. Silicon is pasted on the drilled holes at the wall of the cylinder after inserting soil moisture sensors to form a good seal.

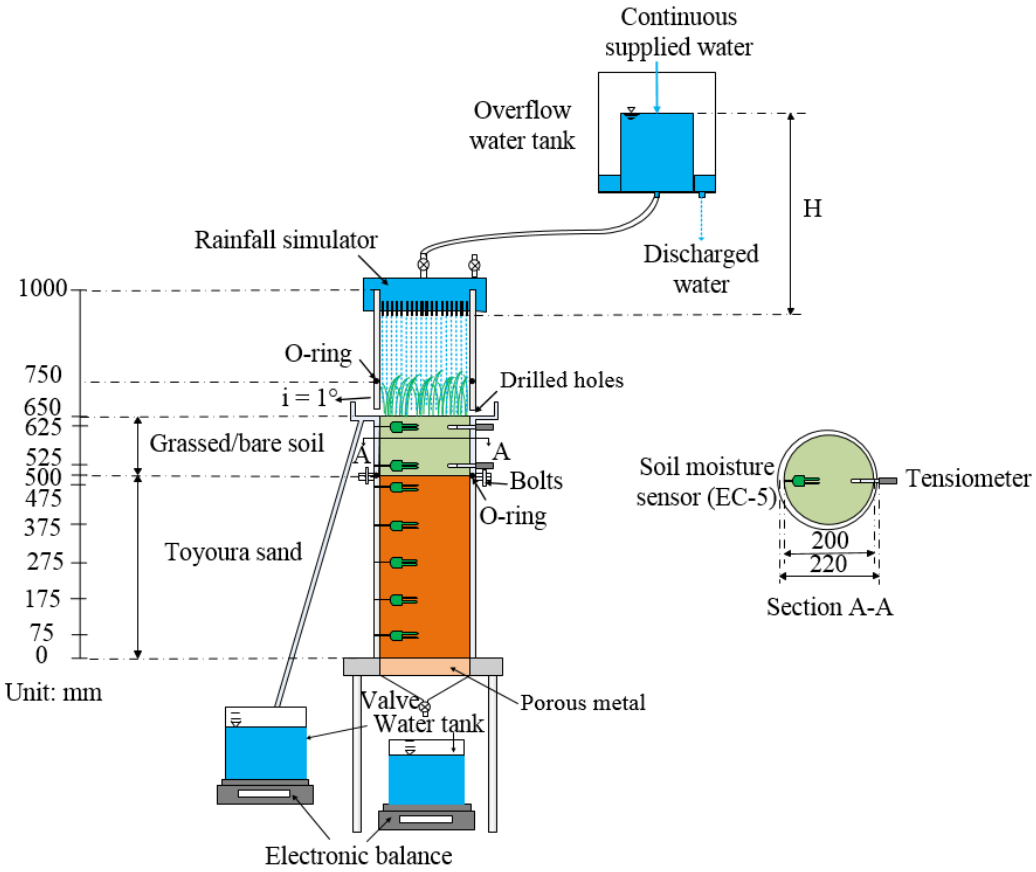

Figure 5.1 Schematic diagram of the column test apparatus.

Rainfall events are simulated by a newly developed rainfall simulator (Fig. 5.4) which was placed on the top of the column test apparatus. The rainfall simulator is 265 mm in diameter and 63 mm in height. It is equipped with 312 hypodermic needles which have inner diameter of 0.15 mm. These hypodermic needles are arranged in concentric circles and uniformly distributed. The distance between each hypodermic needle is 10 mm. The arrangement of hypodermic needles is to create uniformly distributed raindrops over the soil surface. The raindrop size of 3.5 mm in diameter is produced when water drops out from the end of needle. The rainfall simulator is connected to the overflow water tank through the tube at its center, while another tube is placed at the side to eliminate any air trapped in the rainfall simulator. Different rainfall intensities are created by changing the hydraulic head difference between rainfall simulator and overflow water tank (i.e. *H* in Fig. 5.1). The rainfall simulator can simulate rainfall intensity varying from 5 mm/h to 200 mm/h.

In order to measure the runoff during rainfall, eight small holes with each diameter of 15 mm are drilled on the side at the ground surface (650 mm). When the rainfall occurs, runoff flows out through eight small holes and goes across the tube before collecting by a tank. By using the electronic balance to measure the weight of collected water, the amount of runoff is directly determined with time. To accelerate the runoff hence any possibility of ponding on the soil surface is eliminated, the column test apparatus is inclined 1° towards the direction of runoff collecting tank. At the bottom of column test apparatus, a valve can be

adjusted to control drainage. The outflow is collected by a tank and is weighted by an electronic balance.

Figure 5.2 Soil moisture sensor (EC-5, Decagon Devices Inc, USA).

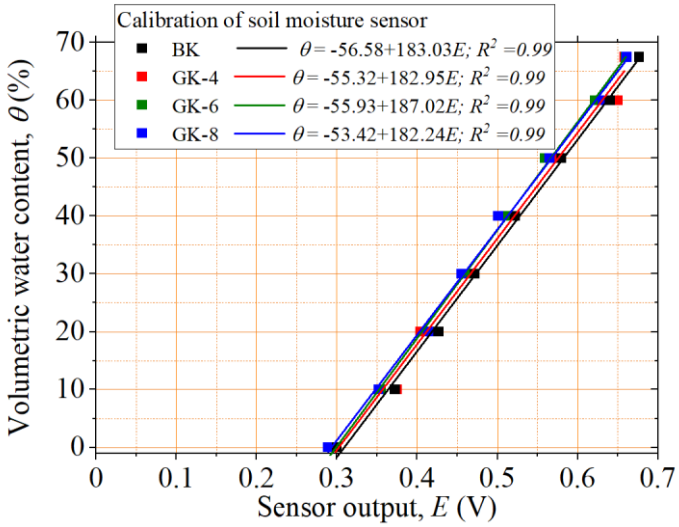

Figure 5.3 Calibration of soil moisture sensors with different grass ages.

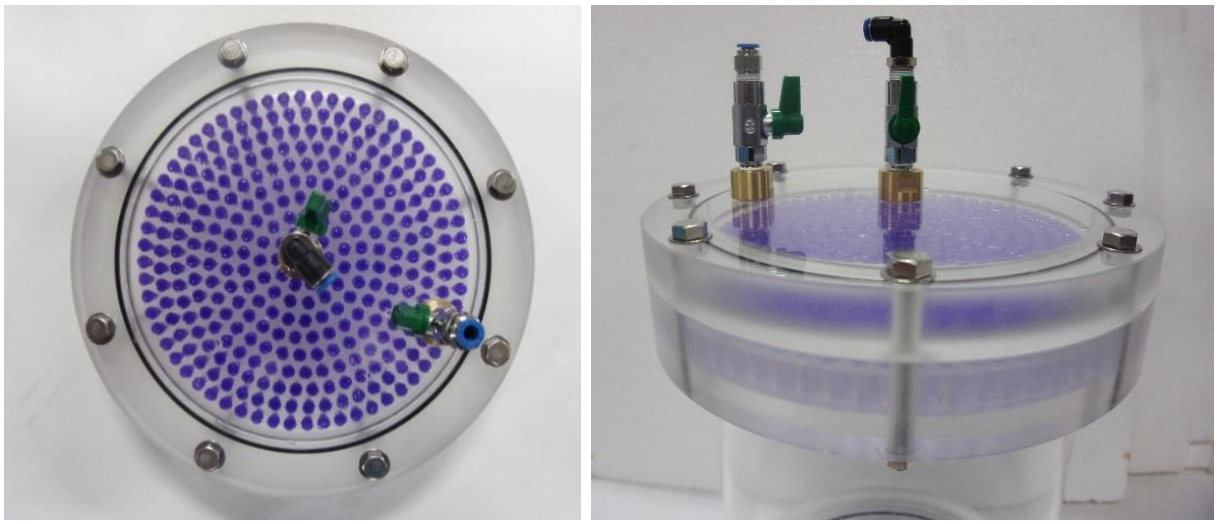

Figure 5.4 Newly developed rainfall simulator.

5.3 Soil specimen preparation

Toyoura sand layer in the column test apparatus was formed by falling the oven-dried sand with air pluviation method for each 25 mm. As a result, Toyoura sand in the column test has the same porosity and dry density presented in Table. 4.1. The soil moisture sensors were buried at the desired elevations before the above layer of Toyoura sand was fallen out. The overlying layer was the bare Komaoka soil or the grassed Komaoka soil with a height of 150 mm. For this layer, Komaoka soil was firstly prepared into steel molds with an internal diameter of 200 mm and a height of 200 mm. These steel molds were pre-cut along vertical direction and fixed with tapes and clamps. The air pluviation method and slight compaction were employed to make Komaoka soil specimen into six layers. The targeted porosity and dry density of soil specimens are similar to those in the permeability test. Subsequently, the mixture of grass seeds was sown on the soil surface to prepare the grassed soil specimens. Bare soil and grassed soil specimens were exposed to the climatic elements for experiencing drying-wetting cycles after putting inside growth room for three weeks. After exposing to climatic elements during 4 months for bare soil and 4, 6, 8 months for grassed soils, the soil specimens were carefully transported into the column test apparatus. Three replicates were used for each grass age to verify and improve the universality of the test results. A thin layer of vacuum grease was pasted along the inner wall of the cylinder to minimize any preferential flow path. Fig. 5.5 presents examples of a grassed soil specimen and grassroots of GK-4. The grassroot length was measured after performing the column test and it was shown that grassroot length was longer than 150 mm for all tests with grassed soils.

(a) (b)

Figure 5.5 Example of (a) grassed soil specimen, and (b) grass roots of GK-4 in column test.

5.4 Experiment procedures

All column tests were carried out in the laboratory room in which constant temperature at around 25 ºC is regulated. Two stages were performed for each column test, namely the wetting stage and drying stage. The wetting stage was to investigate the runoff, outflow, changes in volumetric water content and matric suction under different rainfall intensities. Prior to conduct the wetting stage, all soil in the column test apparatus was wetted by closing the valve at bottom of column test apparatus and applying rainfall with rainfall simulator until soils in column reach a saturated condition. Next, the valve at the bottom of column test apparatus was opened for freely drainage and soils were subsequently exposed to the atmosphere until the volumetric water contents along soil column reached the equilibrium condition (Fig. 5.6). In this Fig., bare soil is named as BK. The tests considering the grassed soil with grass ages of 4, 6, 8 months are denoted as GK-4, GK-6, GK-8, respectively. This procedure was to establish similar initial volumetric water content along the soil column so that the responses of matric suction and volumetric water content were fairly compared.

The wetting stage was carried out by applying the rainfall intensities of 15, 30, 60, 120 mm/h during 5.5, 2, 2, 2 hours, respectively. Rainfall intensities against rainfall duration are illustrated in Fig. 5.7. The rainfall duration at each rainfall intensity was chosen to observe the stable values of volumetric water contents and matric suctions in Komaoka soil and to minimize the influence of any surface erosion due to heavy rainfall events. Before testing, five ceramic cups with diameter of 5 cm were distributed uniformly over the cross-sectional area of the cylinder to collect the amount of rainfall water for 30 minutes. The maximum difference in mass of the collected raindrop water was about 8 %, which was assumed to be acceptable for simulating uniform raindrop distribution (Ng et al., 2014).

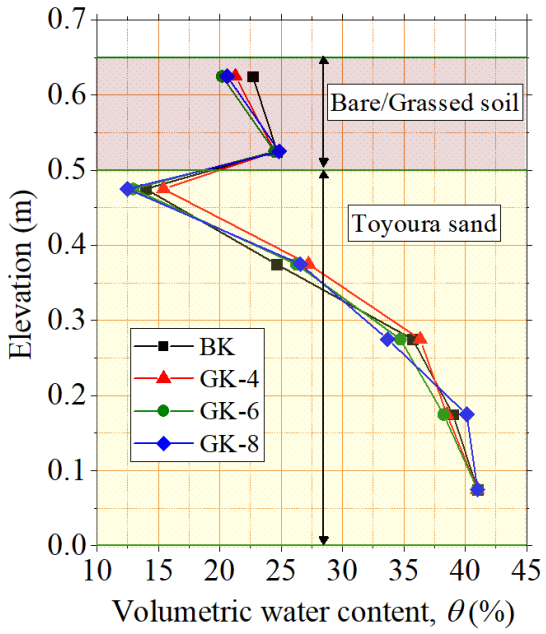

Figure 5.6 Volumetric water content distribution at initial condition of wetting stage.

After finishing the wetting stage, grass shoots were trimmed to prevent any influence of transpiration. The soil in the column was saturated again before carrying out the drying stage. The valve was continuously closed to control the zero-flux boundary condition at the bottom and the surface of Komaoka soil is exposed to the atmosphere for accelerating the evaporation. The drying stage aimed to measure the SWCC and the unsaturated coefficient of permeability of soil. The SWCC was measured by relating the volumetric water content and matric suction, which were shown by soil moisture sensor and tensiometer readings at the same elevation. Besides, the coefficient of permeability of unsaturated soil at center of two tensiometers was computed by the instantaneous profile method.

The instantaneous profile method was originally proposed by Watson, 1966. This method was evaluated and widely used in both laboratory and field because of its simplicity and practicality (Hillel et al., 1972; Meerdink et al., 1996; McCartney, 2007; Ng and Leung, 2011; Ng and Leung, 2012). Leung et al. (2016) reported that the spacing of 100 mm between two sensors is close enough for accurately computing the unsaturated coefficient of permeability.

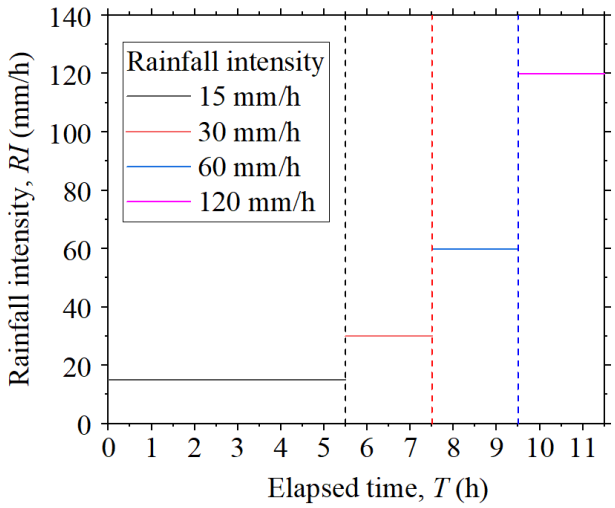

Figure 5.7 Variations of rainfall intensities against time.

The calculation procedure for the instantaneous profile method used in this study is summarized as follows. The water flow rate ($v_{zH,tave}$) at depth z_H for particular average elapsed time (t_{ave} = (t_{i+1}+t_i)/2) is computed:

$$\upsilon_{z_H,t_{ave}} = \frac{\left(\int_{z_A}^{z_H} \theta_{z_H}^{t_{i+1}} dz - \int_{z_A}^{z_H} \theta_{z_H}^{t_i} dz\right)}{t_{i+1} - t_i} + v_{z_A,tave} \tag{5.1}$$

where θ_{zH}^{ti}, θ_{zH}^{ti+1} were volumetric water content profile as a function of depth z_H at a specific elapsed time t_i and t_{i+1}, respectively; $v_{zA,tave}$ was boundary water flow rate evaluated at average elapsed time (t_{ave}) at the bottom of soil column (i.e. z_A = 0 m); The boundary was taken at elevation 0 m. This boundary condition

was controlled as zero flux plane hence $v_{ze,tave} = 0$.

In addition, the hydraulic gradient ($i_{zH,tave}$) at depth z_H at particular average elapsed time (t_{ave}) is determined by the slope of hydraulic head profile at that depth:

$$i_{zH,tave} = \frac{1}{2}\left[\frac{\left(H_{z_K,ti} - H_{z_G,ti}\right)}{\left(z_K - z_G\right)} + \frac{\left(H_{z_K,t_{i+1}} - H_{z_G,t_{i+1}}\right)}{\left(z_K - z_G\right)}\right] \tag{5.2}$$

where H was hydraulic head, which was a summation of pore-water pressure (h_p) and elevation head (z); $H_{zK,\,ti}$, $H_{zK,\,ti+1}$, were the hydraulic head at depth z_{j+1} at specific elapsed time t_i and t_{i+1}, respectively; $H_{zG,ti}$, $H_{zG,ti+1}$ were the hydraulic head at depth z_G at specific elapsed time t_i and t_{i+1}, respectively.

The unsaturated coefficient of permeability at point z_H at average elapsed time (t_{ave}) is computed by dividing the water flow rate ($v_{zH,tave}$) by the average hydraulic gradient ($i_{zH,tave}$):

$$k_{z_H,t_{ave}} = \frac{v_{zH,tave}}{i_{zH,tave}} \tag{5.3}$$

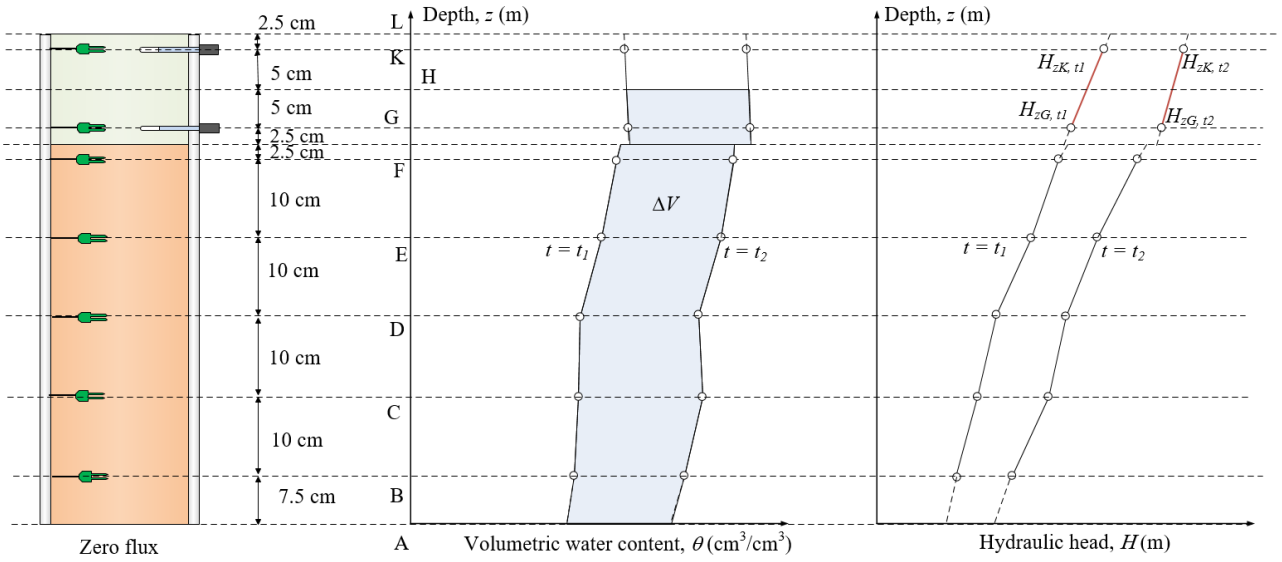

Figure 5.8 Arbitrary instantaneous profile of VWC (θ) and hydraulic head (H) at elapsed time $t = t_1$ and $t = t_2$, along one-dimentional soil column.

5.5 Results and discussions

5.5.1 Soil-water characteristic curve

The drying SWCCs of both bare soil and grassed soils at elevations 525 mm and 625 mm are presented in Fig. 5.9. Grassed soil has a higher matric suction than bare soil for given volumetric water content. The enhanced water retention capacity of grassed soil is similar to the findings of Leung et al. (2015a). A reason for this phenomenon is that the soil pores are occupied by grass roots. As a result, the diameters of soil pores are reduced hence matric suction is increased due to the capillary law (Scanlan and Hinz, 2010).

Another reason might be attributed to the exudates released by grass roots (Grayston et al., 1997; Bengough, 2012). These substances might have effect on the contact angle of water menisci and soil hydrophobicity (Carminati et al, 2016). This leads to the influences on SWCCs and permeability.

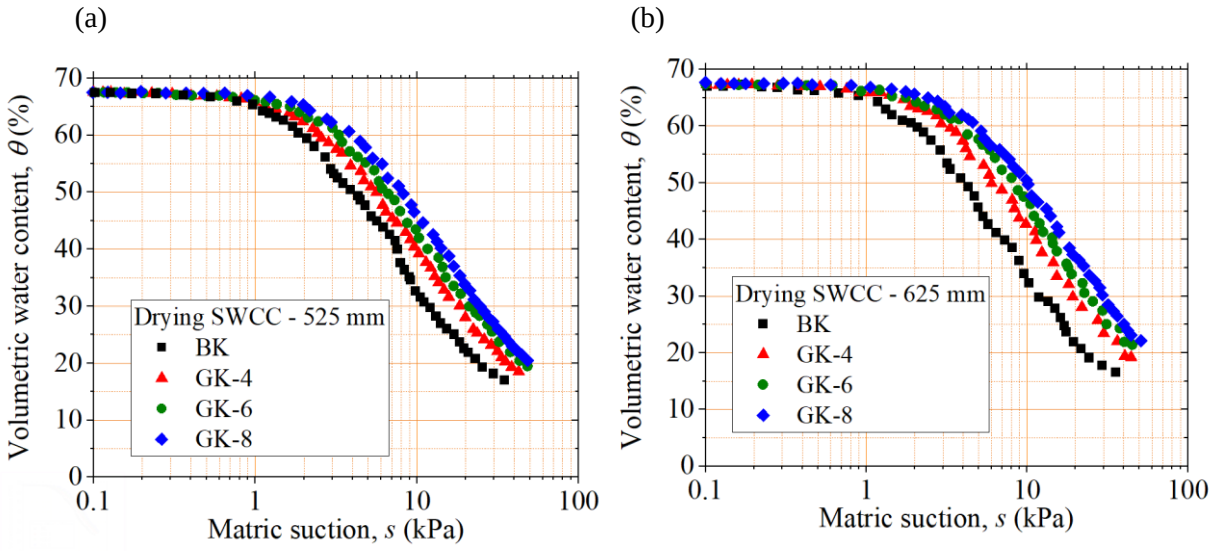

Figure 5.9 Soil-water characteristic curves of grassed soils and bare soil at elevations (a) 525 mm and (b) 625 mm.

Table 5.1 summarizes the root contents including root biomass per soil volume (ρ_R) and root volume ratio (R_v) of grassed soils in column tests. R_v is defined as a ratio of the total volume of grass roots to the total volume of soil. As the root biomass and root volume rise corresponding to the increase in grass age, more soil pores are occupied by grass roots hence the matric suction is further enhanced. In addition, it can be seen clearly from Fig. 11 that matric suctions at elevation 625 mm are slightly higher than that at elevation 525 mm at the same volumetric water content regardless of grass age. The reasons might be attributed to the distribution of R_v. According to Ni et al. (2018b), R_v of grassed soil is reduced along depth. As a result, the matric suction is increased at which the R_v is higher.

Fig. 5.10 shows the correlation of air-entry value (AEV) with the R_v. AEVs of grassed soils at different grass ages are computed by fitting SWCCs employing Van Genuchten (1980) model, which will be explained later. The results of AEVs are presented in Table. 6.1. It can be seen that there is a linear relationship between AEVs and R_v. The higher values of R_v results in the greater AEV. AEV approximately doubles (from 1.58 kPa to 3.64 kPa) when R_v rises from 0 m^3/m^3 (BK) to 7.7E-3 m^3/m^3 (GK-8). This also indicates that the presence of grass roots in soil pores leads to an increase in water retention capacity as mentioned above. The linear empirical relationship is derived (Eq. 5.4) and is plotted in Fig. 5.11 along with the achieved high R^2 value.

$$AEV = 265.983R_v + 1.438 \quad (5.4)$$

5.5.2 Unsaturated coefficient of permeability

The unsaturated coefficients of permeability of grassed soils and bare soil are indicated in Fig. 5.12. The grassed soils have a lower unsaturated coefficient of permeability than that of bare soil regardless of grass age. A similar reduction of unsaturated coefficient of permeability due to the presence of vegetation roots are also found in the studies reported by Rahardjo et al. (2014) and Pagano at al. (2019). In addition, the unsaturated coefficient of permeability of grassed soil is reduced with the increase in grass age. The difference in unsaturated coefficient of permeability is smaller at high matric suction. The possible reason is that the grass roots tend to block large soil pores hence the unsaturated coefficient of permeability at high matric suctions are less influenced.

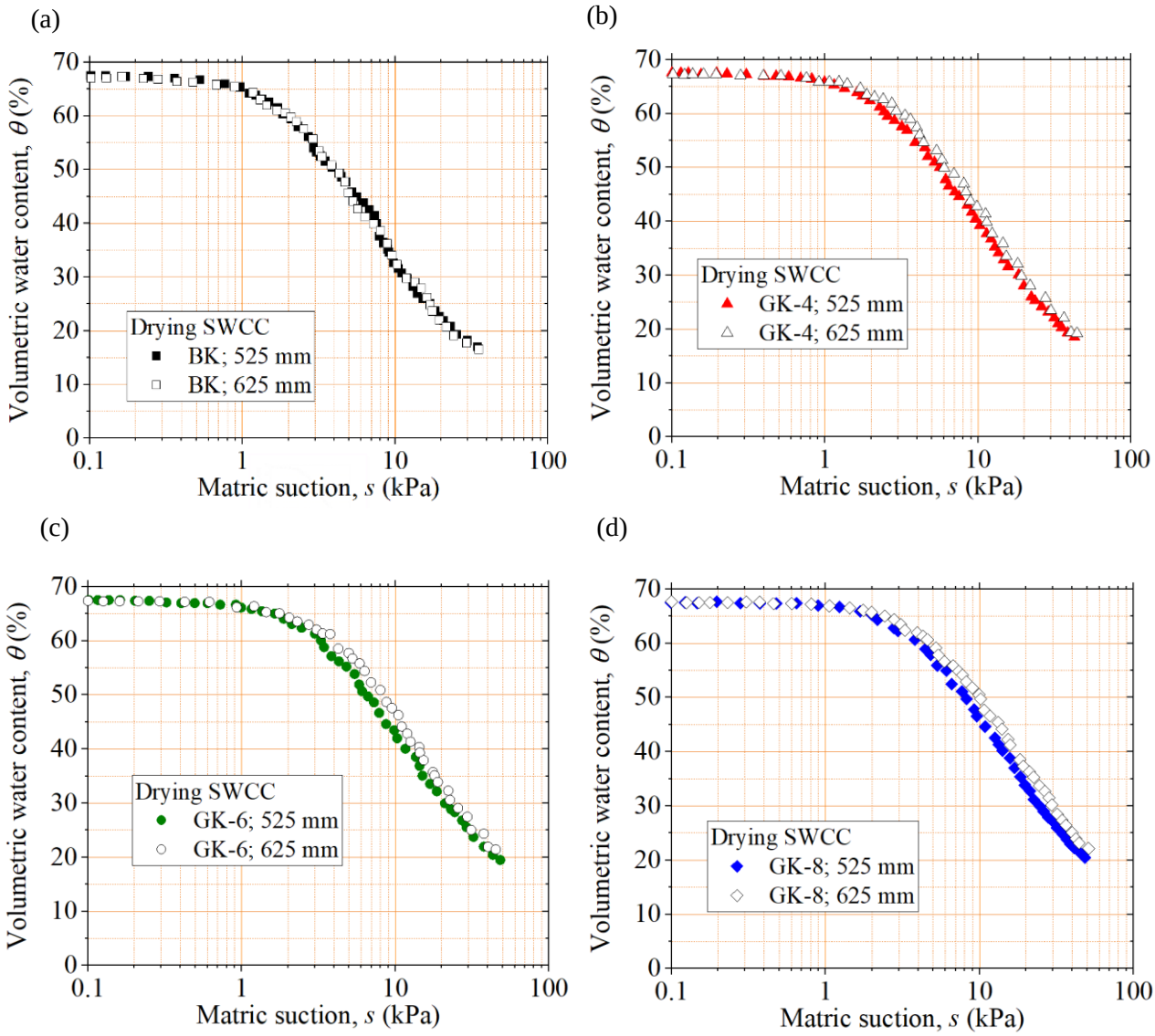

Figure 5.10 Comparisons of soil-water characteristic curves at elevations 525 mm and 625 mm of (a) BK, (b) GK-4, . (c) GK-6, (d) GK-8.

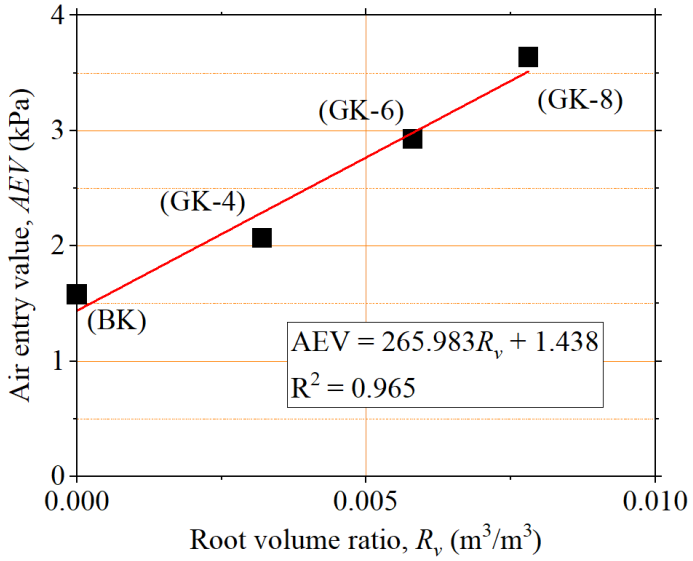

Figure 5.11 Relationship between the air-entry value and root volume ratio.

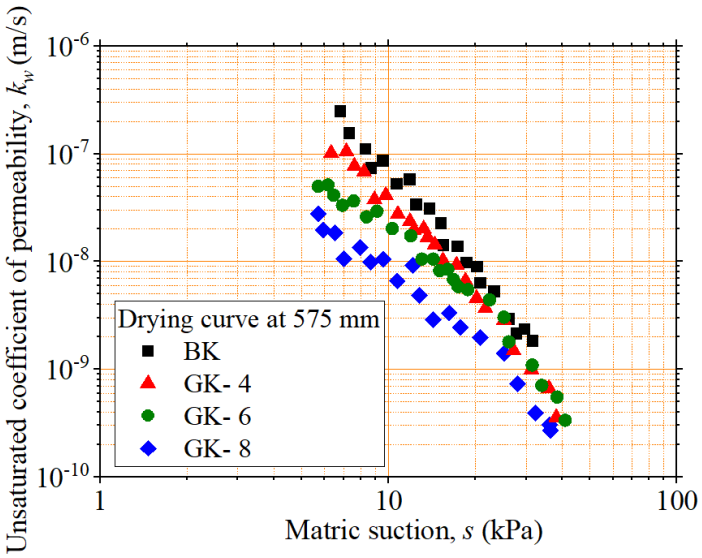

Figure 5.12 Unsaturated coefficient of permeability of bare soil and grassed soils.

Table 5.1 Descriptions of column tests and root contents.

Test No.	Age of plant (months)	Root biomass per soil volume, ρ_R (kg/m^3)	Root volume ratio, R_v (m^3/m^3)
BK	--	--	--
GK – 4	4	1.25	3.2E-3
GK – 6	6	2.36	5.8E-3
GK – 8	8	3.15	7.7E-3

5.5.3 Outflow and runoff

Fig. 5.13 presents the comparison in the cumulative volume of runoff and outflow in column tests. The duration of rainfall in this Fig. is calculated by taking a starting time of simulated rainfall as a reference point. The outflow occurs earliest in bare soil (BK) and starts latest for grassed soil with grass age of 8 months (GK-8). In fact, outflow is occurred at 13770, 17480, 18760, and 22130 seconds after staring rainfall for BK, GK-4, GK-6, GK8, respectively. In addition, the cumulative volume of outflow is much lower in grassed soil with higher grass age. The cumulative volumes of outflow are 10980, 8572, 7333, 6528 cm^3 for BK, GK-4, GK-6, GK8, respectively. These numbers are accounted for 70, 54, 46, and 41 % total cumulative volume of rainfall water. The reason is attributed to the lower values in both saturated and unsaturated coefficient of permeability of grassed soil with higher age.

On the other hand, the runoff occurs in grassed soil regardless of grass age, whereas there is no runoff in bare soil. The surface runoff is commenced at 34430, 30160, 27500 s for GK-4, GK-6, GK-8, respectively. In another word, runoff starts during 120 mm/h rainfall intensity for GK-4, and during 60 mm/h rainfall intensity for GK-6 and GK-8. Moreover, the grassed soil with the higher grass age has much significantly higher amount of runoff. At the end of the experiment, the amount of cumulative volume of runoff in GK-4, GK-6, GK-8 accounts for 14, 20, and 26 % of total rainfall water, respectively.

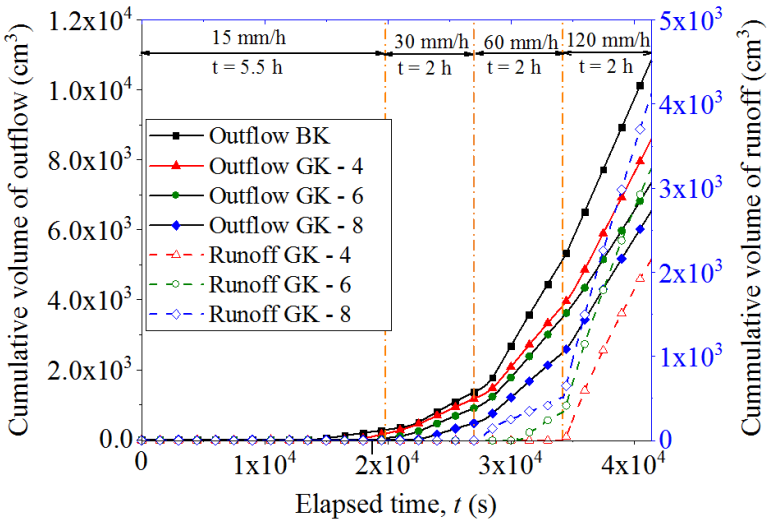

Figure 5.13. Comparisons of cumulative volume of outflow and runoff in grassed soils and bare soil.

5.5.4 Variations in volumetric water content and matric suction

Fig. 5.14 depicts the changes in matric suction and volumetric water content at elevation 525 mm and 625 mm in the column test apparatus, respectively. It can be seen that the grassed soil with lower age has lower matric suction than that of higher age before the commencement of rainfall even though the initial volumetric water contents are relatively similar. This is because the later has a higher capability to retain

matric suction for the same water content than that of the former as have mentioned previously. The matric suction of grassed soil with higher grass age reduces later than that of lower age under rainfall. However, it is interesting that the decreasing rate of matric suction is slightly shaper in the grassed soil with higher grass age than that with lower grass age.

The reason is that the grassed soil with higher grass age has higher initial matric suction, which leads to the higher hydraulic gradient when the wetting front approaches. The matric suction of both bare soil and grassed soils decreases and remains constant at somewhere in the vicinity of 2 kPa despite the fact that different rainfall intensities are applied.

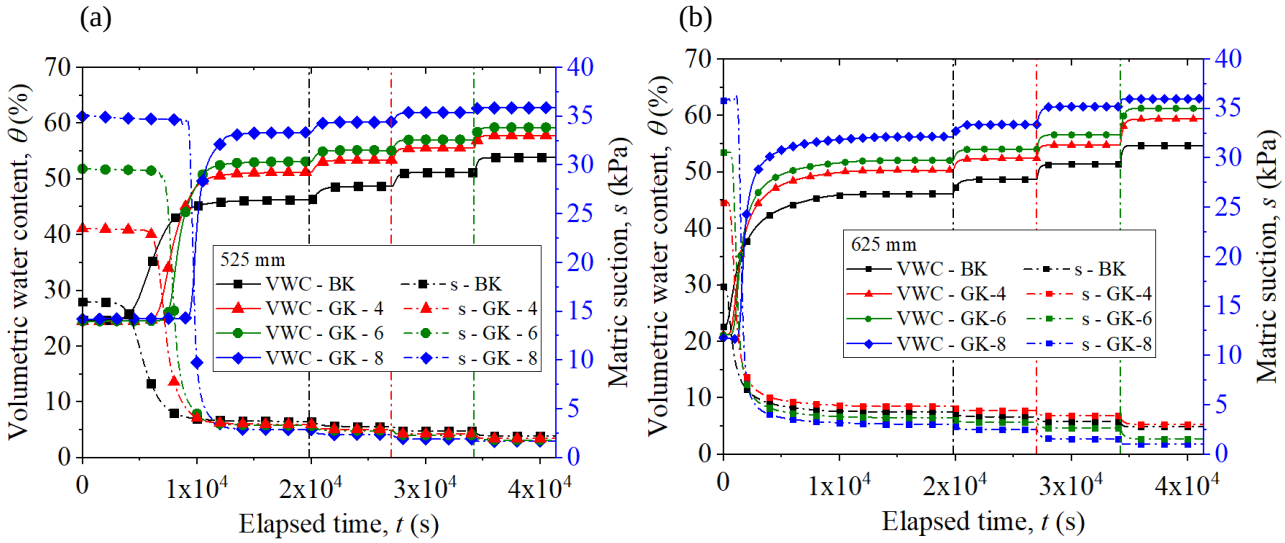

Figure 5.14 Comparisons of VWC and matric suction at elevation (a) 525 mm, and (b) 625 mm of bare soil and grassed soils under rainfall.

Of all column tests, volumetric water content increases earliest in bare soil because grassed soil has a smaller coefficient of permeability. Furthermore, at several minutes after the commencement of rainfall, it was observed that the grass leaves intercepted and retained rainwater. This might also contribute to the delayed response of both volumetric water content and matric suction in grassed soil as compared to bare soil. This phenomenon is also observed by Ng and Zhan (2007) and Ng et al. (2016b). The storage capacity of grass leaves varies from 1 mm to 5 mm of rainfall as reported by Branson et al. (1972). Moreover, the volumetric water content rises earlier for the grassed soil with lower grass age. The volumetric water content in grassed soils rises sharply while the volumetric water content in bare soil increases gradually. It is corresponding to the response of matric suction to rainfall as have mentioned above. Moreover, higher volumetric water contents are recorded for the grassed soils with higher grass age compared to that with lower grass age during intense rainfall intensities although the matric suctions of these soils are similar (2 kPa). The volumetric water contents during rainfall intensity of 120 mm/h were 0.55, 0.57, 0.59, 0.63 for

BK, GK-4, GK-6, GK-8, respectively. The reason is that the grassed soils with higher age retain higher volumetric water content as presented in SWCCs.

5.6 Summary

This chapter studied the influences of grass age on unsaturated hydraulic properties (i.e. SWCC and unsaturated coefficient of permeability) and seepage behaviors (i.e. outflow, runoff, and the variations in volumetric water content/matric suction) of unsaturated Komaoka volcanic soil by performing column tests. Two stages were performed for each column test, namely: wetting stage and drying stage. The wetting stage was to investigate the runoff, outflow, changes in volumetric water content and matric suction under different rainfall intensities. The newly developed rainfall simulator, which produced a uniformly distributed raindrop, was used to create different rainfall events. The drying stage aimed to determine the SWCCs and the unsaturated coefficients of permeability of grassed soils. The unsaturated coefficient of permeability of grassed soil was computed by the instantaneous profile (IP) method.

The experimental results indicated that grassed soil had a higher matric suction than bare soil for given volumetric water content. A reason for this phenomenon was that the soil pores are occupied by grass roots. Another reason might be attributed to the exudates released by grass roots. The increase in grass age also resulted in a capacity to retain higher matric suction and higher AEV of grassed soil.

The grassed soils have a lower unsaturated coefficient of permeability than that of bare soil regardless of grass age. Furthermore, unsaturated coefficient of permeability of grassed soil was reduced with a rise in grass age. The difference in the unsaturated coefficient of permeability was smaller at high matric suction. The plausible reason was that the grass roots tend to block large soil pores. As a result, the unsaturated coefficient of permeability at high matric suctions were less influenced.

The cumulative volume of outflow was much lower in grassed soil with higher grass age. In contrast, the runoff occured in grassed soil regardless of grass age, whereas there was no runoff in bare soil. The matric suction of both bare soil and grassed soils decreased and remained constant at somewhere in the vicinity of 2 kPa despite the fact that different rainfall intensities were applied.

6 ESTIMATION MODEL FOR UNSATURATED HYDRAULIC PROPERTIES OF GRASSED SOIL

6.1 Validation of the existing models

Many models are employed to estimate the unsaturated coefficient of permeability based on SWCC and saturated coefficient of permeability. In general, the measured SWCCs of bare and grassed soils are firstly fitted. After that, the unsaturated coefficients of permeability are estimated based on the saturated coefficient of permeability and above-fitted SWCCs. Of all the existing models, Van Genuchten (1980), Fredlund and Xing (1994), and Fredlund et al (1994) models are widely used. The SWCC and unsaturated coefficient of permeability of bare soil are estimated by Van Genuchten (1980) models as shown in Eqs. 6.1 and 6.2.

$$S_r = \left[1+(as)^n\right]^{-m} \tag{6.1}$$

where S_r is the degree of saturation of soil; a (1/kPa) is a material parameter which is primarily a function of the air entry value of the soil; n and m are material parameters (m = 1-1/n); and s (kPa) is the matric suction.

$$\frac{k(s)}{k_s} = \left[\frac{\left\{1-(as)^{nm}\left[1+(as)^n\right]^{-m}\right\}^2}{\left[1+(as)^n\right]^{m/2}}\right] \tag{6.2}$$

where $k(s)$ (m/s) is the unsaturated coefficient of permeability of soil; k_s (m/s) is saturated coefficient of permeability.

Fredlund and Xing (1994) and Fredlund et al. (1994) equations are shown in Eqs. 6.3 and 6.4.

$$\theta_w = \theta_s\left[1-\frac{\ln\left(1+\frac{s}{h_r}\right)}{\ln\left(1+\frac{s}{h_r}\right)}\right]\left[\frac{1}{\left[\ln\left[\exp(1)+\left(\frac{s}{a_f}\right)^{n_f}\right]\right]^{m_f}}\right] \tag{6.3}$$

where, θ_w (cm^3/cm^3) is volumetric water content at any matric suction; θ_s (cm^3/cm^3) is saturated volumetric water content; a_f (kPa) is material parameter which is primarily a function of the air-entry value of the soil; n_f is material parameter which is primarily a function of rate of water extraction from the soil once the air-entry value has been exceeded; m_f is primarily a function of the residual water content; h_r (kPa) is matric suction at residual water content; and s (kPa) is any matric suction value.

$$k_r(s) = \frac{\int_{\ln(s)}^{b} \frac{\theta(e^y) - \theta(s)}{e^y} \theta'(y)\,dy}{\int_{\ln(s_{aev})}^{b} \frac{\theta(e^y) - \theta_s}{e^y} \theta'(e^y)\,dy} \tag{6.4}$$

where, $k_r(s)$ (m/s) is relative coefficient of permeability at matric suction s; s_{ave} (kPa) is air-entry value of the soil; b is equal to ln(1000000); y is dummy variable of integration representing matric suction; θ' is derivative of Eq. 6.3.

It can be seen from Fig. 6.1 that the fitting results by Van Genuchten (1980) model and Fredlund and Xing (1994) model present a good agreement with the SWCCs of both bare soil and grassed soil obtained from column tests. The parameters used for fitting SWCCs and fitting errors are summarized in Table 6.1.

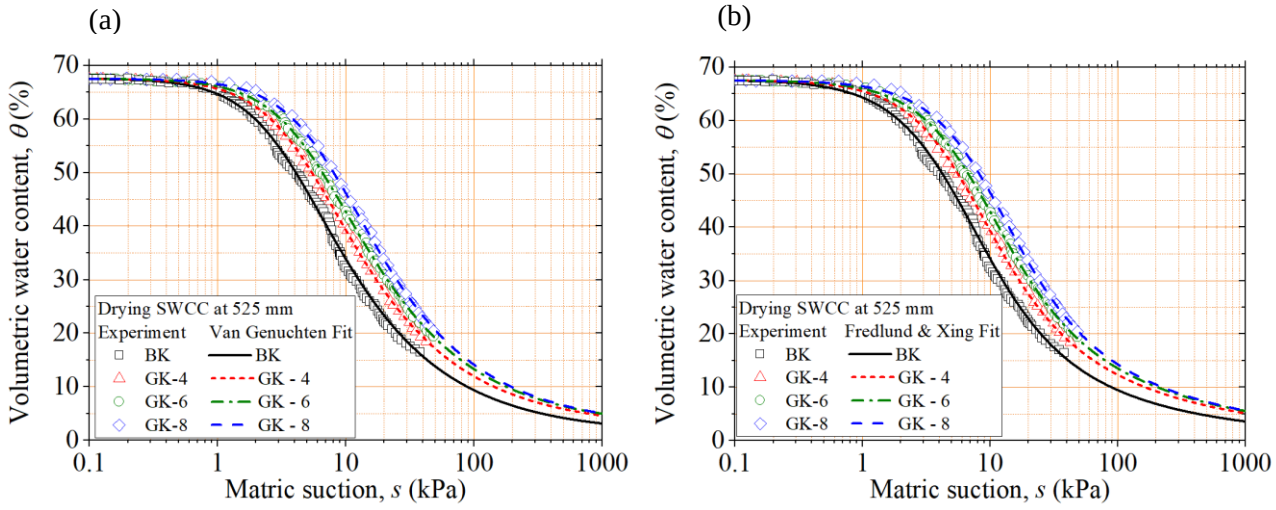

Figure 6.1 Comparisons of measured and fitted SWCCs by (a) Van Genuchten (1980) model, and (b) Fredlund and Xing (1994a) model of bare soil and grassed soils.

In order to estimate unsaturated coefficients of permeability, saturated coefficients of permeability of grassed soils in column tests are determined by interpolation based on Fig. 6.2b. The interpolated results of saturated coefficients of permeability of grassed soils are also presented in Fig. 6.2 and Table 6.2. Fig.6.2a reveals that the saturated coefficients of permeability of grassed soils in column test are higher than that in permeability test for grassed soil at the same grass age. A plausible reason is due to the size effect of soil specimen. Since the volume of soil specimen in permeability test is significantly smaller than that in column test (942 cm^2 compared to 4710 cm^2, respectively), grass roots in the permeability test is more concentrated than the column test. As a result, the root volume ratio in the permeability test is higher than that in the column test (Fig. 6.2b). It should be noted that the relationships between saturated coefficient of permeability of grassed soils and root volume ratio obtained from column tests agree well with that from permeability tests under the same grass age. This indicates that the size effect of soil specimens is hardly recognized in the $R_v - k_s$ relations.

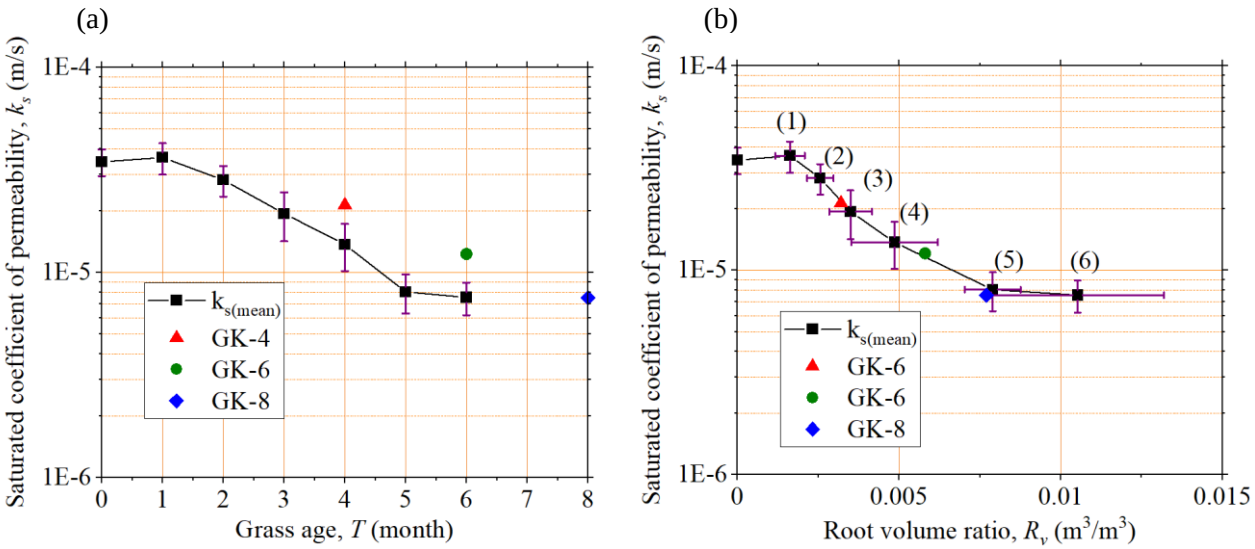

Figure 6.2 Relationship between the saturated coefficient of permeability of grassed soils (a) versus grass age, and (b) versus root volume ratio.

Table 6.1 Parameters used for fitting SWCCs.

Test No.	Fitting parameters				
	Fredlund and Xing (1994)				
	a_f	n_f	m_f	h_r	Fitting error
BK	4.43	1.49	1.15	33.41	0.9988
GK-4	5.67	1.49	1.08	49.89	0.9988
GK-6	6.79	1.48	1.07	60.47	0.9988
GK-8	8.39	1.52	1.09	70.79	0.9989
	Van Genuchten (1980)				
	a	n	m	AEV	Fitting error
BK	0.28	1.63	0.39	1.58	0.9980
GK-4	0.21	1.63	0.39	2.07	0.9944
GK-6	0.18	1.58	0.37	2.93	0.9985
GK-8	0.14	1.63	0.39	3.64	0.9961

However, the estimations of unsaturated coefficients of permeability are far different from experimental results as shown in Fig. 6.3. The unsaturated coefficients of permeability of grassed soils estimated by both two above-mentioned models are significantly higher as compared to that from experimental results. In addition, the estimated results show that the grassed soils have higher unsaturated coefficient of permeability than bare soil at matric suction greater than around 5 kPa.

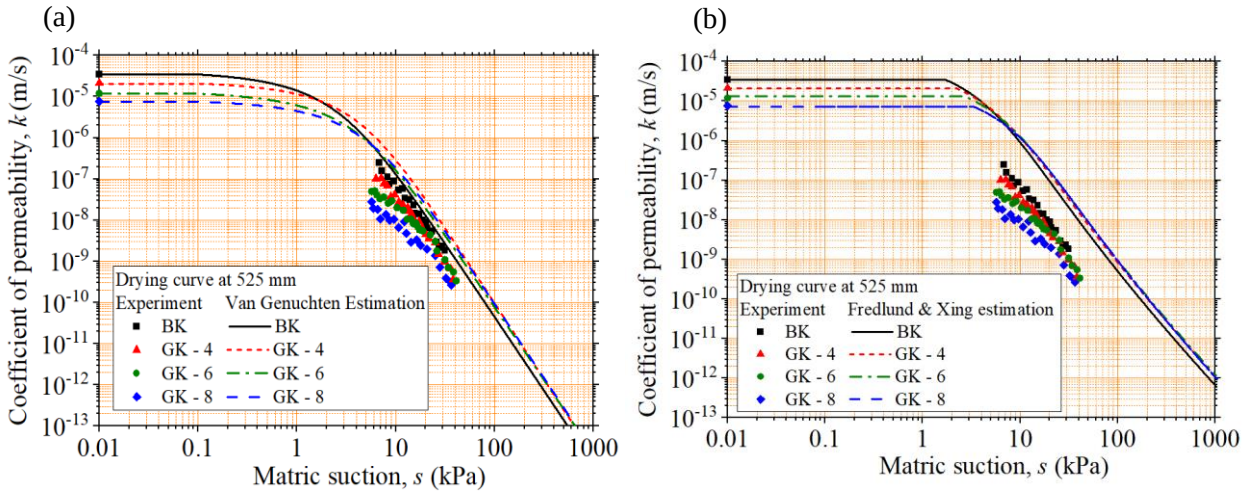

Figure 6.3 Comparisons of measured and estimated unsaturated coefficient of permeability of grassed soils and bare soil by (a) Van Genuchtan (1980) model, and (b) Fredlund et al (1994) model.

6.2 Proposal of new estimation model

Quantifying the root-induced modification in soil hydraulic properties, including SWCC and unsaturated coefficient of permeability, is vital to assess the instability of vegetated soil slope subjected to rainfall. Therefore, in order to minimize the drawback of the above-mentioned models, this chapter proposes a new model for estimating the unsaturated coefficient of permeability of grassed soils. In past research, Ng et al. (2016a) proposed a new water retention model for root-permeated soil. This model considered that plant roots occupy soil pore space and reduce soil pore size. The void ratio of vegetated soil is conculcated as the following equation.

$$e' = \frac{e_0 - R_v(1+e_0)}{1+R_v(1+e_0)} \tag{6.5}$$

where e_0 and e' (dimensionless) are void ratio of bare soil and vegetated soil, respectively; R_v (m^3/m^3) is the root volume ratio.

In order to calculate the SWCC of vegetated soil, Ng et al. (2016a) employed the void-ratio-dependent SWCC (Eq.6.5) proposed by Gallipoli et al. (2003) with substituting Eq. 6.5 into Eq. 6.6.

$$S_r = \left[1 + \left(\frac{se'^{m_4}}{m_3}\right)^{m_2}\right]^{-m_1} \tag{6.6}$$

where m_1 (dimensionless), m_2 (dimensionless), m_3 (kPa), m_4 (dimensionless) are the model parameters. m_1 and m_2 control the shape of the SWCC, while m_3 and m_4 are related to the air-entry value (AEV). Considering that the void ratio has neglectable effects on SWCC at high matric suction range, the product $m_1 m_2 m_4$ can be set to 1 (Gallipoli, 2012).

Furthermore, Ni et al. (2019c) proposed the SWCC model to capture the reduction of AEV due to the formation of soil macropores upon root decay.

$$S_r = \left[1 + \left(\frac{se'^{m_4}}{m_3 \exp(-\kappa \frac{e_r}{e_{r0}})}\right)^{m_2}\right]^{-m_1} \tag{6.7}$$

where κ is the model parameter that controls the rate of reduction of the AEV due to root decay and this parameter is dependent on the plant type and soil type, e_r is the macro void returned from root decay, and e_{r0} is the void ratio occupied by roots.

With the above-mentioned past researches in mind, this study proposes a new water retention model and a new unsaturated hydraulic conductivity model, provided that any effects of root decay and the formation of macropores are neglected, and that the changes in soil microstructure due to wetting-drying cycles are not considered. As a result, in order to consider the effects of active grass roots on the enhancement of water retention ability of soil, Eq.6.6 is modified by adding the exponential term as following.

$$S_r = \left[1 + \left(\frac{se'^{m_4}}{m_3 \exp(\kappa' R_v)}\right)^{m_2}\right]^{-m_1} \tag{6.8}$$

where κ' is a model parameter that controls the rate of the increase in AEV. This model parameter is dependent on the plant type and soil type. The empirical product $\exp(\kappa' R_v)$ might stand for the effects of reduction in void ratio and root exudates. It is noted that when $R_v = 0$, the Eq. 6.8 resembles to Eq. 6.6.

On the other hand, to account for the reduction in void ratio, and the increase in viscosity as well as additional friction between exudates and water, which lead to the decrease in the coefficient of permeability, Eq. 6.2 is empirically modified as follows.

$$\frac{k(s)}{k_s} = \left[\frac{\left\{1-\left(a\exp(\kappa' R_v)s\right)^{nm}\left[1+\left(a\exp(\kappa' R_v)s\right)^{n}\right]^{-m}\right\}^2}{\left[1+\left(a\exp(\kappa' R_v)s\right)^{n}\right]^{m/2}}\right] \tag{6.9}$$

It is also noted that the Eq. 6.9 resembles to Eq. 6.2 when there is no effect of grass roots ($R_v = 0$).

In order to validate the proposed model, the estimated unsaturated coefficients of permeability of grassed soils are compared with the experimental results from the column tests. The process of estimation for unsaturated coefficient of permeability of grassed soil is summarized in Fig. 6.4 and explained as follows. Firstly, the SWCC of bare soil is separately fitted by Eq. 6.6 to derive the parameters m_1, m_2, m_3, and m_4 (Table 6.3), while SWCCs of grassed soils are fitted by Eq. 6.1 to derive the parameters *a, n, m* (Fig. 6.2a). Next, parameters κ' in Eq. 6.8 is calibrated by the SWCCs of grassed soils as shown in Fig. 6.5. In this study, κ' is equal to 90. After that, saturated coefficients of permeability of grassed soils in column tests are determined by interpolation as have mentioned previously. Finally, the unsaturated coefficients of permeability of grassed soils with different grass ages are estimated by Eq. 6.9. It can be clearly seen that the new model proposed in this study captures well the reduction in unsaturated coefficient of permeability of grassed soils due to the increase in the root volume ratio (Fig. 6.6).

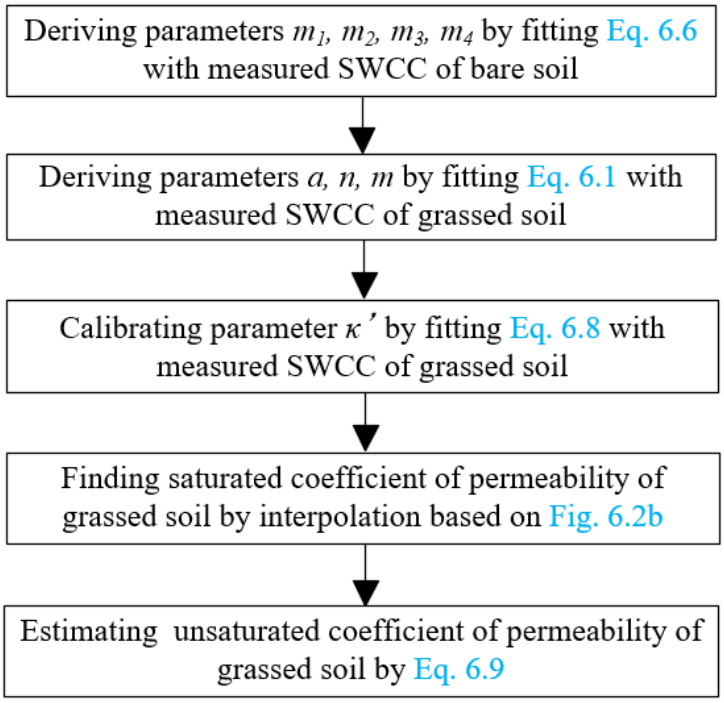

Figure 6.4 Process of estimating coefficient of permeability of grassed soil.

Table 6.2 Parameters used for fitting SWCCs by Eq. 6.6.

Test No.	Fitting parameters			
	m_1	m_2	m_3	m_4
BK	0.355	1.672	11.787	1.686

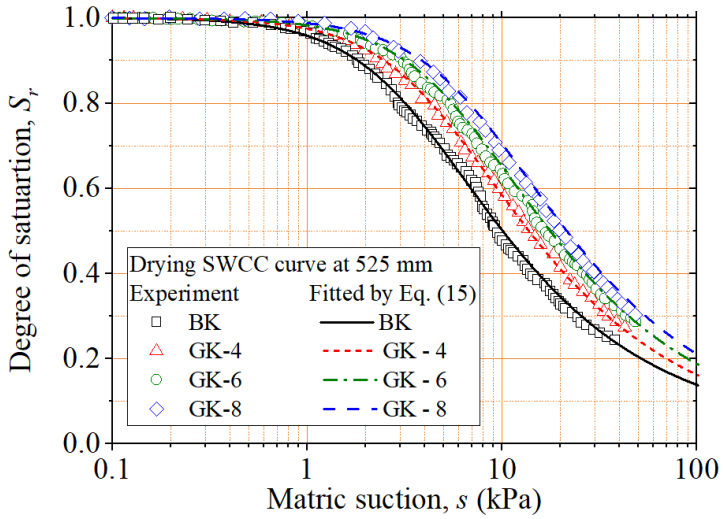

Figure 6.5 Comparisons of measured and fitted SWCCs at elevation 525 mm.

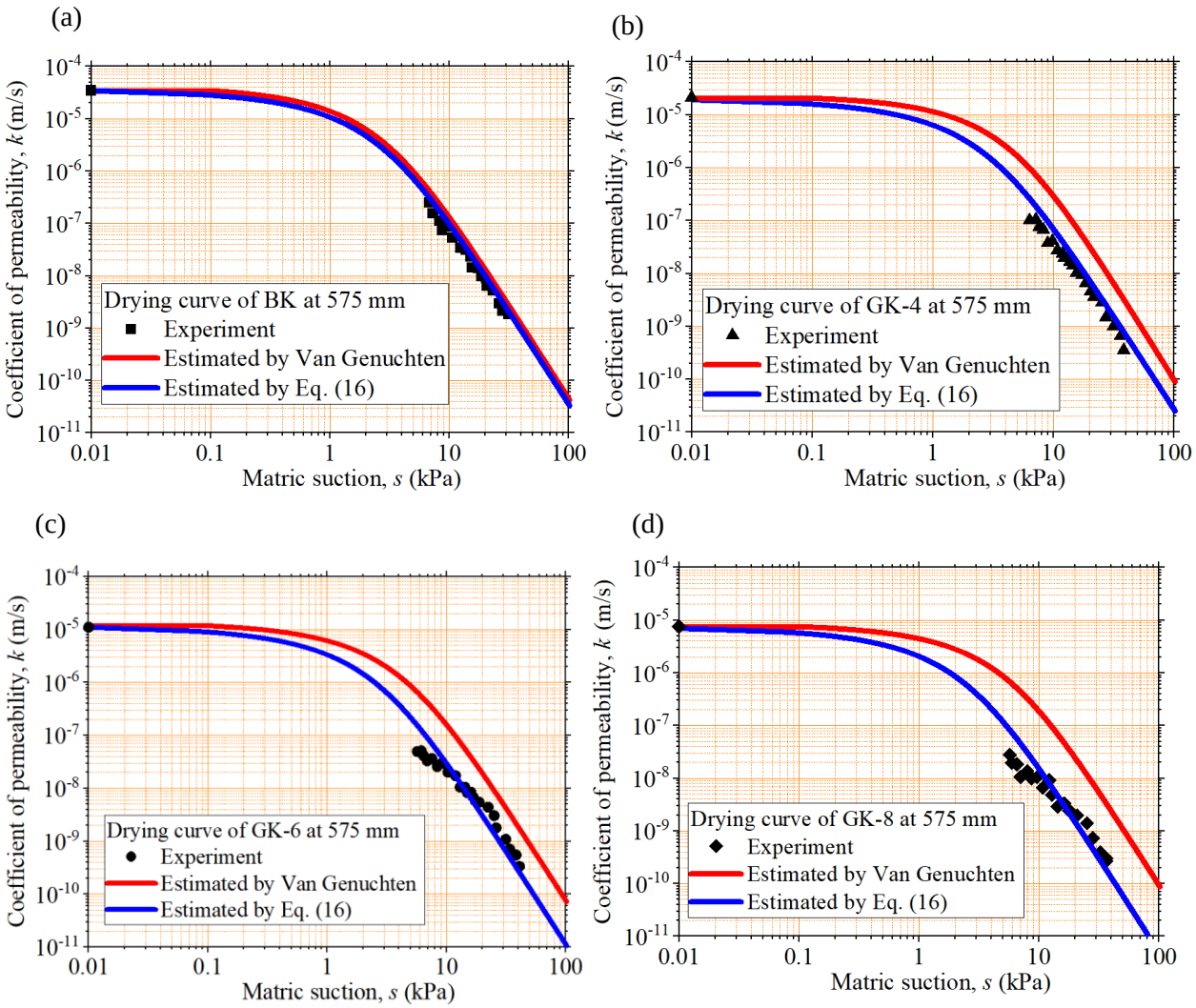

Figure 6.6 Comparisons of measured and estimated unsaturated coefficient of permeability by Van Genuchtan (1980) model and Eq. 16 of (a) BK, (b) GK-4, (c) GK-6, (d) GK-8.

In order to take into account the effect of any difference in grass properties (i.e root volume ratio, R_v) on test results, the SWCCs and unsaturated coefficients of permeability of three replicates of GK-8 are shown in Fig. 6.7. The letter R in Fig. 6.7 denotes the replicate, and it is followed by the number of the test (i.e. R-1). Though SWCCs of three replicates are slightly distinct, those can be fitted by one fitting curve by Van Genuchten (1980) equation as shown in Fig. 6.7a. The saturated coefficients of permeability for three replicates with the average value are illustrated in Table 6.4. It can be seen clearly that the estimated results of unsaturated coefficient of permeability, which is calculated by Eq. 6.9 using the SWCC in Fig.6.7a and the average saturated coefficients of permeability in Table 6.4, agree well with experimental results for three replicates.

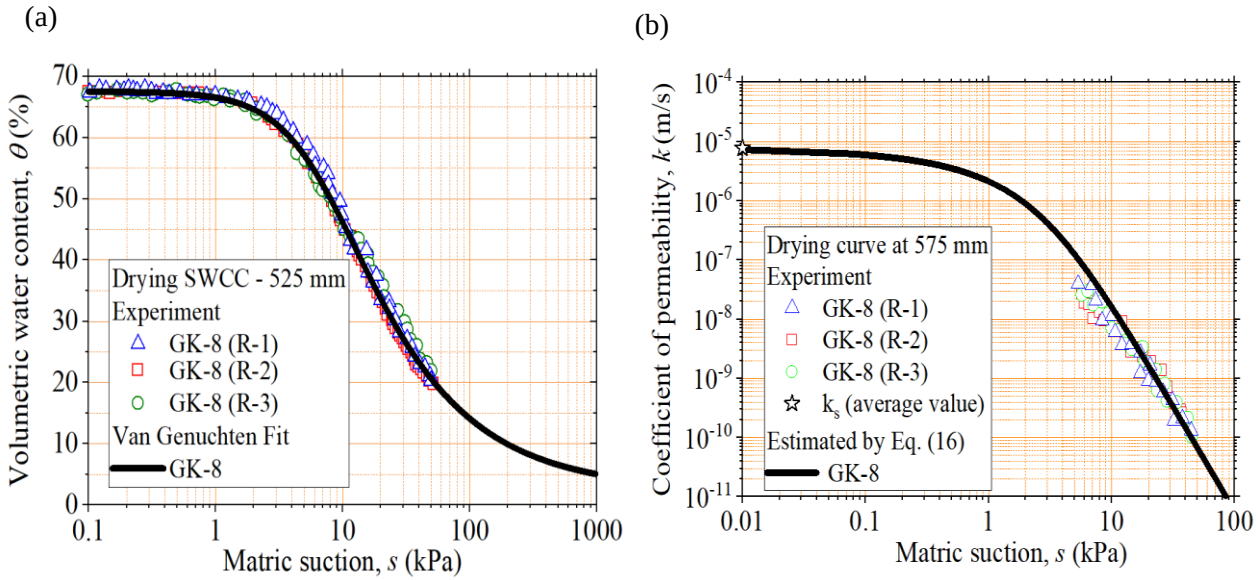

Figure 6.7 Comparisons of measured and estimated (a) SWCCs, (b) coefficients of permeability for three replicates of GK-8.

Table 6.3 Root volume ratio and saturated coefficient of permeability of three replicates of GK-8.

Test No.	Root volume ratio, R_v (m^3/m^3)	Saturated coefficient of permeability, k_s (m/s)
R-1	7.4E-3	9.10E-6
R-2	7.7E-3	7.54E-6
R-3	8.2E-3	5.12E-6
Average value	7.76E-3	7.25E-6

The above findings indicated that the seepage behaviors of grassed soil are affected by grass age. The different grass ages result in the differences in SWCCs, both saturated and unsaturated coefficient of permeability. When the effects of decayed roots are neglected, the grassed soil slope is further stabilized with the increase in grass age. The proposed model is useful to simply estimate the unsaturated coefficient

of permeability of grassed soil at different grass ages. In terms of soil slope stability analysis, the saturated/unsaturated seepage analysis is firstly performed by employing the estimated unsaturated coefficient of permeability of grassed soil as one of input parameters to investigate the seepage behavior of grassed soil slope at different grass ages. The stability analysis is then carried out to understand the performance of grassed soil slope during long-term period. The results relating to hydraulic properties of Komaoka soil in this study are expected to be employed in further researches which numerically investigates the effects of grass on the instability of soil slopes

7 MECHANICAL PROPERTIES OF GRASSED SOIL

7.1 Introduction

Soil shear strength at the potential slip surface of slope is increased due to the enhanced shear strength provided by roots. As a result, the shallow landslide-prone areas might be resisted due to the effective mechanical effects of vegetation. Shear strength behaviors of root-reinforced soil were studied by direct shear test in both experimental laboratory and in-situ condition (Fan and Su 2008, Wood et al. 2016, Mahannopkul and Jotisankasa 2019, Yildiz et al 2020). The drawback of the direct test is that the failure plane is commonly assumed. However, stress and strain in a sample are complicated and the weakest surface may not be the assumed shear plane in reality. Shear strength, stress-strain relationship, and changes of the sample volume can be measured simultaneously in triaxial test. Few past researches employed the root-induced changes in shear strength properties of vegetated soils to numerically access the stability of unsaturated soil slope (Ni et al. 2018b). The cohesion of rooted soils in these researches was empirically estimated by Wu et al (1998), and Liang et al (2020) models. There is limited research that determines the effect of natural roots on an increase in shear strength properties of soils by triaxial test. The effects of roots on shear behaviours of vegetated soil slope are more properly determined by employing shear strength parameters of rooted soil which are studied from the triaxial test.

This chapter investigated the effect of grass roots on the mechanical properties of saturated soil. Triaxial test apparatus was employed to investigate the shear behaviours of the grassed soil. A series of saturated monotonic CD triaxial compression tests were performed on root-reinforced soils with different grass ages. The relationship between root volume ratio and maximum deviator stress, effective cohesion, and the effective angle of internal fraction are studied. Furthermore, the unsaturated shear strengths of grassed soil at different grass ages are estimated by employing Vanapalli model (1996) model.

7.2 Overview of triaxial test apparatus

Figure 7.1 shows an overview of the test apparatus which have been used in this research for the triaxial compression tests. The size of soil specimen is 70 mm in diameter and 170 mm in height. Figure 7.2 illustrates rear of the apparatus. Procedures for preparing triaxial test before consolidation step are explained as follows:

- Smearing silicon grease on side surface of cap and pedestal.
- Mounting membrane to the pedestal then installing O-Rings from the outside of membrane to keep good contact between membrane and pedestal.
- Assembling mold then installing O-Rings on the top of the mold.
- Applying vacuum of about 5 kPa to the void between mold and membrane to ensure good contact between membrane and mold.

- Inserting prepared grassed soil specimen into the mold.
- Putting Polyflon filter on the top of the specimen.
- Installing upper plane meanwhile keeping cap from contacting test specimen. Calibrating the load cell.
- Lowering the cap to a height at where the bottom of the cap just contacts the top of the test specimen. Mounting the membrane to the cap. After that, O-Rings are installed.
- Applying a vacuum of about 20 kPa from the top of the test specimen to keep specimen's cylindrical shape.
- Releasing applied vacuum between mold and membrane. After that, removing the mold with caution.
- Measuring the size of specimen.

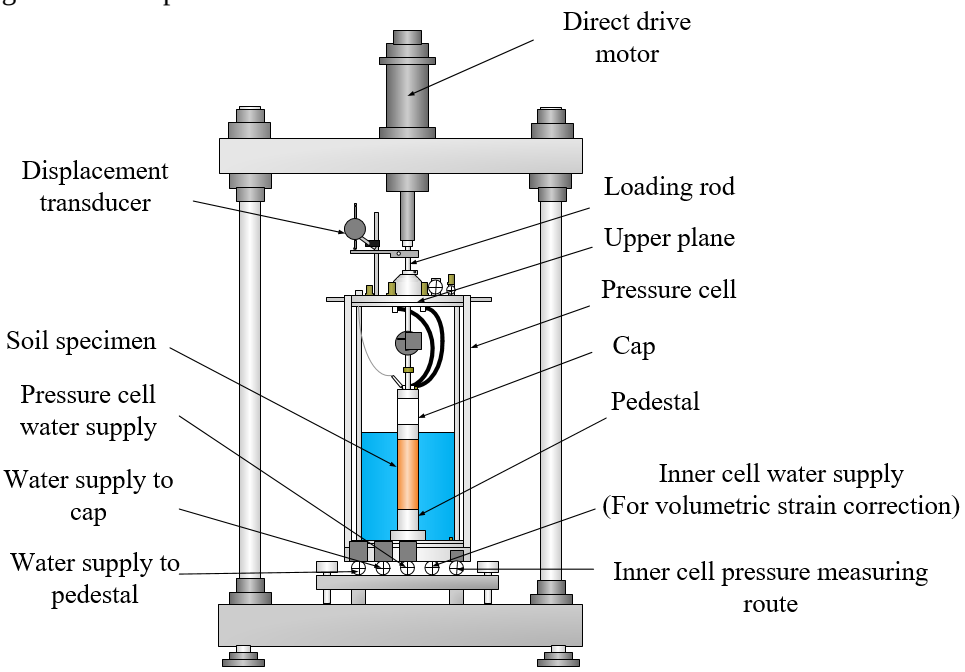

Figure 7.1 Schematic diagram of the triaxial test apparatus.

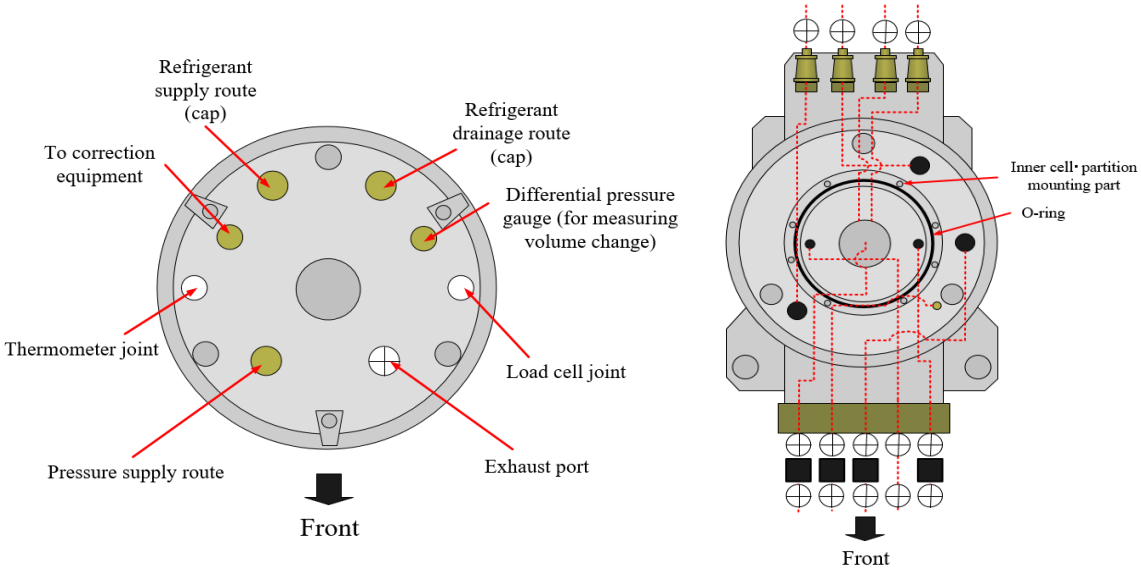

Figure 7.2 Rear of triaxial apparatus.

7.3 Soil specimen preparation

PVC mold with an internal diameter of 70 mm and height of 200 mm was used to prepare the soil specimens. The PVC mold was pre-cut along the axial axis and held with tapes and clamps which were later released when the soil specimens were removed for testing. Komaoka soil with volumetric water content of 24.5% was mixed by quartering method (JGS 2009b) to establish the identical soil water content and uniformity in grain-size distribution. Next, the air pluviation method and slight compaction were employed to make Komaoka soil specimen. The soil specimens have the same in-situ porosity and in-situ dry density as presented in Table 3.1. The soil specimen has 170 cm in high and 70 cm in diameter. After that, the mixture of grass seeds, which used in grassed soil slope as mentioned above, was uniformly germinated on the surface of Komaoka soil specimens. All soil specimens were placed inside growth room with regulated temperature (around 25 ºC). In addition, the fluorescent bulbs were used to simulate daylight (Figures 7.3 and 7.4).

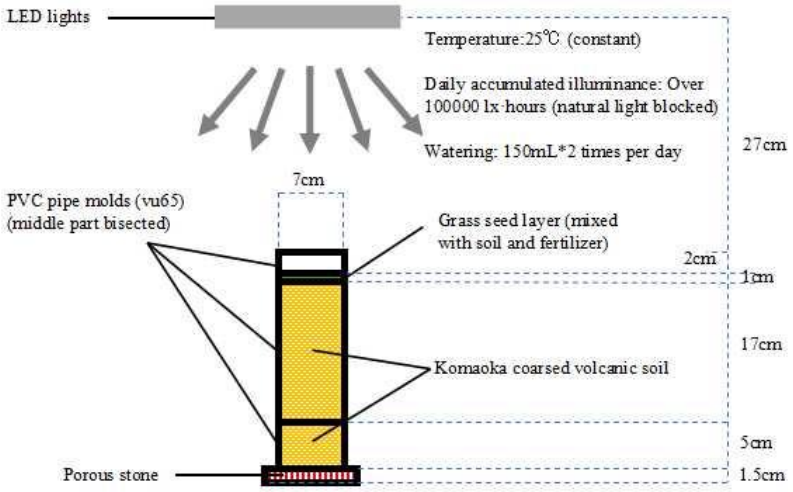

Figure 7.3 Instruction of indoor cultivation.

Figure 7.4 Example of grassed soil specimens in growth room.

The soil specimens were placed on the porous stone for two days for internal drainage when the grasses have grown to a certain age varying from 1 month to 8 months. When the specimens reach the designated ages, the specimens were firstly trimmed, and only soil-root structures inside the middle parts of mold (7 cm in diameter, 17 cm in height bisected into two halves) are reserved. The reserved specimens were covered with 2 filter papers at both top and bottom ends. They were also sealed by wrapper with rubber rings. Finally, the trimmed specimens were put into refrigerator at -20 ℃ for over 12 hours to give them a tough shape so that they could be directly set into the triaxial apparatus with undisturbed root structures inside of the soil.

The mold was then released after moving out soil specimens from the refrigerator. After that, the soil specimen was accommodated into the triaxial test apparatus. The examples of grassed soil specimens and grass roots at the grass age of two months are presented in Fig. 7.5. Two replicates were used for each soil specimen to verify and improve the universality of the test results.

(a) (b)

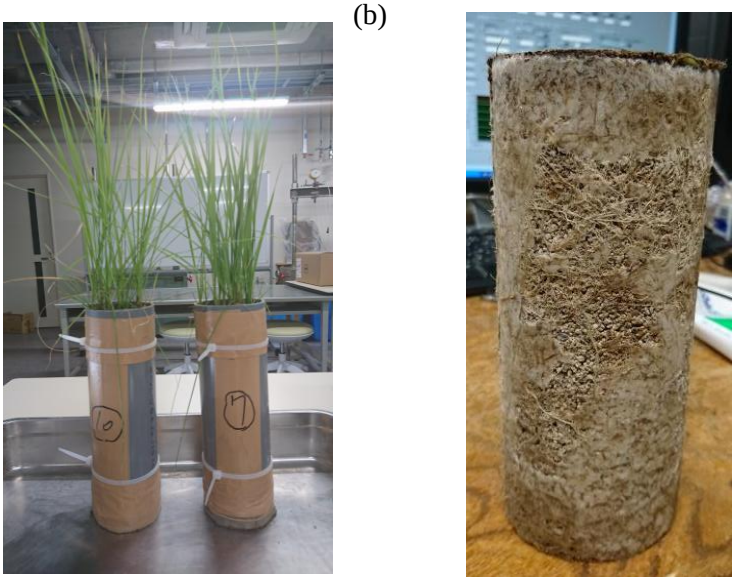

Figure 7.5 Specimens after cultivating and after trimming and freezing

7.4 Experiment procedures

7.4.1 Consolidation process

Monotonic triaxial compression tests were conducted after specimen preparation. At first, each frozen specimen was set into a pressure cell under a cell pressure of 20 kPa for unfreezing. It was followed by the consolidation process. Double vacuuming method which extracted the pore air from the top of the specimen by giving a negative air pressure for saturated condition, was employed to saturate soil specimen. Meanwhile, de-aired water was supplied from the bottom of the specimen. Next, a backpressure up to 200 kPa was applied to make sure that the B value would excess 0.96. When the soil specimen was fully

saturated, the isotropic consolidation would continue in fully drained condition under preset effective confining pressures ($\sigma_{c'}$) of 25 kPa and 49 kPa. Cell pressures (σ_c) of 225 and 249 kPa respectively and pore water pressure (u_w) of 200 kPa were applied till there were no changes in axial displacement or in drainage volume.

7.4.2 Shear process

After completing consolidation process, soil specimen was sheared continuously by applying an axial deviator stress (q) under fully drained condition (CD test). The shear velocity for volcanic soil was set to 0.2 %/min (Ishikawa et al. 2010). The shear process was finished as the axial strain (ε_a) reached 25%.

7.5 Results and discussions

7.5.1 Shear behavior of grassed soil

The relationship between deviator stress (q), volumetric strain (ε_v), and axial strain (ε_a) of grassed soils with different grass ages during CD test under saturated condition are presented in Figůe 7.6. BK and GK in this figure denote the bare Komaoka soil and grassed Komaoka soil, respectively. It is followed by the grass age (e.g. GK-1)

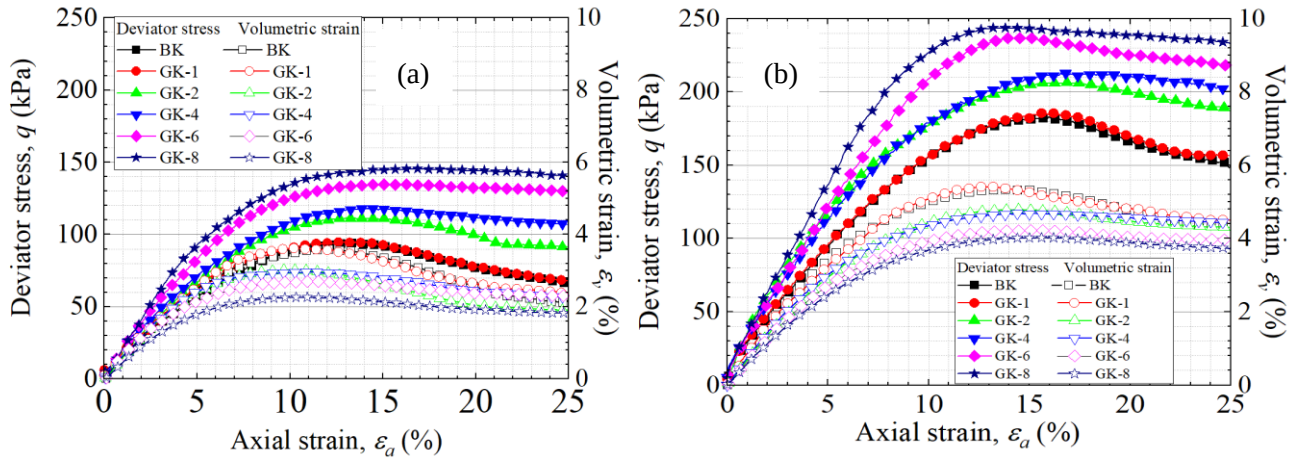

Figure 7.6 Shear behaviors of soils at effective confining pressures of (a) 25 kPa, and (b) 49 kPa.

It can be seen that the peak shear strength of grassed soil is higher than that of bare soil, excepting the grass soil at the growing age of 1 month. In addition, there is an increase in peak shear strength of grassed soil with higher grass age. In contrast, the maximum volumetric strains in grassed soil is lower than that of bare soil. Soil with higher grass age has a lower maximum volumetric strain. The volumetric strains of bare soil increase (strain hardening) and reach peak at the axial strain of somewhere in the vicinity of 10 % and 15 % under confining stress of 25 kPa and 49 kPa, respectively. After that, the volumetric strains dramatically decrease (strain softening) as the axial strain increase continuously. However, the hardening

behavior of grassed soils is still observed after the volumetric strain reaching the peak values. Volumetric strains of grassed soils, which have grass age higher than 2 months, remain constant or slightly decrease after reaching the peak values. The reason for these phenomena is attributed to the effects of grass roots. As the axial strain increases, the friction between roots and soil particles resists the volume expansion. In addition, not only the shear strength of soil but also the tensile strength of roots resists the shear stress due to applying load. As a result, there is a higher peak shear strength and smaller volumetric strain in grassed soils as compared to that in bare soil.

7.5.2 Relationships between root volume ratio and peak shear strength

The root volume ratio (R_v) is defined as the volume of roots to the volume of soil specimen (V_r/V). Fig 7.7a indicated that the root volume ratio is higher as grass age increases. As root volume ratio rises corresponding to an increase in grass age, the friction force between root and soil particles is increased because there is a larger contact area between the root-soil interface. This results in better mobilization of soil-root surficial interaction. Therefore, the shear stress of grass root significantly increases, whereas the volumetric strain decreases with the rise in grass age. It is noted that the diameters of grass root might be higher when grass becomes older (Leung et al. 2018). Several past studies reported that the tensile strength of root decreases with the increase in root diameter (De Baets et al. 2008, Loades et al. 2010). Therefore, the enhanced shear strength and reduced volumetric strain observed in this study are attributed to the higher root volume ratio. The relationships between peak shear strength with root volume ratio are shown in Figure 7.7b. The results of CD tests for both bare and grassed soils at different grass ages are summarized in Table 7.2.

The average results of shear strengths for both bare soil and grassed soils (Table 7.2) under confining pressures of 25 kPa and 49 kPa are employed to draw Mohr-Column failure envelopes as presented in Fig. 7.8. The shear strength of saturated soil can be described using the Mohr-Coulomn failure criterion and the effective stress variable (Terzaghi 1936) as presented in Eq. 7.1.

$$\tau_{ff} = c' + \left(\sigma_f - u_w\right)_f \tan\phi' \tag{7.1}$$

where τ_{ff} is shear stress on the failure plane at failure; c' is effective cohesion; $(\sigma_f - u_w)_f$ is effective normal stress on the failure plane at failure; σ_{ff} is total normal stress on the failure plane at failure; u_{wf} is pore-water pressure at failure; ϕ' is effective angel of internal fraction.

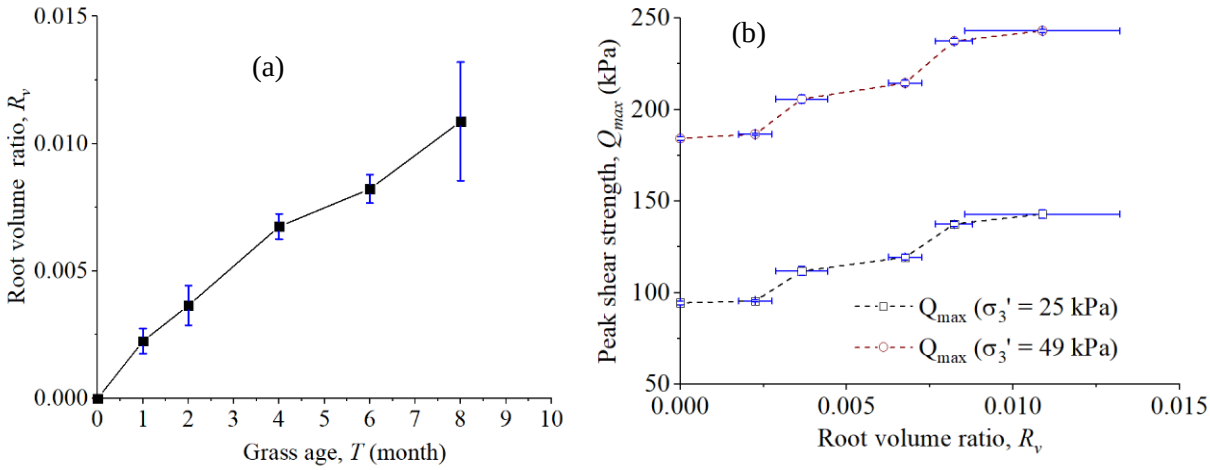

Figure 7.7 Relationship between (a) grass age and R_v, (b) peak shear strength and R_v.

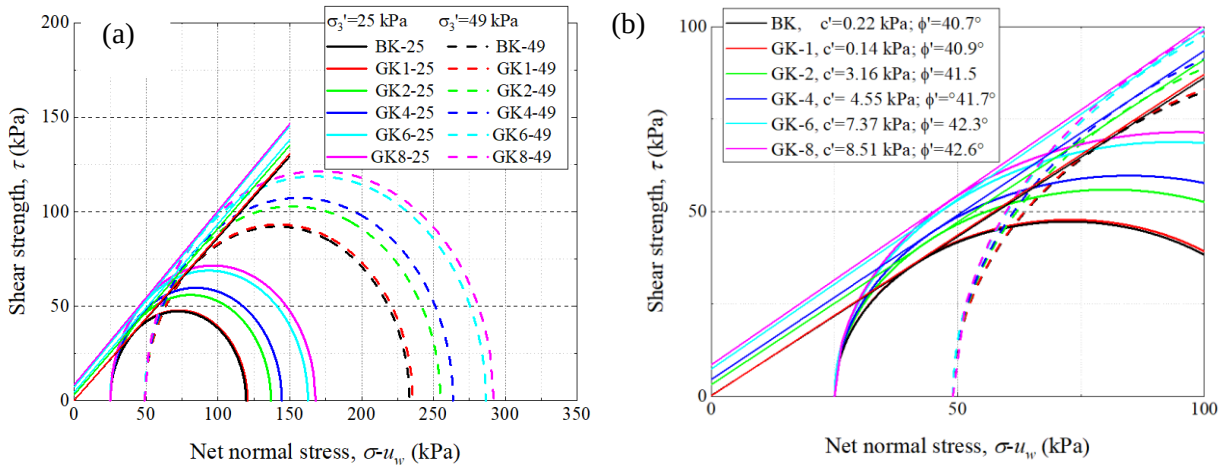

Figure 7.8 (a) Mohr-Column failure envelopes of bare soil and grassed soils, and (b) details in *c'* and φ'.

Fig. 7.9a shows that there is a significant increase in effective cohesion (*c'*) of grassed soil with the increase in root volume ratio. The bare soil has effective cohesion of 0.22 kPa which indicates that the volcanic soil is considered as cohesionless soil. The effective internal friction (ϕ') of grassed soil just exhibits a slight increase as root volume ratio increase (Fig. 7.9b). The effective internal friction of soil with grass age of 8 month is just higher than that of bare soil by around 1.8 ° (40.7° as compared to 42.5°, respectively). The higher effective cohesion might also contribute to the higher shear stress of grassed soil with higher grass age as mentioned above. Effective cohesion (*c'*) and effective internal friction (ϕ') of grassed soil might be estimated based on R_v (2.25E-3 ≤ R_v ≤ 1.087E-2) as presented in Eqs. 7.2 and 7.3, respectively.

$$c' = 933.41R_v - 1.18 \tag{7.2}$$

$$\phi' = 189R_v + 40.62 \tag{7.3}$$

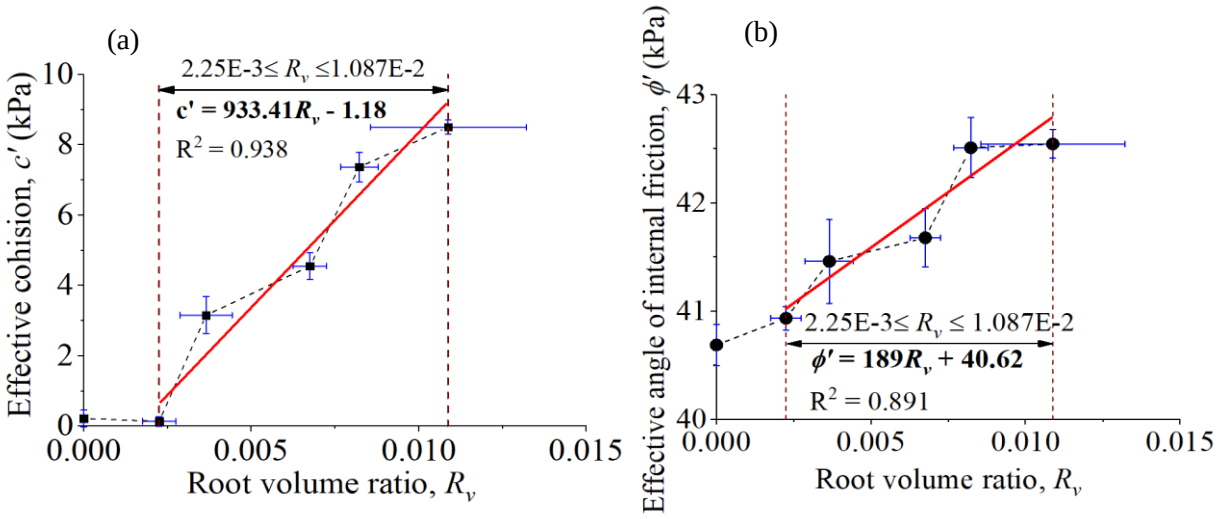

Figure 7.9 Relationship between (a) root volume ratio and effective cohesion, and (b) root volume ratio and effective angle of internal friction.

Table 7.1 Shear strength properties of soils.

Description	BK	GK-1	GK-2	GK-4	GK-6	GK-8
Peak shear strength at σ_3' = 25 kPa, Q_{max}^{25} (kPa)	Mean: 94.5 S.D.: ± 1	Mean: 95.5 S.D.: ± 0.6	Mean: 111.9 S.D.: ± 2.5	Mean: 119.4 S.D.: ± 1.6	Mean: 137.6 S.D.: ± 1.3	Mean: 142.9 S.D.: ± 2.3
Peak shear strength at σ_3' = 49 kPa, Q_{max}^{49} (kPa)	Mean: 184.3 S.D.: ± 0.99	Mean: 186.6 S.D.: ± 0.57	Mean: 205.8 S.D.: ± 2.1	Mean: 214.6 S.D.: ± 1.5	Mean: 237.5 S.D.: ± 1.6	Mean: 243.1 S.D.: ± 0.8
Effective cohesion, c' (kPa)	Mean: 0.22 S.D.: ± 0.24	Mean: 0.14 S.D.: ± 0.14	Mean: 3.16 S.D.: ± 0.53	Mean: 4.55 S.D.: ± 0.38	Mean: 7.37 S.D.: ± 0.42	Mean: 8.51 S.D.: ± 0.20
Effective root cohesion, c_r' (kPa)	0	0	2.94	4.33	6.95	8.29
Effective internal friction angle, ϕ' (°)	Mean: 40.7 S.D.: ± 0.19	Mean: 40.9 S.D.: ± 0.11	Mean: 41.5 S.D.: ± 0.39	Mean: 41.7 S.D.: ± 0.27	Mean: 42.3 S.D.: ± 0.28	Mean: 42.6 S.D.: ± 0.13

S.D stands for standard deviation

7.5.3 Shear strength of grassed unsaturated soil

Fredlund et al. (1979) assumed that the linear form of the shear strength for unsaturated soil can be formulated in terms of independent stress state variables as shown in Fig. 7.10. The location of the Mohr circle plot in the third dimension is a function of the matric suction. The surface tangent to the Mohr circles at failure is referred to as the extended M-C failure envelope for unsaturated soils. The extended M-C failure envelope defines the shear strength of unsaturated soil. The intersection line between the extended M-C failure envelope and the frontal plane is the failure envelope for saturated conditions. The shear strength of an unsaturated soil is expressed based on Bishop's effective stress principle by Vanapalli et al. (1996) as given by:

$$\tau = c' + (\sigma_n - \sigma_a)\tan\phi' + (u_a - u_w)\tan\phi^b \tag{7.4}$$

where, τ (kPa) is shear strength of soil, σ_n (kPa) is net total stress, u_a (kPa) is pore air pressure, u_w (kPa) is pore water pressure, c' (kPa) is effective cohesion, ϕ' (°) is effective angle of internal friction, ϕ^b (°) is the indicating the rate of increase in shear strength with respect to a change in matric suction (tan ϕ^b = χ tan ϕ'), and χ is parameter related to the degree of saturation. According to Vanapalli et al. (1996), the magnitude of parameter χ can be expressed in terms of volumetric water content as follow:

$$\chi = (\theta_w - \theta_r)/(\theta_s - \theta_r) \tag{7.5}$$

where, θ_w (m^3/m^3) is volumetric water content, θ_s (m^3/m^3) is saturated volumetric water content (m^3/m^3) and θ_r (m^3/m^3) is residual volumetric water content.

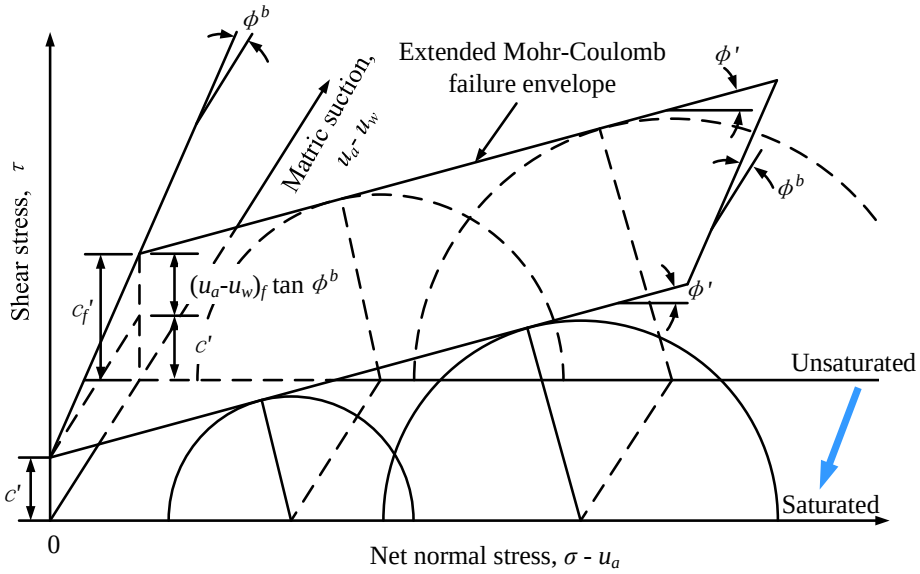

Figure 7.10 Three-dimensional extended M-C failure envelope for unsaturated soils (Fredlund et al. (1979)).

By substituting Eqs. 7.2 and 7.3 to Eq. 7.4, shear strength of grassed unsaturated soil could be estimated as following:

$$\tau = (933.41R_v - 1.18) + (\sigma_n - \sigma_a)\tan(189R_v + 40.62) + (u_a - u_w)\tan\phi^b \quad (7.6)$$

The unsaturated shear strengths of grassed soil at different grassed ages are estimated based on Eq. 7.6. A procedure of estimating unsaturated shear strength of grassed soil are indicated in Fig. 7.11. Fig. 7.12 shows an example of shear strength of grassed unsaturated soil at net normal stress of 7 kPa. It can be seen that higher grass age might lead to higher unsaturated shear strength of grassed soil.

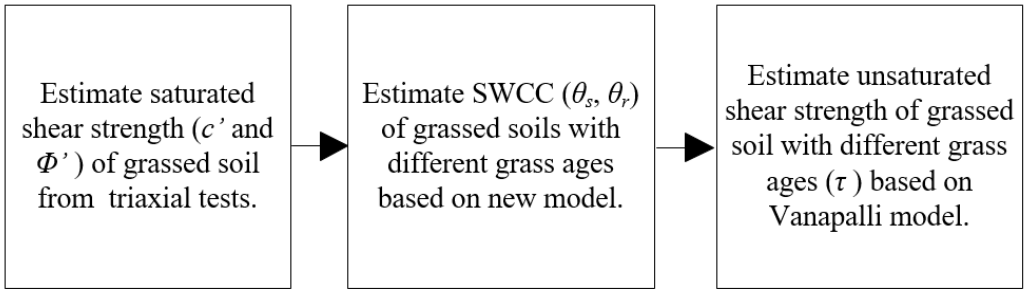

Figure 7.11 Procedures to estimate unsaturated shear strength of grassed soil.

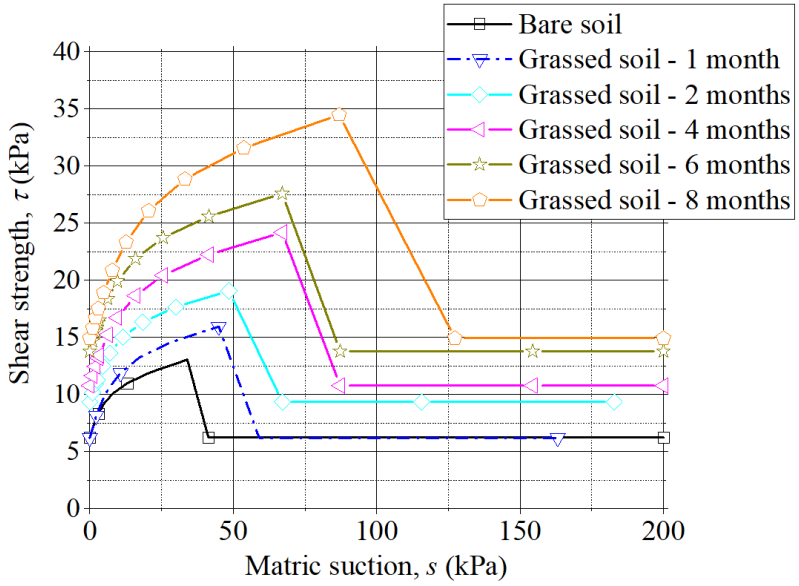

Figure 7.12 Example of shear strength of grassed soil at net normal stress of 7 kPa.

7.6 Summary

This chapter studied the effects of grass age on the shear behaviours (i.e. deviator stress, volumetric strain, and axial strain) of the grassed saturated soil with different grass ages by conducting triaxial tests. Grassed soils with different grass ages varying from 1 month to 8 months were selected to study. Two different effective confining pressures of 25 kPa and 49 kPa were employed as a representative of the in-situ confining pressures of soil at the surface layer. After that, the Mohr-Coulomn failure criterion was used to derive effective cohesion (c'), effective angel of internal fraction (ϕ') of grassed saturated soil. The shear velocity for volcanic soil was set to 0.2 %/min and the shear process was finished as the axial strain (ε_a) reached 25% in order to reduce the possibility of excess pore-water pressure during consolidation and shear process.

The experimental results from CD tests presented that shear strength of root permeated soil was enhanced. There is an increase in effective cohesion (c'), effective angel of the internal fraction (ϕ'), and peak shear strength (Q_{max}) with the increase in grass age. In addition, a rise in grass age resulted in a decrease in volume strain. The reason was that the root volume ratio was higher corresponding to the rise in grass age. As the axial strain increases, the friction between roots and soil particles resisted the volume expansion. Besides, not only the shear strength of soil but also the tensile strength of roots resisted the shear stress due to applying load. Higher root volume ratios lead to a higher tensile strength of roots and greater friction between roots and soil particles. As a result, there was a higher peak shear strength and smaller volumetric strain in grassed soils with higher grass age.

The unsaturated shear strength of grassed soil estimated based on Vanapalli model (1996) shown that there might be an increase in unsaturated shear strength of grassed soil when grass age is higher. However, experiments employing triaxial tests should be further conducted to validate the estimated results.

8 SLOPE STABILITY ANALYSIS CONSIDERING EFFECTS OF GRASS ON HYDRO-MECHANICAL PROPERTIES

8.1 Introduction

Cui et al. (2005, 2010) and An et al. (2018a,b) examined the hydro-thermal behavior of embankment under climate effects. The numerical approach proposed in these studies reproduced well as compared to the field monitoring data for bare soil. On the contrary, numerical simulation approach which considers the influence of vegetation on hydro-thermal properties of unsaturated soil is not well understood. Pagano et al. (2019) reported that the hypothesis of bare soil cannot be used to analyses vegetated conditions. Nguyen et al (2017), Shao et al (2017), and Ni et al. (2018a) reported that the seepage behavior under rainfall infiltration in vegetated soil could be reasonably predicted if the hydraulic properties of vegetated soil including SWCC and saturated/ unsaturated coefficient of permeability are properly considered. Several numerical studies were performed to evaluate the effect of evapotranspiration on only hydraulic behaviors of soil. However, vapor transport was not taken into account in the numerical simulation (Ni et al 2018b, Ni et al. 2019a, Ng. et al 2019). It is noted that considering the coupled transport of heat and water in soil is important when investigating the hydro-mechanical behavior of soil during evaporation (An et al. 2018a). Therefore, vapor transport plays an important role to properly study the soil water content near the soil surface. Ni et al. (2019) presented that soil temperature has influences on transpiration. The root water uptake is inhibited due to low soil temperature. Without considering soil temperature effects on transpiration, the soil water content was underestimated by around 50% in the autumn period. Since only the seepage analysis has been performed in Ni et al. (2019) study, soil temperature near the surface was estimated based on the empirical model. The coupled non isothermal-seepage analysis, which takes both the vapor transport and the effect of vegetation cover on the reduction of soil temperature into account, is useful to the numerical assessment of vegetated soil slope performance.

This chapter aims to propose an approach of coupled nonisothermal-seepage numerical analysis for unsaturated soil slope considering hydro-thermal impacts of grass. The proposed approach then was validated by comparing simulation and field measurement results. Furthermore, the slope stability analysis had been performed by employing both volumetric water content and soil temperature distributions from coupled nonisothermal-seepage numerical analysis with consideration of the effects of grass on the mechanical properties of soils. The factor of safety of grassed slope and bare slope were compared to study the beneficial hydro-mechanical effects of grass on soil slope.

8.2 Numerical simulation approach

The incoming energy from net radiation is received for heating ground surface and evaporation in bare slope. However, net radiation is partially intercepted by grass leaves and the rest of net radiation reach to

heat the soil in grassed slope. As a result, the soil temperature in grassed soil is lower than bare soil. The grass roots have effects on hydraulic properties of soil. Ng et al. 2016a, Ni et al. 2019, Nguyen et al. 2020 presented that the grassed soil has a higher capacity to retain matric suction than the bare soil. Whereas the coefficient of permeability of the former is lower than that of the latter since soil pores are clogged by grass roots. Furthermore, the grass roots reinforce the shear strength of soil by increasing the effective cohesion and slight increase in effective angel of internal fraction as discussed above.

From above-mentioned contexts, this study recommends an approach to simulate the soil water content/matric suction and soil temperature of grassed unsaturated soil slope. The non-isothermal seepage simulation is performed and followed by a slope stability assessment as explained in the flow chart shown in Fig. 8.1. The non-isothermal seepage simulation is to predict a soil water content/matric suction and soil temperature distributions inside grassed soil slope under climate variations. Grass-soil-atmosphere interactions are modelled under the climatic variations (i.e. rainfall, air temperature, net radiation, windspeed, relative humidity) using various governing equations as briefly explained in the next following sections. The effects of grass on reducing net radiation and modifying hydraulic properties (e.g. SWCC) are considered. Next, a traditional limit equilibrium technique based on the Morgenstern and Price (1965) method is used to compute the factor of safety (FOS) in the slope stability analysis. The reinforced shear strength of soil due to grass roots is properly considered and will be discussed in a later section. The proposed numerical simulations are performed using a finite element code, namely: SVOFFICE 2009^{TM} (SoilVison Systems Ltd, Saskatoon, Saskatchewan, Canada). SVFlux and SVHeat modules of SVOFFICE 2009^{TM} (SoilVison Systems, 2009a,b) are used to perform nonisothermal coupled seepage flow. It is followed by employing SVSlope (SoilVison Systems, 2009c) module to conduct the slope stability analyses.

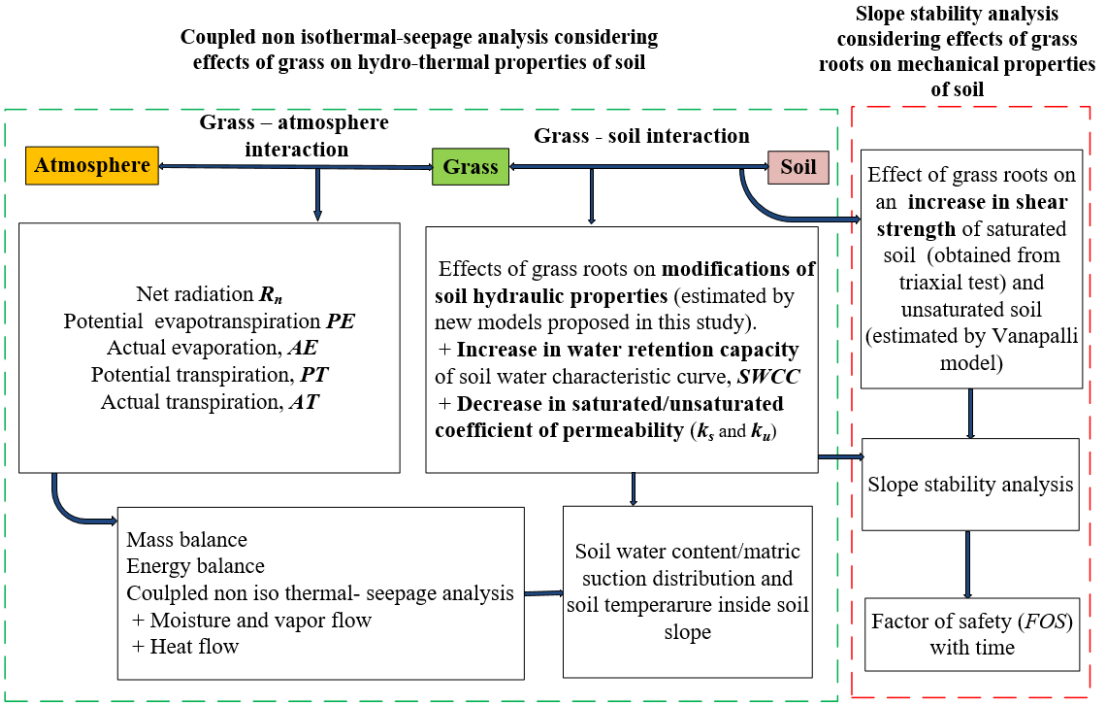

Figure 8.1 Scheme of the proposed numerical analysis procedure for grassed soil slope.

8.3 Governing equations

8.3.1 Atmospheric flux balance

The mass balance at the soil surface is expressed as follows:

$$P = I + RO + AE \tag{8.1}$$

where P (m/day) is the flux of rainfall; I (m/day) is the infiltration rate; RO (m/day) represents the runoff rate on soil surface; AE (m/s) is the actual evaporation rate.

The energy balance at the soil surface is expressed as follows:

$$R_n = G + L + H \tag{8.2}$$

where R_n (MJ.m^{-2}.day^{-1}) is the net radiation flux; G (MJ.m^{-2}.day^{-1}) is the soil heat flux; L (MJ.m^{-2}.day^{-1}) is the latent heat flux; H (MJ.m^{-2}.day^{-1}) is the sensible heat flux.

8.3.2 Coupled non iso-thermal seepage flow

Moisture and vapor flow beneath soil surface are governed by hydraulic head gradients, vapor pressure gradients and temperature gradients. Moisture flow governing equation is presented as follows:

$$\frac{\partial}{\partial x}\left[\left(k_x^{\mathrm{w}} + k^{vd}\right)\frac{\partial h}{\partial x}\right] + \frac{\partial}{\partial y}\left[\left(k_y^{\mathrm{w}} + k^{vd}\right)\frac{\partial h}{\partial x} - k^{vd}\right] + S_{root} = -\gamma_{\mathrm{w}} m_2^w \frac{\partial h}{\partial t} \tag{8.3}$$

where h (m) is total hydraulic head; k_x and k_y (m/day) are coefficient of permeability of soil in x- and y – directions, respectively; k^{vd} (m/s) is pore-water vapor conductivity by vapor diffusion within the air phase; S_{root} is actual transpiration sink term (1/day); γ_w is unit weight of water (9.81 kN/m^3); m_2^w is slope of soil-water characteristic curves.

The heat transfer beneath soil surface is mainly governed by thermal conduction. Heat flow governing equation is given as follows:

$$\frac{\partial}{\partial x}\left(\lambda_x \frac{\partial T}{\partial x}\right) + \frac{\partial}{\partial y}\left(\lambda_y \frac{\partial T}{\partial y}\right) = (C + L_f m_2^i)\frac{\partial T}{\partial t} \tag{8.4}$$

where λ_x, λ_y (J/m.day.°C) are thermal conductivity of soil in x-, y-directions, respectively; C (J/m^3 °C) is volumetric heat capacity of soil; L_f (J/m^3) is volumetric latent heat of soil; m_2^i (m^3/m^3. °C) is the rate of change in unfrozen water content with temperature (e.g the slope of soil freezing characteristic curve); T (°C) is temperature; t (day) is time.

8.3.3 Net radiation

The net radiation (R_n (MJ.m^{-2}.day^{-1})). is the difference between the incoming net shortwave radiation (R_{ns}) and the outgoing net longwave radiation (R_{nl} (MJ.m^{-2}.day^{-1})).

$$R_n = R_{ns} - R_{nl} \tag{8.5}$$

The net shortwave radiation is calculated as follows:

$$R_{ns} = (1-\alpha)R_s \tag{8.6}$$

where α is a canopy reflection coefficient, which is 0.23 for the hypothetical grass reference crop, *Rs* is the incoming solar radiation (MJ.m^{-2}.day^{-1}).

The net longwave radiation is expressed as follows:

$$R_{nl} = \sigma \left[\frac{T_{max,K}^4 + T_{min,K}^4}{2} \right] \left(0.34 - 0.14\sqrt{e_a}\right) \left(1.35 \frac{R_s}{R_{so}} - 0.35\right) \tag{8.7}$$

where σ is Stanfan-Boltzmann constant (4.903E-9 MJ.K^{-4}.m^{-2}.day^{-1}); $T_{max,K}$ and $T_{min,K}$ (K) are maximum and minimum absolute temperature during 24 hour period; e_a is actual vapor pressure; R_s/R_{so} is relative shortwave radiation; R_s (MJ.m^{-2}.day^{-1}) is solar radiation; and R_{so} (MJ.m^{-2}.day^{-1}) is clear-sky radiation.

$$R_{so} = (0.75 + 2\,10^{-5} z) R_a \tag{8.8}$$

where z (m) is the station elevation above sea level.

The extraterrestrial radiation for daily periods (R_a) for each day of the year can be estimated from solar constant:

$$R_a = \frac{24(60)}{\pi} G_{sc} d_r \left[\omega_s \sin\varphi \sin\delta + \cos\varphi \cos\delta \sin\omega_s\right] \tag{8.9}$$

where G_{sc} is solar constant (0.082 MJm^{-2}min^{-1}); d_r is inverse relative distance Earth-Sun; ω_s is sunset hour angle (rad); φ is latitude (rad); δ is solar declination (rad).

The inverse relative distance of Earth-Sun (d_r) and solar declination (δ) are given by:

$$d_r = 1 + 0.033 \cos\left(\frac{2\pi}{365} J\right) \tag{8.10}$$

$$\delta = 0.409 \sin\left(\frac{2\pi}{365} J - 1.39\right) \tag{8.11}$$

where J is the number of the day in the year.

The sunset hour angle can be computed using arctan function:

$$\omega_s = \frac{\pi}{2} - \arctan\left[\frac{-\tan\varphi \tan\delta}{X^{0.5}}\right] \tag{8.12}$$

$$X = 1 - \left[\tan\varphi\right]^2 \left[\tan\delta\right]^2 \tag{8.13}$$

The net radiations for bare slope and grassed slope are computed and shown in Fig. 8.2. The net radiation in the latter is lower than that in the former. The reason is that the grass leaves partially prevent net radiation from reaching to the soil surface (Blight 2002). This phenomenon results in the lower soil temperature in grassed soil slope as compared to bare soil slope as presented in field measurement result.

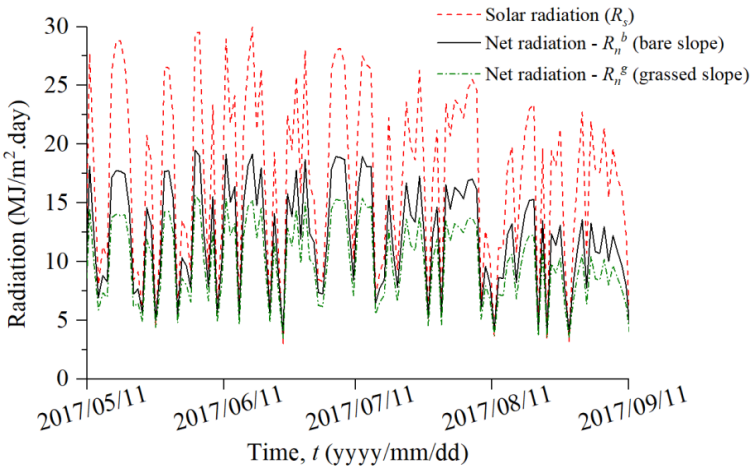

Figure 8.2 Net radiation reaching bare slope and grassed slope

8.3.4 Potential evapotranspiration

The amount of potential evapotranspiration in vegetated soil is calculated based on FAO Penman-Monteith equation (Allen et al. 1998) as follows:

$$PE_g = \frac{0.408\Delta\left(R_n - G\right) + \gamma \frac{900}{T+273} u_2 \left(e_s - e_a\right)}{\Delta + \gamma\left(1 + 0.34u_2\right)} \tag{8.14}$$

where ET_0 is reference evapotranspiration (mm.day^{-1}); R_n is net radiation at the crop surface (MJ.m^{-2}.day^{-2}), G is soil heat flux density (MJ.m^{-2}.day^{-2}); T is mean daily temperature at 2 m height (^{o}C); u_2 is wind speed at 2 m height; e_s is saturation vapor pressure (kPa); e_a is actual vapor pressure (kPa); e_s – e_a is saturation vapor pressure (kPa); Δ is slope vapor pressure curve (kPa. ^{o}C^{-1}); γ is psychometric constant (kPa. ^{o}C^{-1}).

$$e^0(T) = 0.6108 \exp\left[\frac{17.27T}{T+237.3}\right] \tag{8.15}$$

where $e^o(T)$ is saturation vapor pressure at the air temperature T (kPa).

$$e_s = \frac{e^o(T_{max}) + e^o(T_{min})}{2} \tag{8.16}$$

$$e_a = \frac{e^o(T_{min})\frac{RH_{max}}{100} + e^o(T_{max})\frac{RH_{min}}{100}}{2} \tag{8.17}$$

where e_a is actual vapour pressure (kPa), $e^o(T_{min})$ is saturation vapor pressure at the air daily minimum temperature T_{min} (kPa), $e^o(T_{max})$ is saturation vapour pressure at the air daily maximum temperature T_{max} (kPa), RH_{max} is maximum relative humidity (%), RH_{min} is minimum relative humidity (%).

Potential evaporation from bare soil (PE_b (mm/day)) can be estimated as follow:

$$PE_b = 1.15 PE_g \tag{8.18}$$

8.3.5 Actual evaporation

The prediction of actual evaporation (AE) is required when calculating the net moisture flux from the ground surface to the atmosphere. The proposed Wilson-Penman equation could predict reasonable the AE from saturated clayey soils. However, AE from coarse-grained soils in arid regions is overpredicted. To deal with this problem, two distinct approaches have been proposed for the better prediction of AE from unsaturated soil surfaces by attempting to take the effects of "surface resistance" into consideration. Surface resistance is defined as the resistance to water vapor diffusion from near the soil surface (Aluwihare and Watanabe 2003). The original usage of the term was in connection with evaporation from leaves and vegetated ground surfaces (i.e., the canopy effect) (Monteith 1965). Aluwihare and Watanabe (2003) were illustrated surface resistance as shown in Fig. 8.3.

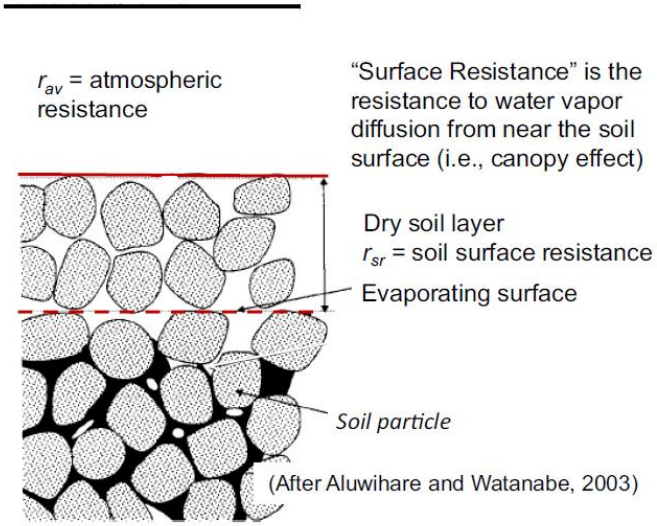

Figure 8.3 Illustration of the surface resistance effect on a dry, coarsegrained soil (after Aluwihare and Watanabe 2003)

The calculation of AE from an unsaturated soil surface is important to assess ground surface infiltration. Models that have been proposed and used in geotechnical engineering for calculation of evaporative flux can be divided into two broad categories: those that take surface resistance into consideration and those that do not take surface resistance into consideration (Fig. 8.4). The classification of evaporation models into these two broad categories presents that surface resistance is a significant parameter when AE is considered. Fig. 8.4 shows that both Wilson (1990) and Wilson et al. (1997) models for AE have been incorporated into numerical models in two different method. In the first method, surface resistance is considered (SoilVision Systems 2009a). Whereas, surface resistance is neglected in the second method (Unsaturated Soils Group 1994; Geo-Slope International Ltd. 2008). When surface resistance has been taken into consideration, the word "modified" has been added (Fredlund et al. 2016).

The effect of surface resistance is particularly significant when considering evaporation from dry, coarse soils in arid regions. It is noted that the Wilson-Penman equation overestimated the rate of evaporation from a sand soil surface and saline soil surfaces (Dunmola, 2012). Tran at al 2014 shown that the reason for the overprediction of AE is attributable to the omission of the surface resistance term. Wilson (1990) also pointed out that osmotic suction effects were not taken into consideration in the Wilson-Penman method. This study employed the latest model proposed by Fredlund et al (2016) which considered the surface resistance in computation of AE.

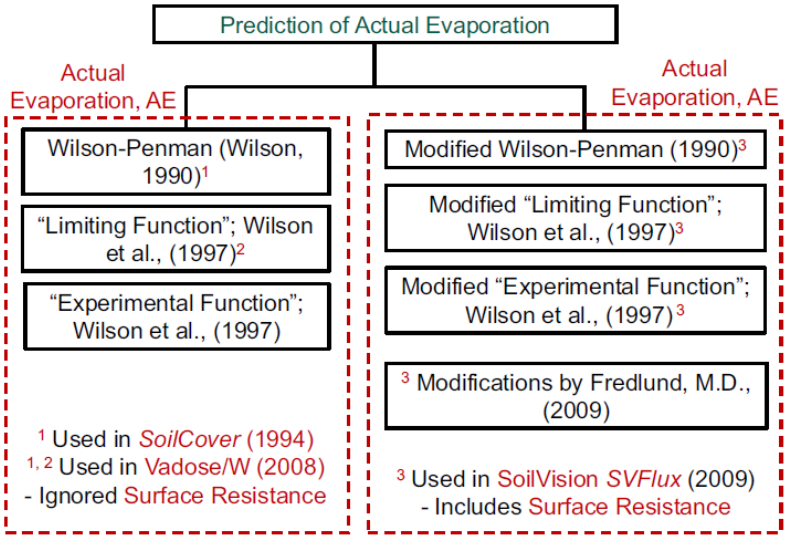

Figure 8.4 Classification of models to predict AE (after Fredlund et al. 2016)

Fredlund et al. (2016) presented an equation to compute a ratio of *AE/PE* as follows:

$$AE / PE = \exp\left(\frac{-sg\omega_v \delta_{corr}}{\zeta(1-RH)\gamma_w R(T_s + 273.15)} \right) \tag{8.19}$$

where ζ is a dimensional empirical parameter with a suggested value of 0.7; *RH* is relative humidity of overlying air; s (kPa) is matric suction; ω_v is molecular weight of water (9.807 kN/m^3); g is gravity acceleration (m/s^2); δ_{corr} is correction factor; R is universal gas constant (8.314 (J/mol.K)); T_s is soil surface temperature (C).

Correction factor (δ_{corr}) is computed as following equation (Fredlund et al, 2016).

$$\delta_{corr} = -\log_{10} s_r + 3.48 \tag{8.20}$$

where s_r (kPa) is residual soil suction. The maximum correction factor for coarse sand soils is 3.48, whereas no correction is required for clayey soils with a high air-entry value.

8.3.6 Actual transpiration

Transpiration is the term used to describe evaporation from vegetated surfaces. Transpiration accounts for the movement of water within plants and the subsequent loss of water as a vapor through stomata in its leaves.

Leaf area index (LAI) presents the effect of the vegetation cover on the energy available to extract the water from the ground surface. The LAI is defined as the surface area of the leaves divided by the surface area covered by the soil. The plant cover with larger LAI has a larger potential to extract water. In the simulation, LAI is used to reduce the amount of net radiation reaching the soil surface, which in turn reduces the computed actual evaporation. In other words, LAI controls how the energy at the surface is portioned between that available for direct evaporation from the soil and that is available to the plants in their attempt to transpire water.

Ritchie (1972) equation is used for the calculation of potential transpiration (PT).

$$PT = 0 \text{ when } \mathrm{LAI} < 0.1 \tag{8.21}$$

$$PT = PE(-0.21 + 0.7\,LAI^{0.5}) \text{ when } 0.1 \le \mathrm{LAI} < 2.7 \tag{8.22}$$

$$PT = PE \text{ when } 2.7 \le \mathrm{LAI} \tag{8.23}$$

where PT (mm/day) is potential transpiration rate, PE (mm/day) is potential evapotranspiration rate.

The zone over which plant transpiration is assumed to extract water is dependent upon the depth of the roots and the distribution of the roots. The grass root zone has a triangular shape in this study. The potential root uptake at a point within the root zone under consideration is defined.

$$PRU = \frac{RSF\ PT}{R_T}\left(1 - \frac{R_n}{R_T}\right) \tag{8.24}$$

where PRU (m^3/day) is potential root uptake rate per unit time, RSF is root distribution shape factor (i.e. triangular), R_t (m) is total thickness of root zone in length units, and R_n (m) is depth to the given point in length units.

The plant limiting factor (PLF) is a function of the soil suction in the root zone. The PLF proposed by Garg et al. (2015) for non-crop plant is shown in Fig.8.5. It was assumed that the grass transpires when soil suction is higher than ‘anaerobiosis point’ and lower than ‘wiling point’. The ability of root water uptake is maximum between 1 kPa (limiting point), and PLF reduces from 1 at around 100 kPa to 0 at 1500 kPa.

Actual transpiration (AT) is calculated by modifying the potential transpiration values when suctions is reduced.

$$AT = (PRU)(PLF) \tag{8.25}$$

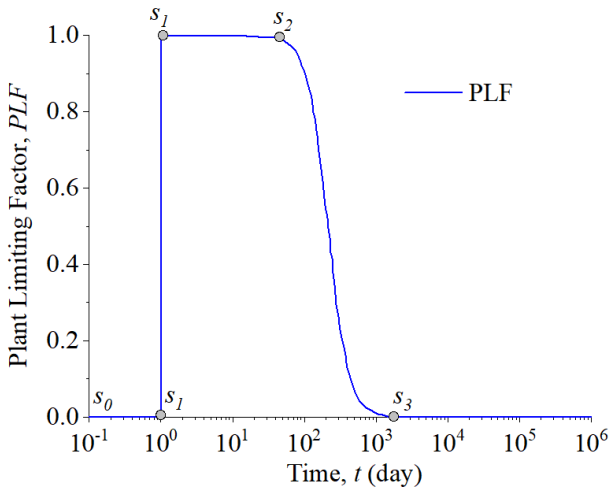

Figure 8.5 Plant limiting factor as suggested by Garg et al (2015).

8.3.7 Shear strength of soil under unsaturated conditions

The shear strength of an unsaturated soil is expressed based on Bishop's effective stress principle by Vanapalli et al. (1996) as given by:

$$\tau = c' + (\sigma_n - \sigma_a)\tan\phi' + (u_a - u_w)\tan\phi^b \tag{8.26}$$

where, τ (kPa) is shear strength of soil, σ_n (kPa) is net total stress, u_a (kPa) is pore air pressure, u_w (kPa) is pore water pressure, c' (kPa) is effective cohesion, ϕ' (°) is effective angle of internal friction, and χ is parameter related to the degree of saturation. According to Vanapalli et al. (1996), the magnitude of parameter χ can be expressed in terms of volumetric water content as,

$$\chi = (\theta_w - \theta_r)/(\theta_s - \theta_r) \tag{8.27}$$

where, θ_w (m^3/m^3) is volumetric water content, θ_s (m^3/m^3) is saturated volumetric water content (m^3/m^3) and θ_r (m^3/m^3) is residual volumetric water content.

When R_v is measured (2.25E-3 ≤ R_v ≤ 1.087E-2), unsaturated shear strength of an grassed soil could be estimated as following:

$$\tau = (933.41R_v - 1.18) + (\sigma_n - \sigma_a)\tan(189R_v + 40.62) + (u_a - u_w)\tan\phi^b \tag{8.28}$$

8.3.8 Factor of safety

Slope stability has been analysed using limit equilibrium technique based on the method given by Morgenstern and Price (1965). The Morgenstern and Price method is a widely used as slope stability method in general geotechnical engineering practice. The factor of safety equations with respect to moment

equilibrium (F_m) and force equilibrium (F_f) considering the unsaturated shear strength of soil are given in Eq. 8.29 and Eq. 8.30 respectively. The unsaturated soil shear strength in the factor of safety is considered based on the nonlinear relationship given by Vanapalli et al. (1996) as explained above.

$$FS_m = \frac{\sum\left[c'lR + \left\{N - u_w l\chi - u_a l(1-\chi)R\tan\phi'\right\}\right]}{\sum W_x - \sum Nf \pm Dd \pm Aa} \tag{8.29}$$

$$FS_f = \frac{\sum\left[c'l\cos\alpha + \left\{N - u_w l\chi - u_a l(1-\chi)\tan\phi'\cos\alpha\right\}\right]}{\sum N\sin\alpha - \sum D\cos\omega \pm A} \tag{8.30}$$

where, W (kN/m^2) is the total weight of a slice of width b and height h, N (kN) is the total normal force on the base of the slice, D (kN) is an external point load. R (m) is the radius of a circular slip surface, x (m)is the horizontal distance from the centerline of each slice to the center of rotation or to the center of moments, d (m) is the perpendicular distance from a point load to the center of rotation or to the center of moments, f (m) is the perpendicular offset of the normal force from the center of rotation or from the center of moments, a (m) is the perpendicular distance from the resultant external water force to the center of rotation or to the center of moments, A (kN) is the resultant external water forces, ω (°) is the angle of the point load from the horizontal, α (°) is the angle between the tangent to the center of the base of each slice and the horizontal and l (m). is the base length of each slice.

8.4 Validation of evaporation model

8.4.1 Introduction of Yanful and Choo's experiment (1997)

Yanful and Choo (1997) measured actual evaporation rates from candidate soils for 40 days. A designed cylindrical column was fabricated from a 6.4 mm thick, ABS (acrylontrile-butadiene-styrene) pipe with an internal diameter of 101.6 mm and a height of 209.6 mm. The column was filled up with candidate soil. A column filled up to the same height with distilled water was placed in the environmental chamber beside the other soil columns. Soil columns were placed in an environmental chamber to maintain control of the temperature, humidity and air circulation. In addition, a column filled to a known height with distilled water was placed in the chamber along with the other soil columns to measure daily potential evaporation rate. Four types of soil in Yanful and Choo's evaporation tests were a topsoil, clay, a fine sand, and coarse sand. Data from fine sand and clay were collected to verify the prediction of evaporation model in this study. SWCC of find sand and clay were fitted by Fredlund and Xing (1994) model, respectively (Fig.8.6a). Whereas the unsaturated coefficients of permeability of these soils were estimated based on above-mentioned fitted SWCCs and measured saturated coefficients of permeability by Fredlund et al. (1994) model as presented in (Fig.8.6b). Soil parameters used in the simulation were summarised in Table. 8.1.

Fredlund and Xing (1994) and Fredlund et al. (1994) equations are shown in Eqs. 8.31 and 8.32.

$$\theta_w = \theta_s \left[1 - \frac{\ln\left(1+\frac{s}{h_r}\right)}{\ln\left(1+\frac{s}{h_r}\right)} \right] \left[\frac{1}{\left[\ln\left[\exp(1) + \left(\frac{s}{a_f}\right)^{n_f} \right] \right]^{m_f}} \right] \tag{8.31}$$

where θ_w (cm^3/cm^3) is volumetric water content at any suction; θ_s (cm^3/cm^3) is saturated volumetric water content; a_f (kPa) is material parameter which is primarily a function of the air-entry value of the soil; n_f is material parameter which is primarily a function of rate of water extraction from the soil once the air-entry value has been exceeded; m_f is primarily a function of the residual water content; h_r (kPa) is suction at residual water content, and s (kPa) is any soil suction value.

$$k_r(s) = \frac{\int_{\ln(s)}^{b} \frac{\theta(e^y)-\theta(s)}{e^y}\theta'(y)dy}{\int_{\ln(s_{aev})}^{b} \frac{\theta(e^y)-\theta_s}{e^y}\theta'(e^y)dy} \tag{8.32}$$

where k_r(s) is relative coefficient of permeability at suction s; s_{ave} (kPa) is air-entry value of the soil; b is equal to ln(1000000); y is dummy variable of integration representing suction; θ' is derivative of Eq. 8.31.

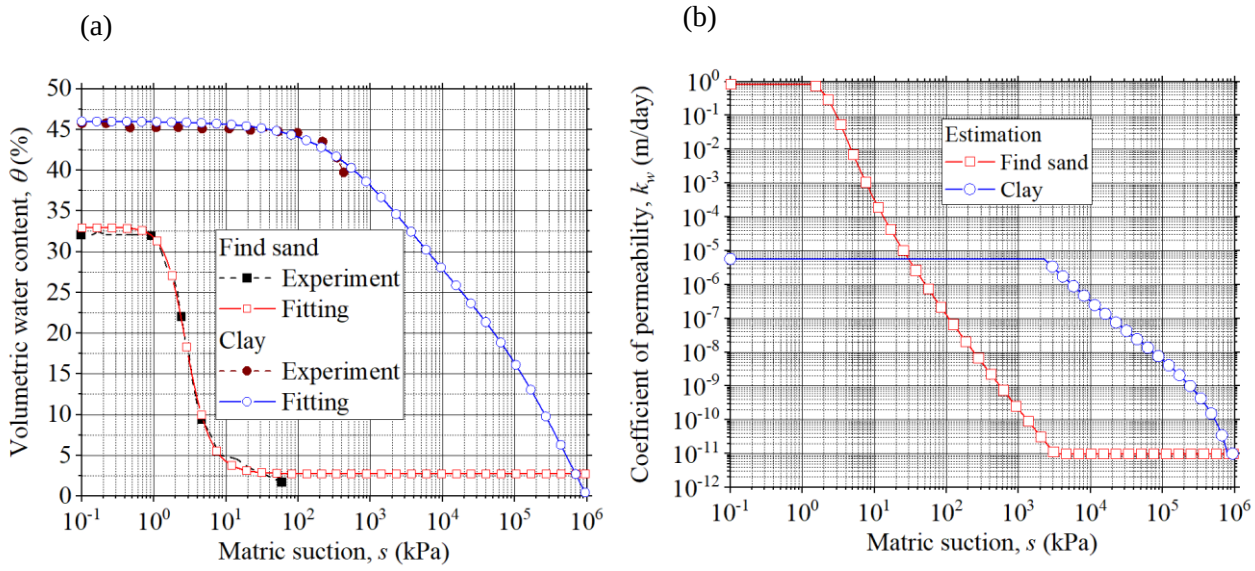

Figure 8.6 (a) SWCC and (b) coefficient of permeability of find sand and clay.

8.4.2 Model geometry and analytical conditions

The evaporation column was simplified in one-dimensional (1D) model as shown in Fig. 8.7. The model had 0.21m height. All lateral edges and the bottom of column were specified as “non-drainage” boundary. Zero pore-water pressure was set for the initial condition of soil, which meant that the soil column was fully saturated at the start of the test. Boundary conditions including potential evaporation (*PE*), relative humidity

(*RH*), and air temperature (T_a) (Fig. 8.7b) were applied to the surface of the soil specimen at an elevation of 0.21 m. The *AE* was computed by Eq. 8.19. The numerical simulation was performed for 40 days with interval time step ranged from 0.1- 0.2 day.

Table 8.1 Soil parameters in Yanful and Choo's experiment (1997), and Tratch's experiment (1995).

Descriptions	Yanful and Choo (1997)		Tratch (1995)
Soil type	Find sand	Clay	Silt
Saturated volumetric water content, θs	0.31	0.46	0.41
Saturated coefficient of permeability, k_s (m/day)	0.864	5.79E-6	1.78E-3
a_f (kPa)	661.32	2.18	48.72
n_f	0.77	3.48	6.01
m_f	0.54	1.12	0.51
h_r (kPa)	139047.2	6.08	132.71
p	--	--	8
k_{min} (m/day)	--	--	1E-9
δ_{corr}	1.8	--	--

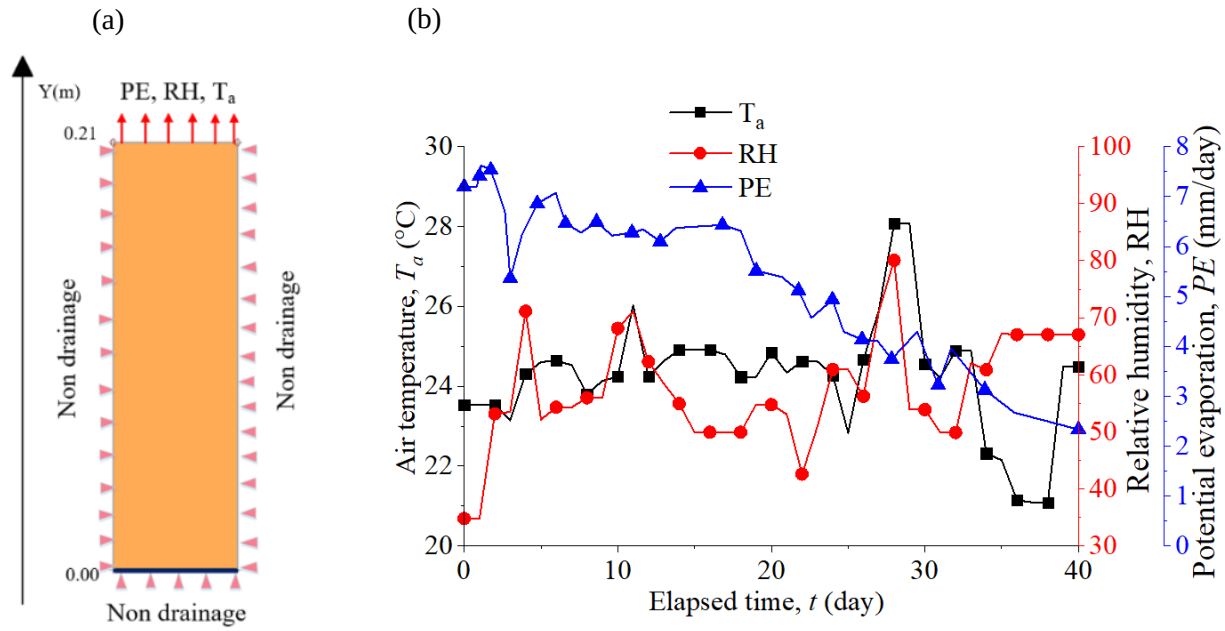

Figure 8.7 (a) Geometry, and (b) boundary conditions of soil columns simulation.

8.4.3 Numerical results and discussions

Fig. 8.8 presents the comparisons in actual evaporation rate obtained using the numerical simulation and the experimental results. Close agreement is observed between all the results. Therefore, Eq. 8.19 is effective to

compute the actual evaporation.

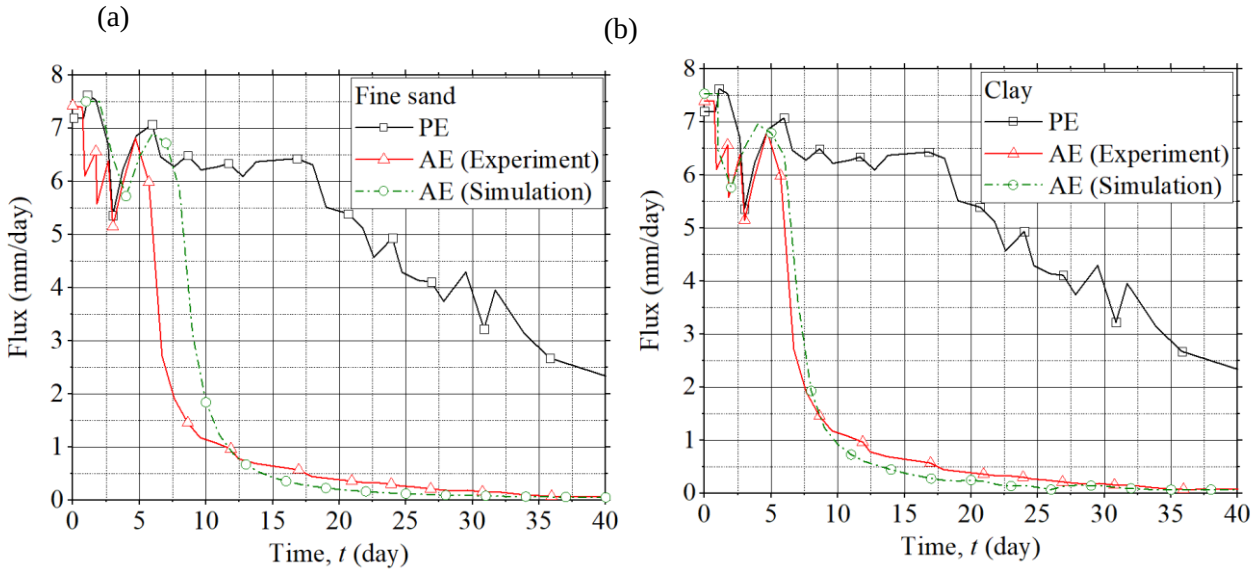

Figure 8.8 Comparisons of experimental and numerical results of (a) find sand and (b) clay.

8.5 Validation of evapotranspiration model

8.5.1 Introduction of Tratch's experiment (1995)

Tratch (1995) conducted laboratory experiment for 86 days to study an influence of plant on evapotranspiration. In this experiment, the soil column was constructed with a 0.6 m length of 0.125 m internal diameter PVC pipe. Soil material used in this experiment was silt. SWCC of silt was fitted by Fredlund and Xing (1994) model based on experimental data reported by Bruch (1993) (Fig. 8.9a). In addition, unsaturated coefficient of permeability of this soil was estimated based on fitted SWCC and saturated coefficient of permeability based on modified Cambell (1974) model as shown in Eq. 8.33 (Fig. 8.9b). The parameters of silt were summarized in Table 8.1.

$$k(s) = (k_s - k_{\min})\left[\left[1 - \frac{\ln(1+s/h_r)}{\ln(1+10^6/h_r)}\right]\left[\frac{1}{\ln(\exp(1)+(s/a_f)^{n_f})^{m_f}}\right]\right]^p \tag{8.33}$$

where $k(s)$ is coefficient of permeability of soil at matric suction s (kPa); k_s is saturated coefficient of permeability of soil; k min is minimum coefficient of permeability of soil; a_f, n_f, m_f, and h_r (kPa) are parameters obtained from Fredlund and Xing (1994) model; p is parameter used to control the modified Cambell (1974) estimation of hydraulic conductivity.

The upper end of column was left open to atmosphere. Water was supplied to the base of the soil column as illustrated in Fig. 8.10d. The plant seeds were sown on the surface of soil. As plants growth, the soil column experienced an evapotranspiration process. Potential evapotranspiration rate was daily determined by evaporating pan.

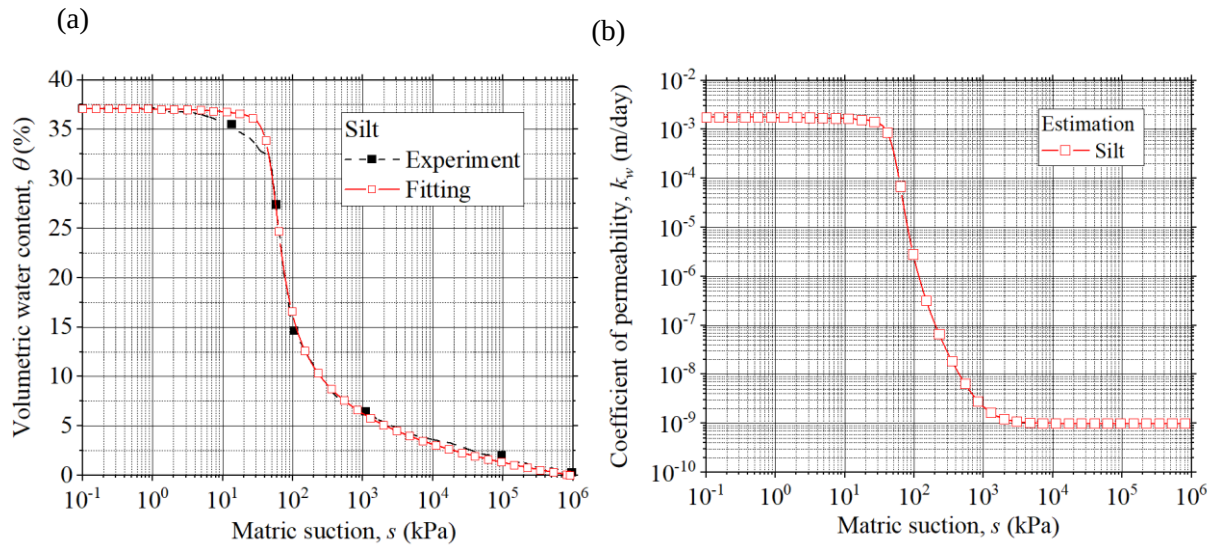

Figure 8.9 (a) SWCC, and (b) coefficient of permeability of silt.

8.5.2 Model geometry and analytical conditions

Two different numerical simulations were carried out. On the one hand, the first numerical simulation was considered a transpiration effect. A vertical 1D model was set up with a 0.6 m depth. The model was run for 86 days with time-step range of 0.1 day to 0.2 day. The bottom of the model consisted of a flow boundary condition using the data from Tratch's thesis (Figs. 8.10 b,c,d). Since the column was fully saturated at the beginning of the test, an initial pore water pressure of 0 kPa was assigned for soil.

Boundary conditions including air temperature, relative humidity, potential evapotranspiration were applied to the top of the model. Lower end of model was applied normal flux against time as presented in Fig. 8.10c. The actual evaporation was computed based on Eq.8.19. Furthermore, the plant parameters including root depth (R_t), the leaf-area index (LAI), the plant limiting function (PLF) as indicated in Fig. 8.11 were set to calculate the transpiration by employing Eqs. 8.22 - 8.24. A triangular root zone distribution was employed in this simulation.

Experimental results obtained from Garg et al. 2015 revealed that the PLF from non-crop species was similar to that proposed by Van Genuchten et al (1987) (Fig. 8.11b). Therefore, PLF proposed by Van Genuchten et al. 1987 was employed in this study. PLF is used to control the capability of root-water uptake of grass against matric suction. Grass might not transpire if the matric suction is too small due to the lack of aeration or when the matric suction is extremely high hence the grass might not further extract soil moisture. It was assumed that the grass transpires when soil suction is higher than 'anaerobiosis point' (s_1) and lower than 'wiling point' (s_3). In addition, the water uptake by the roots is maximal when the matric suction in the soil is between s_1 and s_2.

On the other hand, second numerical simulation was conducted to compute the amount of actual evaporation in case of ignoring the transpiration effect. The only difference with the above-mentioned

simulation was that the actual evaporation in this simulation was computed based on Eq. 8.19 and the transpiration was neglected.

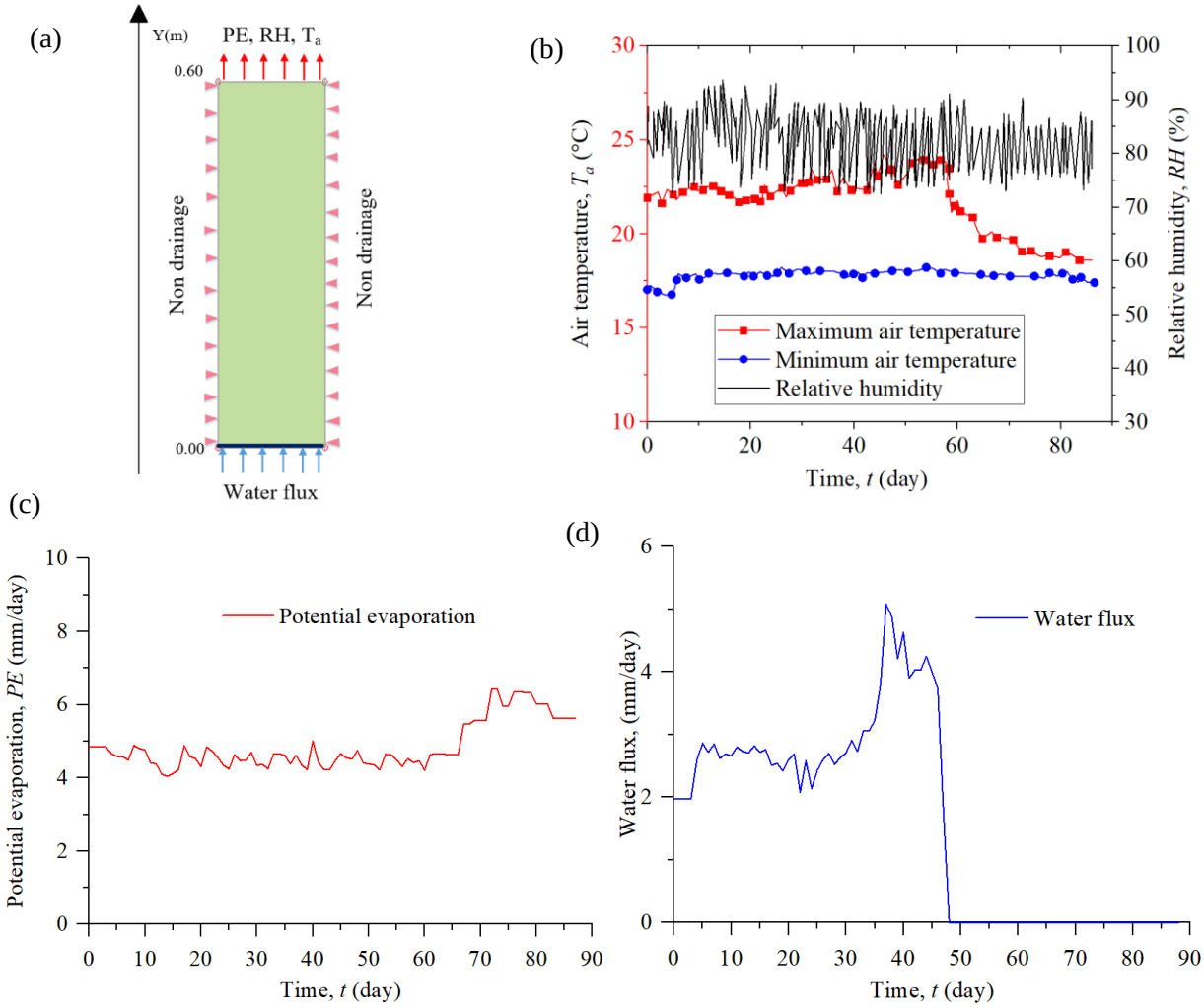

Figure 8.10 (a) Geometry, and (b), (c), (d) boundary conditions of soil columns simulation.

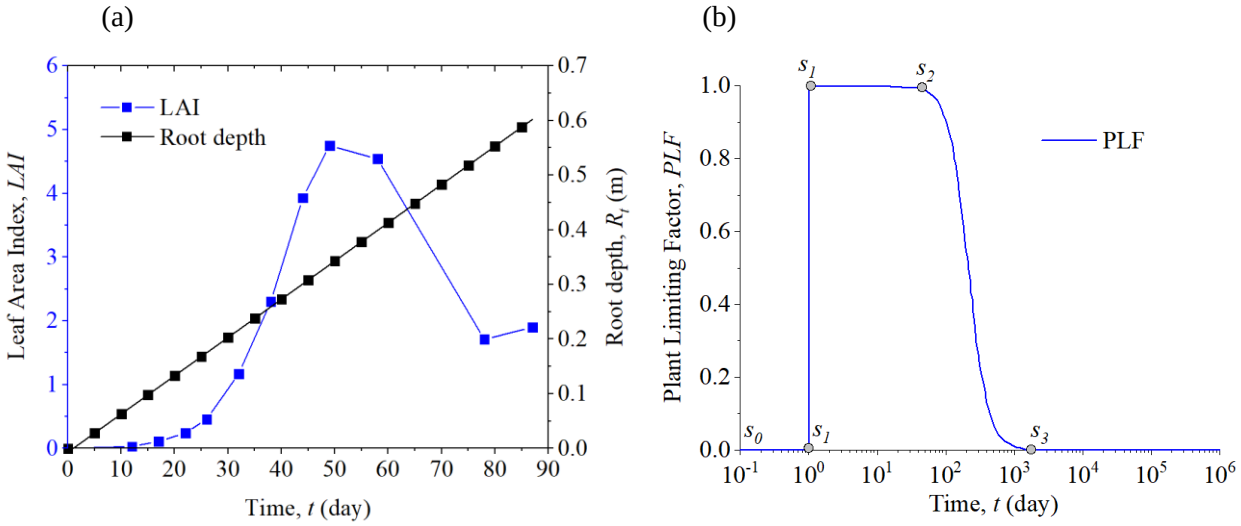

Figure 8.11 Plant parameters used in simulation.

8.5.3 Numerical results and discussions

It can be seen from Fig. 8.12 that the evapotranspiration flux from the first numerical simulation agreed well with that from the measured data presented by Tratch (1995) over 86 days. In contrast, there was significantly less agreement as the transpiration was neglected in the second simulation. From the start of the experiment to day 15, the second numerical simulation produced reasonable as compared to the experiment since the evaporation dominated the transpiration. However, after the day of 15, the transpiration flux increased significantly since there was a dramatic rise in LAI and R_t. From the day 40 to the end of the experiment, there was a huge difference between the two numerical results. In case of taking transpiration into account, the evaporation flux remained constant at 0 mm/day and the transpiration flux decreased by 30% from day 40 (4.3 mm/day) to the end of the experiment (1.4 mm/day) due to water deficiency. In contrast, there was a dramatic decrease in evaporation flux when transpiration was ignored in the second numerical simulation. In addition, the evaporation flux in the second numerical simulation was nearly a third as compared to the evapotranspiration flux derived from the first numerical simulation. Therefore, taking the transpiration into account in numerical simulation is important to study the hydraulic behavior of vegetated soil. The numerical simulation reveals that there might be a lower moisture flux from the soil in case the transpiration is neglected. As a result, soil water content might be higher than that in reality.

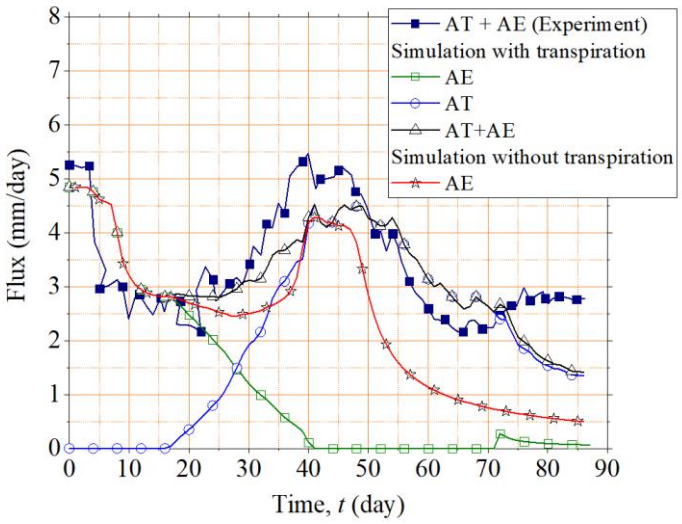

Figure 8.12 Comparisons of experimental and numerical results of evapotranspiration test.

8.6 Numerical simulation of Komaoka soil slopes

8.6.1 Model geometry and boundary conditions

The geometry and boundary conditions of two slopes for numerical simulation are demonstrated in Fig. 8.13. Two-dimensional model of the slope has a total height of 8 m and a length of 18 m. The coupled nonisothermal-seepage analyses were performed for both bare slope and grassed slope. Three stages of

analyses were conducted for each soil slope. Firstly, the steady-state analysis was performed by assuming the total head of 2 m at the bottom of the model, while the ground temperature at the slope surface and bottom of the model was assumed to be 10 °C and 5 °C. These values of temperature were equal to the average air temperature and estimated soil temperature at the bottom of the slope on 11 May 2012. After that, a transient analysis was performed to set the soil water content/matric suction and soil temperature distributions into soil slopes in the second stage. The climate boundary obtained from Automatic Meteorological Data Acquisition System (AMeDAS) provided by the Japanese Meteorological Agency (JMA) including rainfall, snowfall, air temperature, relative humidity, solar radiation, and wind speed over a period of 5 years from 11 May 2012 to 10 May 2017 was applied on the slope surface. Impermeable and adiabatic boundaries were set for two lateral sides, while a bottom of the model was assigned as 'unit gradient'. In this case, the downward flux was equal to the coefficient of permeability at the points in the bottom edge. In other words, the boundary downward flux was equal to the coefficient of permeability at the points in bottom edge multiplied by the edge boundary length. Finally, the climate boundary measured from the meteorological station in cut-slopes during 11 May 2017 to 11 September 2017 as presented in Fig. 8.14 was applied in the third stage. The bottom of the model was applied temperature (T_z) implemented from Andersland and Ladanyi (2004) equation as follows.

$$T_z = T_m + A.\exp\left(-z\sqrt{\frac{\pi}{\alpha_u p}}\right).\sin\left(\frac{2\pi t}{p} - z\sqrt{\frac{\pi}{\alpha_u p}}\right) \tag{8.34}$$

where T_m (6.4°C) is mean annual temperature; A (16.1°C) is surface temperature amplitude; z (8 m) is the depth; p (365 days) is corresponding period; t (day) is time; α_u (4.89 E-7 W/m^2 °C) is thermal diffusivity.

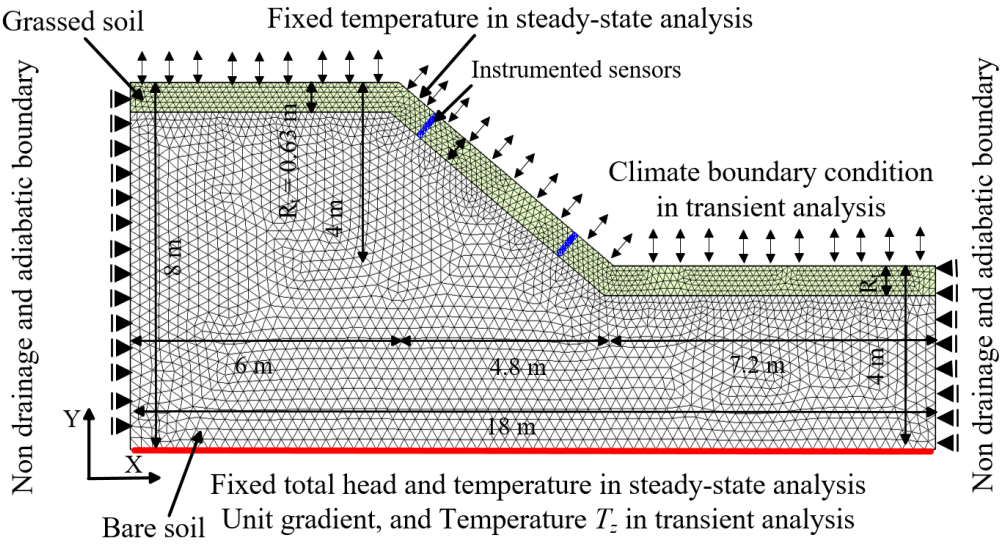

Figure 8.13 Boundary conditions and mesh generation of Komaoka soil slope

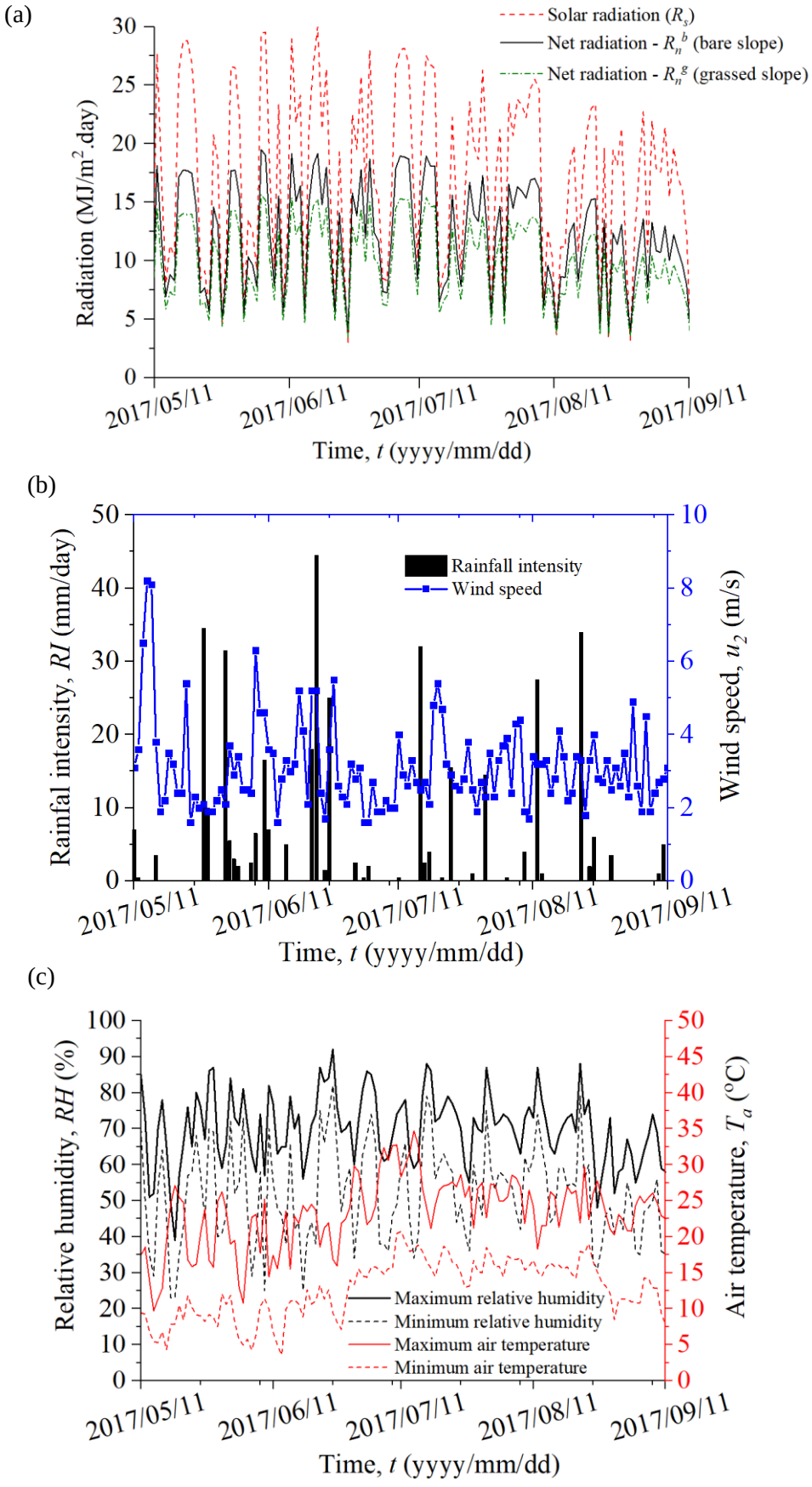

Figure 8.14 Meteorological data from 11 May 2017 to 11 September 2017 including (a) solar radiation and net radiation, (b) rainfall intensity and wind speed, (c) relative humidity and air temperature.

8.6.2 Soil and grass parameters

8.6.2.1 Soil hydraulic properties

Nguyen et al. 2020 conducted experimental study to investigate the effects of root volume ratio on hydraulic properties of Komaoka soil. The saturated coefficients of permeability of grassed soil at different grass ages were measured by permeability test apparatus. Whereas SWCCs and unsaturated coefficients of permeability were determined by column test apparatus. The soil types, soil properties, and grass species were identical to this study. Therefore, the saturated coefficient of permeability of bare soil measured from permeability test was employed in this simulation. In order to determine the hydraulic properties of grassed soil, R_v was measured from sampling at grassed slope at three days. It can be seen from Fig. 8.15a that R_v slightly increased from 2.98E-3 (May 11st, 2017) to 4.23E-3 (December 11st, 2017). The saturated coefficients of permeability of grassed soils were interpolated based on relationship of R_v and k_s (Nguyen et al. 2020) as presented in Fig. 8.15b. In Fig. 8.15, GF and BF were referred to grassed slope and bare slope, respectively. It is followed by the measured date. It can be seen that the saturated coefficients of permeability of the grassed soil were lower than bare soil. In addition, saturated coefficient of grassed soil was slightly decreased against time. It is corresponding to the rise in R_v of grassed soil. Since the R_v was increased, more soil pores were occupied by grass roots and hence the flow channels were more clogged.

To verify the applicability of measured results obtained from the laboratory test, the saturated coefficients of permeability of bare soil were determined by conducting constant head infiltration appratus in field (JGS 2017) as shown in Fig. 8.16. The measurements were carried out at the top of soil slopes in two different days (July 11st 2019 and December 24th 2019). The constant head infiltration appratus has 0.696 m height and 0.2 m internal diameter. After preparing the ground for execuation, the infiltration cylinder was inserted to a depth of 0.04 m below the soil surface. Infiltration was initialed with a constant head applied to the soil surface. Once the infiltration started, infiltration flow rate was recored along with time. The saturated coefficient of permeability (k_{fs} (m/day)) are computed as follows:

$$k_{fs} = \frac{\alpha G Q_s}{r_0 \alpha h + r_0 + G \alpha \pi r_0^2} \tag{8.35}$$

where Q_s is steady state infiltration flow rate (m^3/s); h (= 0.17m) is infiltration head (water depth in test hole); r_0 (m) is radius of test hole; α (= 12) is soil texture/structure parameter set according to the type of soil. G is shape factor that is determined by the following equation for a test hole of radius r_0 (m) and penetration depth d (m).

$$G = 0.316(d / r_0) + 0.184 \tag{8.36}$$

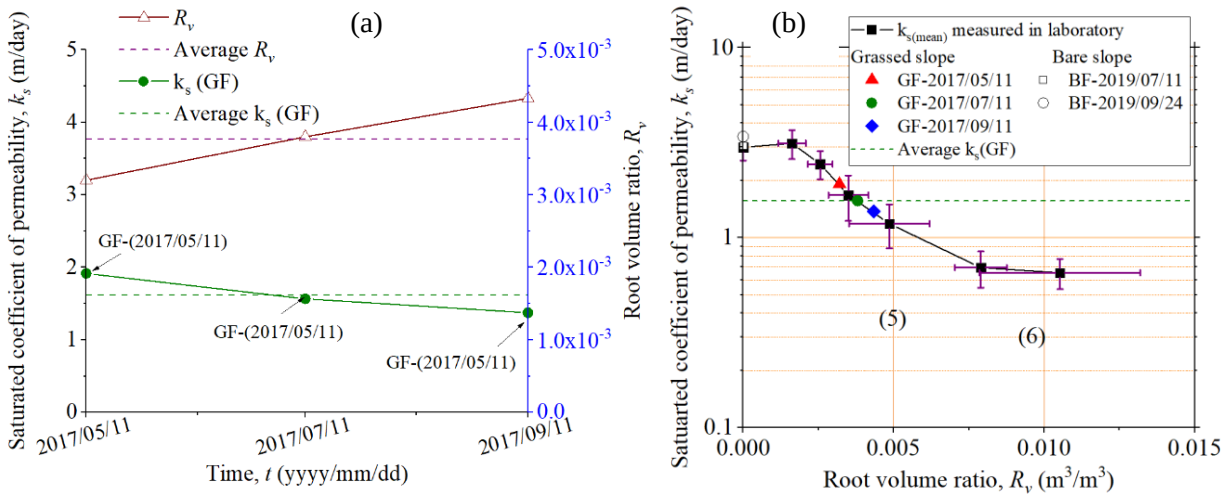

Figure 8.15 (a) Saturated coefficients of permeability of bare slope and grassed slope, (b) relationship between R_v and saturated coefficients of permeability of grassed soil (Nguyen at al. 2020).

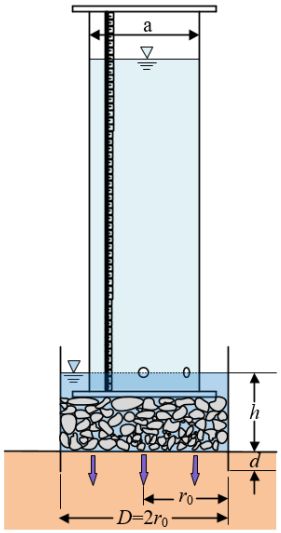

Figure 8.16 Schematic diagram of constant head infiltration apparatus.

The results of saturated coefficient of permeability of bare soil measured in filed were plotted in Fig. 8.15b. It can be seen that saturated coefficient of permeability measured in the filed agreed well with that in laboratory. The SWCC and unsaturated coefficient of permeability of grassed soil are estimated by models proposed by Nguyen et al. (2020), which is based on the Van Genuchten (1980) models. In Nguyen et al. (2020) models, the SWCC of grassed soil is estimated based on SWCC of bare soil and measured R_v. After that, the unsaturated coefficient of permeability is estimated based on SWCC and saturated coefficient of permeability of grassed soil. The models to compute SWCC and unsaturated coefficient of permeability of grassed soil are presented in Eqs. 8.38 and 8.39, respectively. The average values of saturated coefficient of permeability and R_v of grassed soil were employed for estimations. The estimated parameters are summarized in Table 8.2. The differences in the hydraulic properties of these soils are illustrated in Fig.

8.17. It can be seen clearly that the grassed soil retains higher water content at a given matric suction compared to bare soil. In contrast, the former also has a lower coefficient of permeability than the latter.

The void ratio of vegetated soil is conculcated as the following equation.

$$e' = \frac{e_0 - R_v(1+e_0)}{1+R_v(1+e_0)} \tag{8.37}$$

where e_0 and e' (dimensionless) are void ratio of bare soil and grassed soil, respectively; R_v (m^3/m^3) is the root volume ratio.

In order to consider the effects of active grass roots on hydraulic properties of soils, the SWCC and unsaturated coefficients of permeability of grassed soil is computed as following Eqs. 8.38 and 8.39, respectively.

$$S_r = \left[1+\left(\frac{se'^{m_4}}{m_3\exp(\kappa' R_v)}\right)^{m_2}\right]^{-m_1} \tag{8.38}$$

where S_r is the degree of saturation of soil; m_1 (dimensionless), m_2 (dimensionless), m_3 (kPa), m_4 (dimensionless) are the model parameters. m_1 and m_2 control the shape of the SWCC, while m_3 and m_4 are related to the air-entry value (AEV). Considering that the void ratio has neglectable effects on SWCC at high matric suction range, the product $m_1\, m_2\, m_4$ can be set to 1 (Gallipoli, 2012).

$$\frac{k(s)}{k_s} = \left[\frac{\left\{1-\left(a\exp(\kappa' R_v)s\right)^{nm}\left[1+\left(a\exp(\kappa' R_v)s\right)^{n}\right]^{-m}\right\}^2}{\left[1+\left(a\exp(\kappa' R_v)s\right)^{n}\right]^{m/2}}\right] \tag{8.39}$$

where $k(s)$ (m/day) is the unsaturated coefficient of permeability of soil; k_s (m/day) is saturated coefficient of permeability; n and m are material parameters (m = 1-1/n).

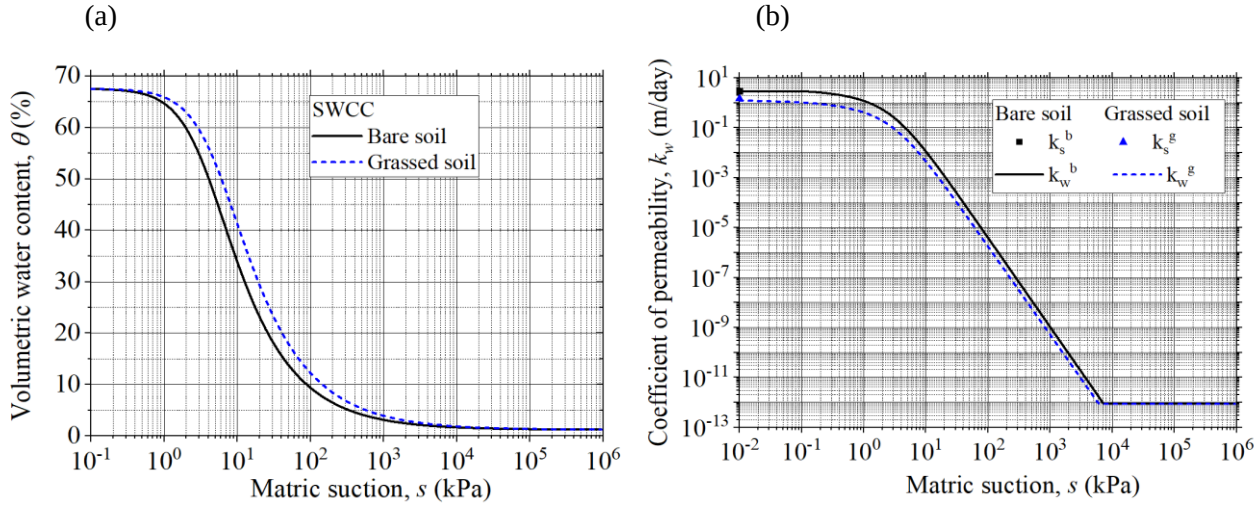

Figure 8.17 (a) SWCC, and (b) coefficient of permeability of bare soil and grassed soil.

8.6.2.2 Thermal properties

Improved Johansen – Lu et al (2007) model as shown in Eq. 8.40 is used for the estimation of thermal conductivity of soil.

$$\lambda = \left(\lambda_{sat} - \lambda_{dry}\right)\lambda_e + \lambda_{dry} \tag{8.40}$$

where λ, λ_{sat}, λ_{dry}. (J/day.m.°C) are the thermal conductivities of soil, saturated soil, and dry soil, respectively; λ_e is the Kersten number, which is related to degree of saturation.

$$\lambda_{sat} = \left(\lambda_s\right)^{1-n}\left(\lambda_w\right)^{n};\quad \lambda_{dry} = -0.56n + 0.51;\quad \lambda_e = \exp\left\{\alpha\left[1 - S_r^{(\alpha-\beta)}\right]\right\} \tag{8.41}$$

where λ_s, λ_w (J/day.m.°C) are thermal conductivity of soil particle and water, respectively; n is porosity of soil; α (0.728) is parameter related to soil texture; β (1.165) is shape parameter.

Volumetric heat capacity of soil is estimated by Jame (1977) and Newman (1996) model as presented in Eq.8.42.

$$C = \gamma_d\left(c_s + c_w w_u\right) \tag{8.42}$$

where C (J/m^3.°C) is volumetric heat capacity; C_s and C_w (J/m^3.°C) are mass specific heat of solid soils and unfrozen water, respectively.

The estimated results of thermal conductivity and volumetric heat capacity of Komaoka soil are presented in Fig. 8.18.

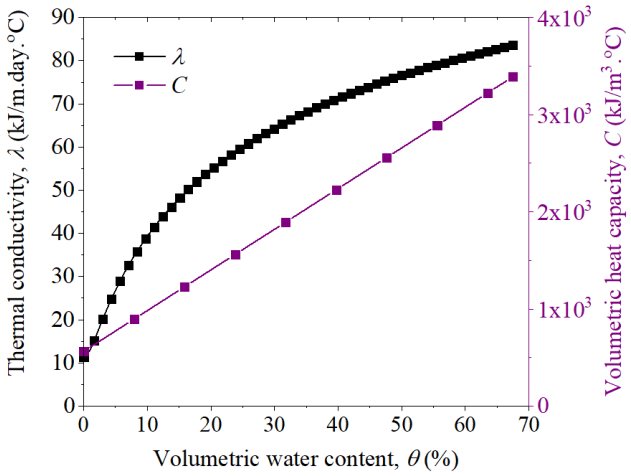

Figure 8.18 Thermal conductivity and volumetric heat capacity of Komaoka soil.

8.6.2.3 Grass parameters

LAI and R_t of grass were measured each month from 2017 May to December and were illustrated in Fig. 8.19. *LAI* increased from around 1.35 (May 2017) to 2.5 (July 2017) before remaining constant at this value

until middle of December. While the R_t is slightly increased from 0.57 m to 0.68 m over 4 months. It is noted that the whole result of measured *LAI* and the average value of R_t (0.63) were assigned in the simulation of grassed slope.

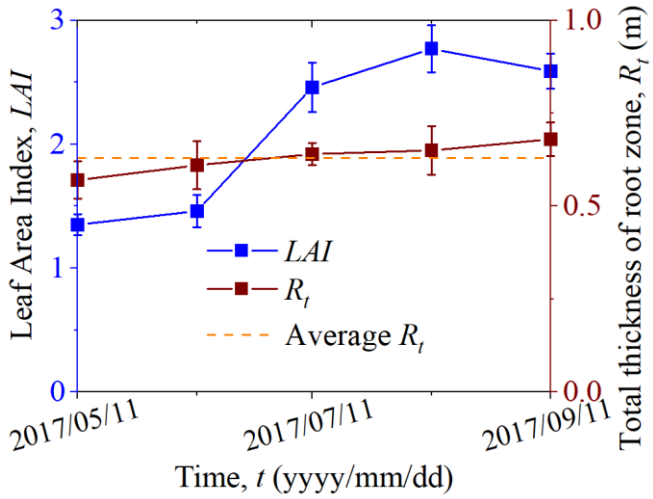

Figure 8.19 Variations of *RAI* and R_t against time.

8.6.2.4 Mechanical properties

Unsaturated shear strength of both bare soil and grassed soil were estimated using saturated shear strength properties by Vanapalli (1996) model as shown in Eqs. 8.26 and 8.28. Fig. 8.20 shows an example of saturated/unsaturated shear strength of bare soil and grassed soil at net normal stress of 7 kPa. It can be seen that the saturated shear strength of bare soil and grassed soil are 6.23 kPa and 9.17 kPa. The saturated sheat strength of two soils are increased with the rise in matric suction. The gap between two curves was greater at higher matric suction. After reaching around 30 kPa for bare soil and 70 kPa for grassed soil, these values decreased rapidly to the initial value which was equal to effective cohesion (*c'*) at saturated condition.

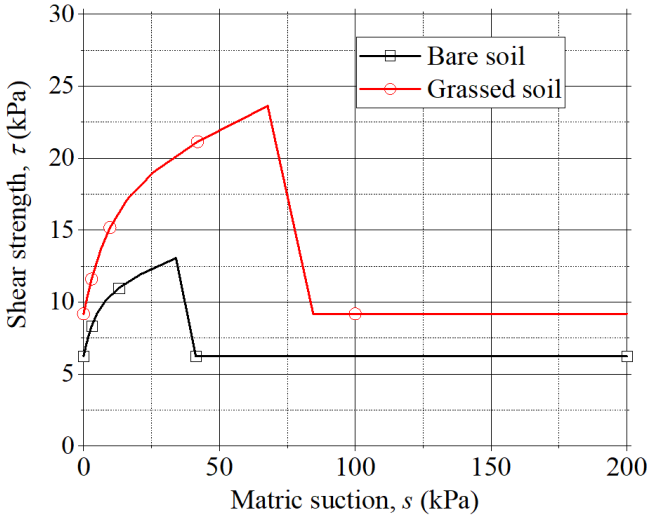

Figure 8.20 Estimations of unsaturated shear strength of bare soil and grassed soil.

Table 8.2 Soil parameters used in simulations.

Descriptions	Bare soil	Grassed soil
Saturated coefficient of permeability, k_s (m/day)		--
m_1	0.355	--
m_2	1.672	--
m_3	11.787	--
m_4	1.686	--
a	0.27	0.14
m	1.63	0.39
n	1.63	0.39
c' (kPa)	0.22	2.95
ϕ' (°)	40.7	41.4

8.6.3 Numerical results and discussions

8.6.3.1 Volumetric water content

The results of volumetric water content at 0.05 m and 0.35 m depths derived from the numerical simulation and field measurement are selected to be presented in Fig. 8.21. Volumetric water content of grassed soil is lower compared to that of bare soil. Furthermore, the volumetric water content in the latter is far fluctuated against rainfall infiltration as compared to the former. This is caused by the lower coefficient of permeability as shown in Fig. 8.17b. The numerical simulation captures well the variations in volumetric water content of soil against the climatic variations.

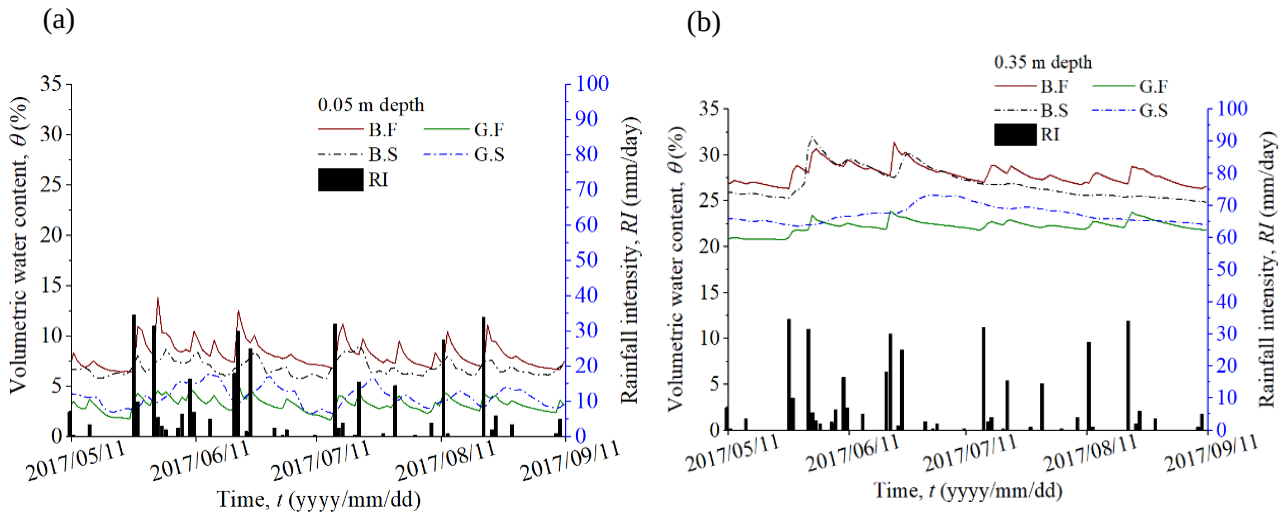

Figure 8.21 Comparisons in volumetric water content between experimental and numerical results.

8.6.3.2 Matric suction

The comparisons of matric suction at 0.25 m depths between the numerical simulation and field measurement are illustrated in Fig. 8.22. Matric suction of grassed soil doubled as compared to bare soil. It is corresponding to the results of volumetric water content as presented in Fig. 8.21. The close similarity is observed between numerical simulations and filed measurement.

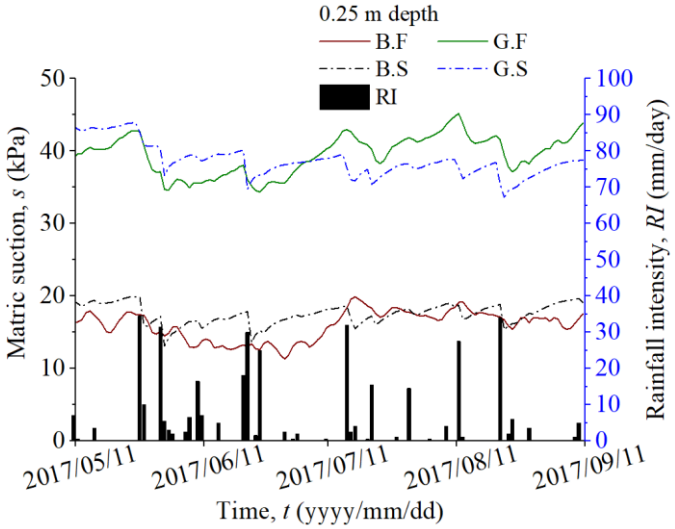

Figure 8.22 Comparisons in matric suction between experimental and numerical results.

8.6.3.3 Soil temperature

Fig. 8.23 presents the comparisons in soil temperature between field measurement and numerical simulation for both bare and grassed slopes. The soil temperature at 0.05 m depth more fluctuates because it is significantly affected by the variation of air temperature and net radiation. The numerical simulation can reasonably reproduce the changes in soil temperature of both two soil slopes by considering the effect of grass leaves on reducing the net radiation hence decrease the soil heat on soil surface. This simulation shows that the influence of grass leaves causes the lower soil temperature in grassed soil.

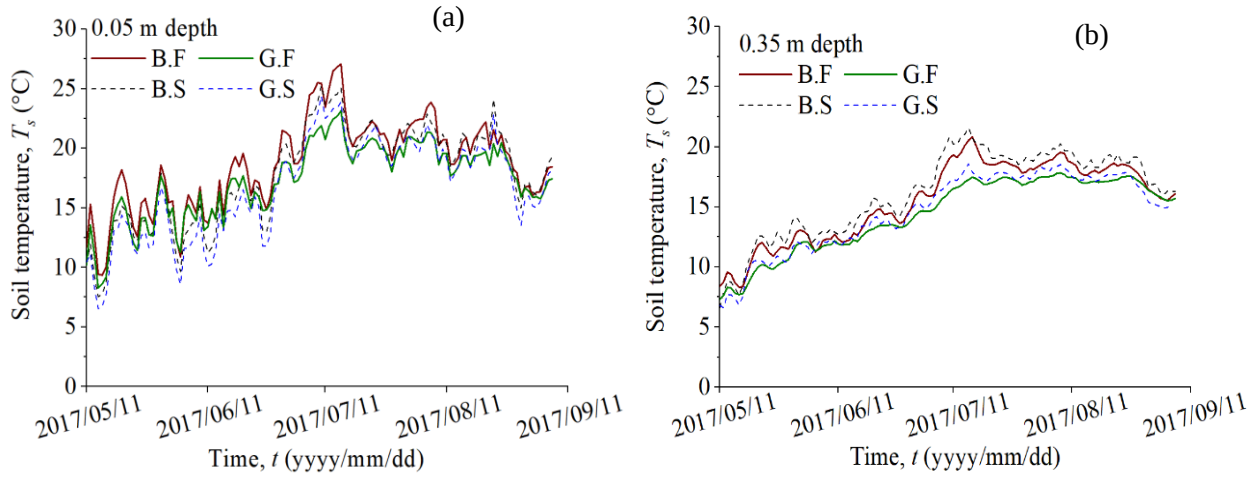

Figure 8.23 Comparison in soil temperature in bare slope and grassed slope.

8.6.3.4 Factor of safety

A comparison in FOS of bare slope and grassed slope derived from slope stability analysis are illustrated in Fig. 8.24. FOS of the former slightly fluctuates at somewhere in the vicinity of 2.15 over four-month period. Whereas the FOS of the latter is higher than the former by around 20 %. The higher value of FOS of grassed slope is attributed to the higher in matric suction as presented in Fig. 8.21. The higher shear strength of soil due to reinforcement of grass roots is also contributed. Furthermore, mechanical effect of roots is more significant for increasing the stability of grassed soil slope than hydrological effect (accounted for approximately 14 %). The similar findings are also reported by Feng et al (2020).

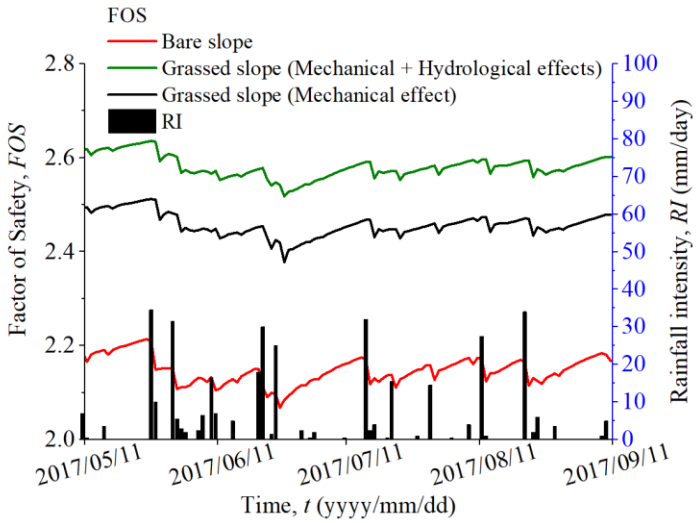

Figure 8.24 Comparisons in FOS of bare slope and grassed slope.

Fig. 8.25 presents the example of slip failure and FOS of grassed slope computed in 1858 day of numerical simulation. Since this numerical simulation started from May 11st, 2012, day 1858 is corresponding to June 11st, 2017. A maximum depth of slip surface in grassed slope is greater than bare slope (1.2 m and 1.0 m, respectively). These values are nearly two times as higher as the total thickness of grass root zone (R_t) (0.63 m). In addition, it is clearly seen that there were also the differences in length and volume of slip failure. As have mentioned above, the grassed soil has higher matric suction and shear strength. As a result, the shallow landslide-prone areas are resisted.

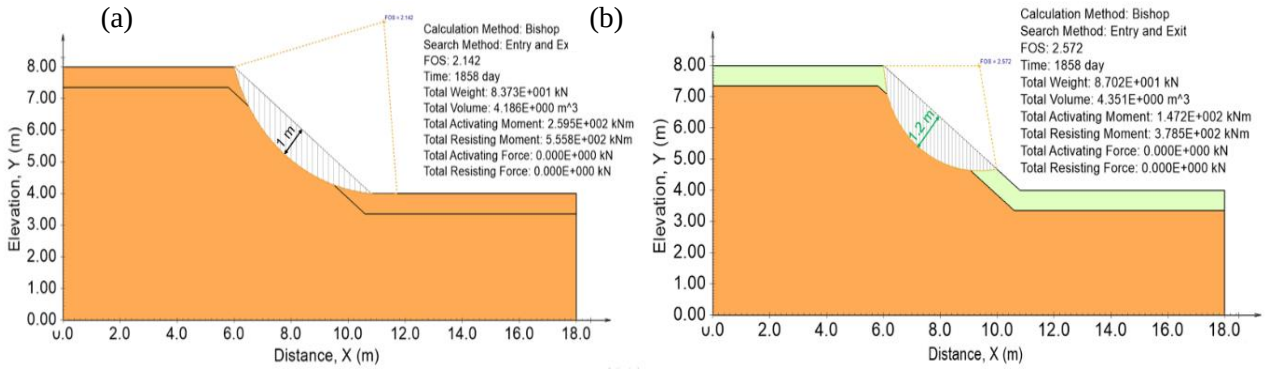

Figure 8.25 Example of slip surfaces of (a) bare slope, and (b) grassed slope.

8.7 Summary

This chapter firstly validated the models and numerical procedures to predict the actual evaporation and actual evapotranspiration. After that, an approach of coupled nonisothermal-seepage numerical analysis for unsaturated soil slope with consideration of hydro-thermal effects of grass was proposed. Next, the proposed numerical approach was validated by comparing simulation results and field measurement results. In addition, the slope stability analysis was performed by employing both volumetric water content and soil temperature distributions from coupled nonisothermal-seepage numerical analysis with consideration of the effects of grass on the mechanical properties of soils. The factor of safety of grassed slope and bare slope were compared to study the beneficial hydro-mechanical effects of grass on soil slope.

Yanful and Choo (1997) model was employed to validate the model to predict actual evaporation from the effect of climate conditions. Whereas, the applicability of models and numerical approach to compute actual evapotranspiration was implemented from Tratch (1995) model. It can be seen that the models and numerical approach were useful to predict actual evaporation and actual evaporation.

The good agreement between field measurements of Komaoka soil slope and numerical simulation results shown that the recommended approach considering the changes in SWCC, coefficient of permeability, grass parameters (i.e. LAI and total thickness of root zone), proper values of net radiation of grassed slope was effective to accurately predict the volumetric water content/matric suction and soil temperature for a long-term period against the climate variations. In fact, the numerical simulation captured well the variations in volumetric water content/matric suction of soil against the climatic variations. Besides, the numerical simulation reasonably reproduced the changes in soil temperature of both grassed slope by considering the effect of grass leaves on reducing the net radiation hence decrease the soil heat on the soil surface. This simulation has shown that the influence of grass leaves causes the lower soil temperature in grassed soil.

It was clearly seen that FOS of the grassed slope was higher than the bare slope by around 20 %. Furthermore, there were differences in maximum depth and volume of slip failure between bare slope and grassed slope. A maximum depth of slip surface in grassed slope is greater than bare slope (1.2 m and 1.0 m, respectively). While the volumes of slip failure were 2.572 and 2.142 for the latter and the former in June 11st 2017, respectively. Mechanical effect of roots is more significant for increasing the stability of grassed soil slope than hydrological effect. Since the grassed soil has ability to retain higher matric suction and higher shear strength, the shallow landslide-prone areas were resisted.

9 CONCLUSIONS AND RECOMMENDATIONS

9.1 Conclusions and recommendations

The findings from Chapter 3 can be outlined as follows:

1. Grass has influences on minimizing and stabilizing volumetric water content of soil near the slope surface. There is a lower volumetric water content in grassed slope as compared to that in bare slope. Furthermore, the volumetric water content in the grassed slope is less fluctuated against infiltration than in bare slope, especially when the snow melt occurs.
2. There is a higher matric suction in grassed slope than bare slope. It is corresponding to the lower volumetric water contents in the former as compared to the latter. The reason is the differences in soil hydraulic properties (SWCC and saturated/unsaturated coefficient of permeability). Another attributable reason is the transpiration due to soil-grass-atmosphere interaction.
3. The gap of matric suction between grassed slope and bare slope is greater in winter with the existence of snow cover. It might be because more exudates are released by grass roots.
4. In warm season, lower daily soil temperature is observed in grassed slope. The reason is that the grass leaves intercept net radiation by shading the ground surface. In contrast, the higher daily soil temperature in the bare slope is observed in winter seasons due to the insulation of grass leaves.
5. Since the soil temperature in grassed slope is higher than 0° C in snowy season, the shear strength of grassed soil is not be affected by freeze-thaw action. However, as the soil temperature near the slope surface of bare slope is around 0° C, shear strength of bare soil might be reduced because of freeze-thaw effects. Therefore, the shallow stability of grassed slope might be higher than that of bare slope.

The findings from Chapters 4, 5, and 6 can be outlined as follows:

1. There are differences in SWCCs of bare soil and grassed soil. Grass roots result in the capability to retain higher matric suction in grassed soil as compared to bare soil. At the same volumetric water content, the higher grass age has a higher matric suction. A reason for this phenomenon is that the soil pores are occupied by grass roots. Another reason might be attributed to the exudates released by grass roots. The increase in grass age also causes the rise in AEV of grassed soil.
2. The saturated coefficient of permeability of grassed soil is lower than bare soil and it decreases with the increase in grass age. In addition, there is a significant decrease in the unsaturated coefficient of permeability of grassed soil with a higher grass age. Since more soil pores are clogged by grass roots, the flow channels are blocked due to the increase in the root volume ratio. An additional reason is that the exudates, which are released by grass roots, lead to the higher viscosity of the liquid phase.
3. The grass roots result in a decrease in outflow and an increase in runoff for Komaoka soil. Besides, the increase in grass age also causes lower amount of outflow and higher amount of runoff. The reasons

are due to the different hydraulic properties of grassed soils. The higher grass age has lower saturated/unsaturated coefficient of permeability.

4. The matric suction in grassed soil reduces later than that in bare soil under rainfall. However, there is a significantly sharper decrease in matric suction of grassed soil with a higher grass age. The matric suction of both bare soil and grassed soils remain constant at around 2 kPa under long and intense rainfall events regardless of grass age. The volumetric water content in grassed soils is higher than that in bare soil during intense rainfall due to its higher ability to retain water. Grassed soil with the higher grass age has higher volumetric water content under intense rainfall.
5. Both Fredlund model (1994) and Van Genuchten model (1980) are effective to fit the SWCCs of bare soil and grassed soil. However, the unsaturated coefficients of permeability of grassed soil are over-estimated by these two models regardless of grass age. Only Van Genuchten (1980) model shows a good agreement with the unsaturated coefficient of permeability of bare soil.
6. A new model based on the Van Genuchten (1980) is proposed for estimating the unsaturated coefficient of permeability of grassed soil. The unsaturated coefficients of permeability of grassed soils at different grass ages estimated by this model present a good agreement with experimental results obtained from column tests.

The findings from Chapter 7 can be outlined as follows:

1. The experimental results obtained from triaxial tests present that shear strength of root permeated soil is enhanced. There is an increase in effective cohesion (c'), effective angel of internal fraction (ϕ'), and peak shear strength (Q_{max}) as grass age increases.
2. The volume strain is reduced as the grass age increases. The reason is that the root volume ratio is higher corresponding to the rise in grass age. As the axial strain increases, the friction between roots and soil particles resists the volume expansion. Besides, not only the shear strength of soil but also the tensile strength of roots resists the shear stress due to applying load. Higher root volume ratio leads to a higher amount of total tensile strength of roots and greater friction between roots and soil particles.
3. The unsaturated shear strength of grassed soil estimated based on Vanapalli model (1996) shows that there might be an increase in unsaturated shear strength of grassed soil when grass age is higher. However, experiments employing triaxial tests should be further conducted to validate the estimated results.

The findings from Chapter 8 can be outlined as follows:

1. There is a good agreement between the numerical simulation results and field measurements of Komaoka soil slope. This proves that the recommended approach considering the changes in hydraulic properties (i.e. SWCC, saturated/unsaturated coefficient of permeability), grass parameters (i.e. LAI and a total thickness of root zone) which related to transpiration, and proper net radiation of grassed slope is useful to predict the variations in volumetric water content/matric suction and soil temperature

for a long-term period against the climate effects.

2. The results derived from slope stability analysis indicate that the grass roots resist the shallow landslide-prone area by minimizing the infiltration, enhancing matric suction due to modifications of soil hydraulic properties and transpiration process, and increasing shear strength of soil due to friction caused by soil-root interaction. In fact, FOS of the grassed slope is higher than the bare slope by about 20 %. Moreover, the maximum depth of slip surface and volume of slip failure in the former is greater than that in the latter.
3. Mechanical effect of roots is more significant for increasing the stability of grassed soil slope than hydrological effect.

9.2 Future assignments

1. Field measurement results show that the gap of matric suction between grassed slope and bare slope is greater in winter with the existence of snow cover. It might be because more exudates are released by grass roots. However, this explanation is not yet conclusive. The enhanced matric suction due to exudates released by the grass roots in the winter season should be further experimentally investigated.
2. It should be noted that the reduced SWCC and increased saturated/unsaturated coefficient of permeability could be recorded if the vegetated age is extended. Ng. et al (2019) reported that saturated coefficient of permeability of soil vegetated with shrubs was reduced during the first 2-3 months of transplantation. In contrast, it was increased after growing for 9 months due to evidently root decays. Ni et al (2019a) indicated that when the plant was relatively young, there was an increase in soil water retention capability. Whereas the change of SWCC was mostly affected by an increase in soil void ratio due to root decays when the plant became older. Therefore, further research is needed to investigate longer grass age effects of grass roots on hydraulic properties, seepage behaviors, and mechanical properties of soil.
3. It should be noted that this research conducted the consolidated drained test by employing triaxial test apparatus to investigate the mechanical behaviours of rooted soil in saturated condition. The effect of grass roots on angle indicating the rate of increase in shear strength with respect to a change in matric suction (ϕ^b) in unsaturated shear strength should be furthered examined.
4. The undrained triaxial test should be performed in order to study pore water pressure generation during shearing and the possibility of static liquefaction occurrence of grassed soil.
5. Shear strength of volcanic soil decreased due to effects of freeze-thaw action (Ishikawa and Miura, 2011). Field measurement results presented that bare soil was frozen in snowy season. Therefore,

effects of freeze-thaw on a reduction of shear strength of volcanic soil should be experimentally studied to access properly shallow stability of bare slope.

6. It should be noted that actual root architecture could be very complicated (Ni et al. 2019c and Feng at al. 2020). However, this study assumed that grass root has idealized uniform root architecture to simplify the numerical simulation. Further study should consider the effects actual root architecture to accurately predict the influence of grass on distributions of matric suction and shear strength along rooted zone.
7. Grass parameters (i.e. R_v, LAI, R_t) vary against seasons. Root volume ratio (R_v), leaf area index (LAI) of grass in the cold season might be different compared to that in warm seasons. Besides, the lower soil temperature in cold season might reduce transpiration (Ni et al. 2019a). Since this study performed the numerical simulation for grassed slope in warm season, further study is needed to investigate effects of temperature on transpiration of grass in cold region.

LIST OF REFERENCES

Ali, F.H., Osman, N., 2007. Soil–roots composite: correlation between shear strength and some plant properties. Electron. J. Geotech. Eng. V12 D.

Allen, R. G., Pereira, L. S., Raes, D., Smith, M. 1998. Crop evapotranspiration-Guidelines for computing crop water requirements-FAO Irrigation and drainage paper 56. Fao, Rome, 300(9), D05109

Aluwihare, S., Watanabe, K., 2003. Measurement of evaporation on bare soil and estimating surface resistance. Journal of Environmental Engineering, 129(12), 1157-1168.

An, N., Hemmati, S., Cui, Y. J., Maisonnave, C., Charles, I., Tang, C. S. 2018a. Numerical analysis of hydro-thermal behaviour of Rouen embankment under climate effect. Computers and Geotechnics, 99, 137-148.

An, N., Hemmati, S., Cui, Y. J., Tang, C. S., 2018b. Numerical investigation of water evaporation from Fontainebleau sand in an environmental chamber. Engineering Geology, 234, 55-64.

Andersland, O.B., and Ladanyi, B., 2004. Frozen ground engineering. John Wiley & Sons.

Bengough, A.G., 2012. Water dynamics of the root zone: rhizosphere biophysics and its control on soil hydrology. Vadose Zone Journal, 11(2).

Blight, G.E., 2002. Measuring evaporation from soil surfaces for environmental and geotechnical purposes. Water SA, 28(4), 381-394.

Bordoloi, S., Ng, C.W.W. 2020. The effects of vegetation traits and their stability functions in bio-engineered slopes: A perspective review. Engineering Geology, 105742.

Branson, F.A., Gifford, G.F., Owen, J. R., 1972. Rangeland hydrology. Range Science Series No. 1, Soc. Range Manage., Denver. Colo.

Bruch, P.G., 1993. Laboratory study of evaporative fluxes in homogeneous and layered soils (Doctoral dissertation, University of Saskatchewan).

Campbell, G.S. 1974. A simple method for determining unsaturated conductivity from moisture retention data. Soil science, 117(6), 311-314.

Campbell, K.A., Hawkins, C.D., 2003. Paper birch and lodgepole pine root reinforcement in coarse-, medium-, and fine-textured soils. Canadian journal of forest research, 33(8), 1580-1586.

Carminati, A., Zarebanadkouki, M., Kroener, E., Ahmed, M.A., Holz, M., 2016. Biophysical rhizosphere processes affecting root water uptake. Annals of botany, 118(4), 561-571.

Cui, Y.J., Gao, Y.B., Ferber, V., 2010. Simulating the water content and temperature changes in an experimental embankment using meteorological data. Engineering Geology, 114(3-4), 456-471.

Cui, Y.J., Lu, Y.F., Delage, P., Riffard, M., 2005. Field simulation of in situ water content and temperature changes due to ground-atmospheric interactions. Géotechnique, 55(7), 557-568.

Day, R.W., 1993. Surficial slope failure: a case study. J. Perform. Constr. Facil. 7 (4), 264–269.

De Baets, S., Poesen, J., Reubens, B., Wemans, K., De Baerdemaeker, J., Muys, B., 2008. Root tensile

strength and root distribution of typical Mediterranean plant species and their contribution to soil shear strength. Plant and soil, 305(1-2), 207-226.

Dunmola, A.S., 2012. Predicting evaporative fluxes in saline soil and surface-deposited thickened mine tailings (Doctoral dissertation, Carleton University).

Fan, C.C., Su, C.F., 2008. Role of roots in the shear strength of root-reinforced soils with high moisture content. Ecol. Eng. 33 (2), 157–166.

Feddes, R.A., Kowalik, P., Kolinska-Malinka, K., and Zaradny, H., 1976. Simulation of field water uptake by plants using a soil water dependent root extraction function. Journal of Hydrology, 31(1-2), 13-26.

Feng, S., Liu, H. W., Ng, C.W.W., 2020. Analytical analysis of the mechanical and hydrological effects of vegetation on shallow slope stability. Computers and Geotechnics, 118, 103335.

Fredlund, D.G., Rahardjo. H, Fredlund M.D., 2012. Unsaturated soil mechanics in engineering practice. John Wiley & Sons, 2012.

Fredlund, D.G., 1979. Appropriate concepts and technology for unsaturated soils, Second Canadian Geotechnical Colloquium, Canadian Geotechnical Journal. 16(1), 121-139.

Fredlund, D.G., Xing, A., 1994. Equations for the soil-water characteristic curve. Canadian geotechnical journal, 31(4), 521-532.

Fredlund, D.G., Xing, A., Huang, S., 1994. Predicting the permeability function for unsaturated soils using the soil-water characteristic curve. Canadian Geotechnical Journal, 31(4), 533-546.

Fredlund, M.D., Tran, D., Fredlund, D.G., 2016. Methodologies for the calculation of actual evaporation in geotechnical engineering. International journal of geomechanics, 16(6), D4016014.

Gallipoli, D., 2012. A hysteretic soil-water retention model accounting for cyclic variations of suction and void ratio. Géotechnique, 62(7), 605-616.

Gallipoli, D., Wheeler, S.J., Karstunen, M., 2003. Modelling the variation of degree of saturation in a deformable unsaturated soil. Géotechnique,53(1), 105-112.

Garg, A., Leung, A.K., Ng, C.W.W., 2015. Transpiration reduction and root distribution functions for a non-crop species Schefflera heptaphylla. Catena, 135, 78-82.

Geo-Slope International Ltd., 2008. Vadose zone modeling with Vadose/W 2007, 3rd Ed., Geo-SlopeInternational Ltd., Calgary, Alberta, Canada.

Ghestem, M., Sidle, R.C., Stokes, A., 2011. The influence of plant root systems on subsurface flow: implications for slope stability. Bioscience, 61(11), 869-879.

Gray, D.H., Al-Refeai, T., 1986. Behavior of fiber-versus fiber-reinforced sand. J. Geotech. Eng. ASCE 112 (8), 804–820.

Grayston, S.J., Vaughan, D., Jones, D., 1997. Rhizosphere carbon flow in trees, in comparison with annual plants: the importance of root exudation and its impact on microbial activity and nutrient availability. Applied soil ecology, 5(1), 29-56.

Hillel, D., Krentos, V.D., Stylianou, Y., 1972. Procedure and test of an internal drainage method for

measuring soil hydraulic characteristics in situ. Soil science,114(5), 395-400.

Hong, Y., Adler, R.F., 2008. Predicting global landslide spatiotemporal distribution: Integrating landslide susceptibility zoning techniques and real-time satellite rainfall estimates. International Journal of Sediment Research, 23(3), 249–257.

Ishikawa, T., Miura, S., Ito, K., Ozaki, Y., 2010. Influence of freeze-thaw action on mechanical behavior of unsaturated crushable volcanic soil. InProc. of the 5th International conference on Unsaturated Soils.

Ishikawa, T., Miura, S., 2011. Influence of freeze-thaw action on deformation-strength characteristics and particle crushability of volcanic coarse-grained soils. Soils and foundations, 51(5), 785-799.

Ishikawa, T., Tetsuya, T., Miura, S., 2015. Geohazard at volcanic soil slope in cold regions and its influencing factors. *Japanese Geotechnical Society Special Publication* 1.1: 1-20.

Jame, Y. W., 1977. Heat and mass transfer in freezing unsaturated soil (Doctoral dissertation, University of Saskatchewan).

Japan Meteorological Agency (JMA)., 2012. Past weather data, (in Japanese), Date accessed: June 20th, 2018.

Japanese Geotechnical Society. 2017. Japanese Geotechnical Society Standard (JGS 1319-2017). Method for determination of field-saturated hydraulic conductivity above the water table.

Japanese Geotechnical Society., 2009a. Japanese Geotechnical Society Standard (JGS 0051-2009). Method of classification of geomaterials for engineering purpose.

Japanese Geotechnical Society., 2009b. Japanese Geotechnical Society Standard (JGS 0101-2009). Practice for preparing disturbed soil samples for soil testing.

Japanese Geotechnical Society. 2009c. Japanese Geotechnical Society Standard (JGS 0311-2009). Test method for permeability of saturated soils.

Jibson, R. W., 2005. Landslide Hazards at La Conchita, California. Open-File Report 2005–1067, US Geological Survey, Reston, VA, p. 12.

Johansen, O., 1975. Thermal conductivity of soils, PhD Thesis, Trondheim, Norway (CRREL Draft Translation 637, 1977).

Jotisankasa, A., Sirirattanachat, T., 2017. Effects of grass roots on soil-water retention curve and permeability function. Canadian Geotechnical Journal, 54(11), 1612-1622.

Krahn, J., Fredlund, D.G., 1972. On total, matric and osmotic suction. Soil Science, 114(5), 339-348.

Kroener, E., Zarebanadkouki, M., Kaestner, A., Carminati, A., 2014. Nonequilibrium water dynamics in the rhizosphere: How mucilage affects water flow in soils. Water Resources Research, 50(8), 6479-6495.

Leung, A.K., 2014. Grass evapotranspiration-induced suction in slope: case study. Environmental Geotechnics, 3(3), 155-165.

Leung, A.K., Boldrin, D., Liang, T., Wu, Z., Kamchoom, V., Bengough, A.G., 2018. Plant age effects on soil infiltration rate during early plant establishment. Géotechnique, 68(7), 646-652.

Leung, A.K., Coo, J.L., Ng, C.W.W., Chen, R., 2016. New transient method for determining soil hydraulic conductivity function. Canadian Geotechnical Journal, 53(8), 1332-1345.

Leung, A.K., Garg, A., Ng, C.W.W., 2015a. Effects of plant roots on soil-water retention and induced suction in vegetated soil. Engineering Geology, 193, 183-197.

Leung, A.K., Garg, A., Coo, J.L., Ng, C.W.W., Hau, B.C.H., 2015b. Effects of the roots of Cynodondactylon and Schefflera heptaphylla on water infiltration rate and soil hydraulic conductivity. Hydrological processes, 29(15), 3342-3354.

Leung, A.K., Garg, A., Ng, C.W.W., 2015c. Effects of plant roots on soil-water retention and induced suction in vegetated soil. Engineering Geology, 193, 183-197.

Li, J.H., Li, L., Chen, R., Li, D.Q., 2016. Cracking and vertical preferential flow through landfill clay liners. Engineering Geology, 206, 33-41.

Liang, T., Knappett, J. A., Leung, A., Carnaghan, A., Bengough, A. G., Zhao, R., 2020. A critical evaluation of predictive models for rooted soil strength with application to predicting the seismic deformation of rooted slopes. Landslides, 17(1), 93-109.

Loades, K.W., Bengough, A.G., Bransby, M.F., Hallett, P.D., 2010. Planting density influence on fibrous root reinforcement of soils. Ecological Engineering, 36(3), 276-284.

Mahannopkul, K., Jotisankasa, A., 2019. Influences of root concentration and suction on Chrysopogonzizanioides reinforcement of soil. Soils and Foundations, 59(2), 500-516.

McCartney, J.S., 2007. Determination of the hydraulic characteristics of unsaturated soils using a centrifuge permeameter (Doctoral dissertation).

Meerdink, J.S., Benson, C.H., Khire, M.V., 1996. Unsaturated hydraulic conductivity of two compacted barrier soils. Journal of geotechnical engineering, 122(7), 565-576.

Monteith, J.L., 1965. Evaporation and environment. In Symposia of the society for experimental biology (Vol. 19, pp. 205-234). Cambridge University Press (CUP) Cambridge.

Morgenstern, N.U., Price, V.E., 1965. The analysis of the stability of general slip surfaces. Geotechnique, 15(1), 79-93.

Mori A, 2016. Development of unsaturated permeability test apparatus using approximated profile method. Hokkaido University.

Newman, G.P., 1995. Heat and mass transfer in unsaturated soils, M.Sc. Thesis, University of Saskatchewan, Saskatoon, SK.

Ng, C.W.W., Ni, J.J., Leung, A.K., 2019. Effects of plant growth and spacing on soil hydrological changes: a field study. Géotechnique, 1-15.

Ng, C.W.W., Zhan, L.T., 2007. Comparative study of rainfall infiltration into a bare and a grassed unsaturated expansive soil slope. Soils and foundations, 47(2), 207-217.

Ng, C.W.W., Leung, A.K., Woon, K.X., 2013a. Effects of soil density on grass-induced suction distributions in compacted soil subjected to rainfall. Canadian Geotechnical Journal, 51, 311-321.

Ng, C.W.W., Woon, K.X., Leung, A.K., and Chu, L.M., 2013b. Experimental investigation of induced suction distribution in a grass-covered soil. Ecological Engineering, 52, 219-223.

Ng, C.W.W, Pang, Y.W., 2000. Experimental investigations of the soil-water characteristics of a volcanic soil. Canadian Geotechnical Journal, 37(6), 1252-1264.

Ng, C.W.W., Leung, A.K., 2011. Measurements of drying and wetting permeability functions using a new stress-controllable soil column. Journal of Geotechnical and Geoenvironmental Engineering, 138(1), 58-68.

Ng, C.W.W., Leung, A.K., 2012. In-situ and laboratory investigations of stress-dependent permeability function and SDSWCC from an unsaturated soil slope. Geotechnical Engineering, 43(1), 26-39.

Ng, C.W.W., Leung, A.K., Woon, K.X., 2014. Effects of soil density on grass-induced suction distributions in compacted soil subjected to rainfall. Canadian Geotechnical Journal, 51(3), 311-321.

Ng, C.W.W., Ni, J.J., Leung, A.K., Wang, Z.J., 2016a. A new and simple water retention model for root-permeated soils. Géotechnique Letters, 6(1), 106-111.

Ng, C.W.W., Ni, J.J., Leung, A.K., Zhou, C., Wang, Z.J., 2016b. Effects of planting density on tree growth and induced soil suction. Géotechnique, 66(9), 711-724.

Ng, C.W.W., Zhan, L.T., 2007. Comparative study of rainfall infiltration into a bare and a grassed unsaturated expansive soil slope. Soils and foundations, 47(2), 207-217.

Nguyen, B. T., Ishikawa, T., Takumi, M. 2020. Effects evaluation of grass age on hydraulic properties of coarse-grained soil. Transportation Geotechnics, 100401.

Nguyen, T. B, Ishikawa, T, Subramanian, S.S., 2017. Rainfall infiltration and runoff characteristics of an unsaturated volcanic soil under grass cover. Second Pan American Conference on Unsaturated soils, November 12-15, 2017, Texas, USA, 135-145.

Nguyen, T. B., Ishikawa, T., Siva Subramanian, Yokohama. S, Tokoro, T., 2016. Applicability of three-dimensional coupled seepage and thermal analysis to soil slope stability in cold region. 56th Annual Meeting of Hokkaido Branch Japanese Geotechnical Society, Sapporo, Japan.

Nguyen, T.B, Ishikawa, T, Murakami, T., 2019. Numerical analysis of in-situ water content and temperature variations due to effects of grass cover. 7th Asia-Pacific Conference on Unsaturated Soils, August 23-25, 2019, Nagoya, Japan.

Ni, J.J, Cheng, Y., Wang, Q., Ng, C.W.W., Garg, A., 2019a. Effects of vegetation on soil temperature and water content: Field monitoring and numerical modelling. Journal of Hydrology, 571, 494-502.

Ni, J.J, Leung, A. K., Ng, C.W.W, 2019b. Unsaturated hydraulic properties of vegetated soil under single and mixed planting conditions. Géotechnique, 69(6), 554-559.

Ni, J.J., Leung, A.K., Ng, C.W.W., 2019c. Modelling effects of root growth and decay on soil water retention and permeability. Canadian Geotechnical Journal, 56(7), 1049-1055.

Ni, J.J., Leung, A.K., Ng, C.W.W., 2018a Modelling soil suction changes due to mixed species planting. Ecological Engineering, 117, 1-17.

Ni, J.J., Leung, A.K., Ng, C.W.W., Shao, W., 2018b. Modelling hydro-mechanical reinforcements of plants to slope stability. Computers and Geotechnics, 95, 99-109.

Ni, J.J., Leung, A.K., Ng, C.W.W., So, P.S., 2017. Investigation of plant growth and transpiration-induced matric suction under mixed grass-tree conditions. Canadian Geotechnical Journal, 54(4), 561-573.

Novoselov, V. S.,1960. A closed volumeter for plant root systems. FiziolRast, 7, 243-244.

Pagano, L., Reder, A., Rianna, G., 2019. Effects of vegetation on hydrological response of silty volcanic covers. Canadian Geotechnical Journal, 56(9), 1261-1277.

Rahardjo, H., Satyanaga, A., Leong, E. C., Santoso, V.A., Ng, Y.S., 2014. Performance of an instrumented slope covered with shrubs and deep-rooted grass. Soils and Foundations, 54(3), 417-425.

Ritchie, J.T., 1972. Model for predicting evaporation from a row crop with incomplete cover. Water resources research, 8(5), 1204-1213.

Rui, D., Ji, M., Nakamur, D., Suzuki, T., 2018. Experimental study on gravitational erosion process of vegetation slope under freeze–thaw. Cold Regions Science and Technology, 151, 168-178.

Sauceda, M., Johnson, D.W., Huang, J., Bin-Shafique, S., Sponsel, V.M., Appleford, M., 2014. Soil-strength enhancements from polymer-infused roots. Journal of Geotechnical and Geoenvironmental Engineering, 140(2), 04013004.

Scanlan, C. A., Hinz, C., 2010. Insights into the processes and effects of root-induced changes to soil hydraulic properties. 19th World Congress of Soil Science, Soil Solutions for a Changing World. 1-6.

Schlosser, F., Long, N.T., 1974. Recent results in French research on reinforced earth. J. Construct. Div. ASCE 100 (03), 223–237.

Shao, W., Ni, J.J, Leung, A. K., Su, Y., Ng, C.W.W., 2017. Analysis of plant root–induced preferential flow and pore-water pressure variation by a dual-permeability model. Canadian Geotechnical Journal, 54(11), 1537-1552.

Smucker, A.J.M., McBurney, S.L., Srivastava, A.K., 1982. Quantitative Separation of Roots from Compacted Soil Profiles by the Hydropneumatic Elutriation System 1. Agronomy Journal, 74(3), 500-503.

SoilVision Systems Ltd. 2010. SVSLOPE Theory Manual (SVOFFICE 2009). Saskatoon, Saskatchewan, Canada.

SoilVision Systems. 2009a. SVFlux, user's manual for, SoilVision Systems, Saskatoon, Saskatchewan, Canada.

SoilVision Systems., 2009b. SVHeat, user's manual, SoilVision Systems, Saskatoon, Saskatchewan, Canada.

SoilVision Systems., 2009c. SVSlope, user's manual, SoilVision Systems, Saskatoon, Saskatchewan, Canada.

Song, L., Li, J.H., Zhou, T., Fredlund, D.G., 2017. Experimental study on unsaturated hydraulic properties of vegetated soil. Ecological Engineering, 103, 207-216.

Sonnenberg, R., Bransby, M. F., Bengough, A. G., Hallett, P. D., Davies, M. C. R., 2012. Centrifuge modelling of soil slopes containing model plant roots. Canadian Geotechnical Journal, 49(1), 1-17.

Terzaghi, K. V., 1936. The shearing resistance of saturated soils and the angle between the planes of shear. In First international conference on soil Mechanics, 1936 (Vol. 1, pp. 54-59).

Tran, D. T. Q., Chan, D. H., Fredlund, D. G., 2014. Reassessment of Soil Suction at the Evaporation Rate Reduction Point for Saturated-Unsaturated Soil Surfaces. In Geo-Congress 2014: Geo-characterization and Modeling for Sustainability (pp. 4084-4096).

Tratch, D.J., Wilson, G.W., Fredlund, D.G., 1995. An introduction to analytical modeling of plant transpiration for geotechnical engineers. In 48th Annual Canadian Geotechnical Conference, Vancouver BC (pp. 771-780).

Van Genuchten, M. T., 1987. A Numerical Model for Water and Solute Movernent.

Van Genuchten, M.T., 1980. A closed-form equation for predicting the hydraulic conductivity of unsaturated soils 1. Soil science society of America journal, 44(5), 892-898.

Vanapalli, S.K., Fredlund, D. G., Pufahl, D.E., Clifton, A.W., 1996. Model for the prediction of shear strength with respect to soil suction. Canadian geotechnical journal, 33(3), 379-392.

Watson, K.K., 1966. An instantaneous profile method for determining the hydraulic conductivity of unsaturated porous materials. Water Resources Research, 2(4), 709-715.

Wilson, G. W., Fredlund, D. G., Barbour, S. L., 1997. The effect of soil suction on evaporative fluxes from soil surfaces. Canadian Geotechnical Journal, 34(1), 145-155.

Wilson, G. W., 1990. Soil evaporative fluxes for geotechnical engineering problems (Doctoral dissertation, University of Saskatchewan).

Wood, D.M., Diambra, A., Ibraim, E., 2016. Fibres and soils: a route towards modelling of root-soil systems. Soils and Foundations, 56(5), 765-778.

Wu, T.H., Watson, A., 1998. In situ shear tests of soil blocks with roots. Can. Geotech. J. 35 (4), 579–590.

Yanful, E. K., Choo, L. P., 1997. Measurement of evaporative fluxes from candidate cover soils. Canadian Geotechnical Journal, 34(3), 447-459.

Yildiz, A., F. Graf, S.M. Springman., 2020. On the dilatancy of root-permeated soils under partially saturated conditions. Géotechnique Letters, 1-4.

Yildiz, A., Graf, F., Rickli, C., Springman, S.M., 2018. Determination of the shearing behaviour of root-permeated soils with a large-scale direct shear apparatus. Catena, 166, 98-113.

Zhang, C.B., Chen, L.H., Liu, Y.P., Ji, X.D., Liu, X.P., 2010. Triaxial compression test of soil–root composites to evaluate influence of roots on soil shear strength. Ecological Engineering, 36(1), 19-26.

LIST OF NOTATIONS

Description	Symbol
Specific gravity	Gs
In-situ dry density	ρ_d
Maximum dry density	$\rho_{d\,max}$
Minimum dry density	$\rho_{d\,min}$
In-situ porosity	n
In-situ volumetric water content	θ_n
Mean grain size	D_{50}
Coefficient of uniformity	U_c
Fines content	F_c
Saturated coefficient of permeability of soil	k_s
Specimen length	L
Volume of water flowing through the soil specimen	Q
Cross-sectional area of the soil specimen	A
Measurement time	t
Sample value	X_i
Mean of all values	$\overline{X}$
Sample size	n
Water flow rate	$v_{zj,tave}$
Hydraulic head	H
Air-entry value	AEV
Root volume ratio	R_v
Degree of saturation of soil	S_r
Material parameter which is primarily a function of the air entry value of the soil	a
V-G material parameters	n
V-G material parameters	m (m = 1-1/n)
Matric suction	s
Volumetric water content at any matric suction	θ_w

Saturated volumetric water content	θ_s
Material parameter which is primarily a function of the air-entry value of the soil	a_f
Material parameter which is primarily a function of rate of water extraction from the soil once the air-entry value has been exceeded	n_f
Primarily a function of the residual water content	m_f
Matric suction at residual water content	h_r
Relative coefficient of permeability at matric suction *s*	$k_r(s)$
Air-entry value of the soil	s_{ave}
Dummy variable of integration representing matric suction	y
Void ratio of bare soil	e_0
Void ratio of vegetated soil	e'
Model parameters that control the shape of the SWCC	m_1, m_2
Model parameters that are related to the air-entry value (AEV)	m_3, m_4
Model parameter that controls the rate of reduction of the AEV due to root decay	κ
Macro void returned from root decay	e_r
Void ratio occupied by roots	e_{r0}
Model parameter that controls the rate of the increase in AEV	κ'
Effective confining pressure	$\sigma_{c'}$
Cell pressure	σ_c
Axial deviator stress	q
Volumetric strain	ε_v
Axial strain	ε_a
Shear stress on the failure plane at failure	τ_{ff}
Effective cohesion	c'
Effective normal stress on the failure plane at failure	$(\sigma_f - u_w)_f$
Total normal stress on the failure plane at failure	σ_{ff}
Pore-water pressure at failure	u_{wf}
Effective angel of internal fraction	ϕ'

Flux of rainfall	P
Infiltration rate	I
Runoff rate on soil surface	RO
Actual evaporation rate	AE
Net radiation flux	R_n
Soil heat flux	G
Latent heat flux	L
Sensible heat flux	H
Pore-water vapor conductivity by vapor diffusion within the air phase	k^{vd}
Actual transpiration sink term	S_{root}
Unit weight of water	γ_w
Slope of soil-water characteristic curves	m_2^w
Thermal conductivity of soil in x- directions	λ_x
Thermal conductivity of soil in y-directions	λ_y
Volumetric heat capacity of soil	C
Volumetric latent heat of soil	L_f
Rate of change in unfrozen water content with temperature	m_2^i
Temperature	T
Net shortwave radiation	R_{ns}
Net longwave radiation	R_{nl}
Canopy reflection coefficient	α
Stanfan-Boltzmann constant	σ
Maximum and minimum absolute temperature during 24 hour period	$T_{max,K}$; $T_{min,K}$
Clear-sky radiation	R_{so}
Station elevation above sea level	z
Solar constant	G_{sc}
Inverse relative distance Earth-Sun	d_r
Sunset hour angle	ω_s
Latitude	φ
Solar declination	δ

Number of the day in the year	J
Reference evapotranspiration	ET_0
Net radiation at the crop surface	R_n
Soil heat flux density	G
Mean daily temperature at 2 m height	T
Wind speed at 2 m height	u_2
Saturation vapor pressure	e_s
Actual vapor pressure	e_a
Slope vapor pressure curve	Δ
Saturation vapor pressure at the air temperature T	$e^o(T)$
Saturation vapor pressure at the air daily minimum temperature T_{min}	$e^o(T_{min})$
Saturation vapour pressure at the air daily maximum temperature T_{max}	$e^o(T_{max})$
Maximum relative humidity	RH_{max}
Minimum relative humidity	RH_{min}
Potential evaporation from bare soil	PE_b
Dimensional empirical parameter	ζ
Relative humidity of overlying air	RH
Molecular weight of water	ω_v
Gravity acceleration	g
Correction factor	δ_{corr}
Universal gas constant	R
Soil surface temperature	T_s
Residual soil suction	s_r
Potential transpiration rate	PT
Potential evapotranspiration rate	PE
Potential root uptake rate per unit time	PRU
Root distribution shape factor	RSF
Total thickness of root zone in length units	R_t
Depth to the given point in length units	R_n
Shear strength of soil	τ

Net total stress	σ_n
Pore air pressure	u_a
Pore water pressure	u_w
Parameter related to the degree of saturation	χ
Factor of safety equations with respect to moment equilibrium	F_m
Factor of safety equations with respect to force equilibrium	F_f
Total weight of a slice of width b and height h	W
Total normal force on the base of the slice	N
External point load	D
Radius of a circular slip surface	R
Horizontal distance from the centerline of each slice to the center of rotation or to the center of moments	x
Perpendicular distance from a point load to the center of rotation or to the center of moments	d
Perpendicular offset of the normal force from the center of rotation or from the center of moments	f (m)
Perpendicular distance from the resultant external water force to the center of rotation or to the center of moments	a
Resultant external water forces	A
Angle of the point load from the horizontal	ω
Angle between the tangent to the center of the base of each slice and the horizontal	α
Base length of each slice.	L
Parameter used to control the modified Cambell (1974) estimation of hydraulic conductivity	p
Mean annual temperature	T_m
Surface temperature amplitude	A
Corresponding period	p
Thermal diffusivity	α_u
Saturated coefficient of permeability (in field)	k_{fs}
Steady state infiltration flow rate	Q_s

Radius of test hole	r_0
Soil texture/structure parameter set according to the type of soil	α
Shape factor	G
Thermal conductivities of soil, saturated soil, and dry soil, respectively	λ, λ_{sat}, λ_{dry}
Kersten number	λ_e
Thermal conductivity of soil particle and water	λ_s, λ_w
Porosity of soil	n
Parameter related to soil texture	α
Shape parameter	β
Volumetric heat capacity	C
Mass specific heat of solid soils and unfrozen water, respectively.	C_s, C_w